ORNL/TM-2022/1846

Foam Fracturing Study for Stimulation Development of Enhanced Geothermal Systems

Hong Wang
Jy-An J. Wang
Yarom Polsky
Fei Ren
Viren Thakore

Date: Mar. 2022

OAK RIDGE NATIONAL LABORATORY
MANAGED BY UT-BATTELLE FOR THE US DEPARTMENT OF ENERGY

ORNL/TM-2022/1846

Materials Science and Technology Division

FOAM FRACTURING STUDY FOR STIMULATION DEVELOPMENT OF ENHANCED GEOTHERMAL SYSTEMS

Hong Wang, Jy-An J. Wang, Yarom Polsky,[1)] Fei Ren,[2)] Viren Thakore[2)]

[1]Electrification & Energy Infrastructure Division

[2]Temple University, 1947 North 12th Street, Philadelphia, PA 19122

Date Published: Apr. 2022

Prepared by
OAK RIDGE NATIONAL LABORATORY
Oak Ridge, TN 37831-6283
managed by
UT-BATTELLE, LLC
for the
US DEPARTMENT OF ENERGY
under contract DE-AC05-00OR22725

CONTENTS

Table of Contents

CONTENTS iii
LIST OF TABLES v
LIST OF FIGURES vi
ACRONYMS AND ABBREVIATIONS x
EXECUTIVE SUMMARY 1
1. BACKGROUND 4
2. INTRODUCTION 5
2.1 FOAM PREPARATION 5
2.1.1 General Requirements and Field Preparation 5
2.1.2 Preparation in Laboratory 5
2.2 FOAM APPLICATION 7
2.2.1 Foam Generation and Delivery 7
2.2.2 Foam Injection and Fracturing 7
2.3 FOAMS 9
2.3.1 Compositions 9
2.3.2 Effects of Temperature and Pressure 10
2.3.3 Stabilizing Agents and Emerging Strategy 10
2.4 TECHNICAL GAPS 10
2.5 OUTLINE OF REPORT 11
3. FOAM FRACTURING TESTING SYSTEM 12
4. FOAM FRACTURING TESTING TECHNIQUE 15
4.1 TEST PLAN 15
4.1.1 Monotonic Injection 15
4.1.2 Cyclic injection 15
4.2 PROCEDURES 16
4.3 MATERIALS AND SPECIMEN PREPARATION 17
4.4 DATA PROCESSING 19
4.4.1 Monotonic Injection 19
4.4.2 Cyclic Injection 21
5. RESULTS OF MONOTONIC INJECTION 22
5.1 WATER FRACTURING 22
5.1.1 G2 Series 22
5.1.2 G3 Series 24
5.1.3 Data Summary 27
5.2 FOAM FRACTURING 31
5.2.1 G2 Series 31
5.2.2 G3 Series 34
5.2.3 Data Summary 37
5.3 COMPARISON OF WATER AND FOAM FRACTURING FOR MONOTONIC INJECTION 44
5.3.1 Fracture Initiation Characteristics 44
5.3.2 Breakdown Characteristics 44
5.3.3 Fracture Surface Characteristics 44
6. RESULTS OF CYCLIC INJECTION 46
6.1 WATER FRACTURING 46
6.1.1 G2 Series 46
6.1.2 Data Summary 50

6.2 FOAM FRACTURING 51
6.2.1 G2 Series 51
6.2.2 G3 Series 55
6.2.3 Data Summary 58
6.3 SUMMARY OF CYCLIC RESULTS 64
6.3.1 Experimental Technique 64
6.3.2 Responses of Granite 64
7. DISCUSSIONS OF FRACTURING RESULTS 66
7.1 FAILURE MODE AND LOCAL STRESS 66
7.2 INJECTION MODULUS 67
7.3 CRACK GROWTH AND INJECTIVITY VARIATION 69
7.3.1 Crack Growth 69
7.3.2 Injectivity Enhancement 70
7.3.3 Cyclic Injection 71
7.4 WATER REDUCTION AND REPLACEMENT 72
7.4.1 Monotonic Injection 72
7.4.2 Cyclic Injection 74
7.5 CYCLIC FATIGUE 75
7.5.1 Mechanical Fatigue 75
7.5.2 Hydraulic Fatigue 75
7.5.3 Field Cyclic Fatigue 76
8. FOAM CHARACTERIZATION 78
8.1 TEST SETUP AT TEMPLE UNIVERSITY 78
8.2 CANDIDATE FOAMS 79
8.3 EXPERIMENTAL RESULTS 80
8.3.1 Thermal Stability of AOS Foams 80
8.3.2 Foam Data Assembly 83
8.3.3 Analysis and Discussion 84
9. CONCLUSION AND FUTURE WORK 89
9.1 INJECTION SYSTEM AND INJECTION TESTING 89
9.1.1 Foam Testing System 89
9.1.2 Experimental Results 89
9.2 FOAM CHARACTERIZATION 90
9.2.1 Foam Testing System and Candidate Foams 90
9.2.2 Experimental Results 90
9.3 FUTURE WORK 90
9.3.1 Foam Fracturing Testing 90
9.3.2 Numerical Study 92
9.3.3 Foam Stability Study 92
9.3.4 Downhole Device Development 92
10. ACKNOWLEDGMENTS 93
11. REFERENCES 94
Appendix A. Critical components for foam fracturing system A-3

LIST OF TABLES

Table 1 Summary of foam generator designs 6
Table 2 Classification according to pressure level 6
Table 3 Dimensions of blind hole specimens in mm 18
Table 4 Granite specimens and fracturing conditions 18
Table 5 Pressure and mass rate for water fracturing under monotonic injection 30
Table 6 Injectivity index and injection mass for water fracturing under monotonic injection 30
Table 7 Injection modulus for water fracturing under monotonic injection 30
Table 8 Pressure and mass rate for foam fracturing under monotonic injection 42
Table 9 Injectivity index and injection mass for foam fracturing under monotonic injection 43
Table 10 Injection modulus for foam fracturing under monotonic injection 43
Table 11 Foam density and quality for foam fracturing under monotonic injection 43
Table 12 Mass rate and mass of water in fluid for foam fracturing under monotonic injection 43
Table 13 Gas mass rate ration for foam fracturing under monotonic injection 43
Table 14 Cyclic results with water as fracturing fluid 51
Table 15 Pressure and Nf obtained for cyclic injection tests using foam as a fracturing fluid 63
Table 16 Density, quality, and gas MRR obtained for cyclic injection tests using foam as a fracturing fluid 63
Table 17 Curve fitting coefficients of fatigue test data 65
Table 18 Inner tangential stress for thick-walled cylinder 67
Table 19 Surfactants used in this study 79
Table 20 Stabilizing agents used in this study 79
Table 21 Fitting results to Equation 15 at 600 psi, 800 psi and 1000 psi. 85
Table 22 Fitting results to the power law model (Equation 16) and the exponential model (Equation 17) at 100°C. 86
Table 23 Fitting results to the power law model (Equation 16) and the exponential model (Equation 17) at 150°C. 86
Table 24 Fitting results to the power law model (Equation 16) and the exponential model (Equation 17) at 200°C. 87
Table 25 Components for liquid section A-3
Table 26 Components for gas section A-4
Table 27 Components for foam section A-4

LIST OF FIGURES

Figure 1 Schematics of (a) layout and (b) controlling lines for foam testing system. GC- gas cylinder, TK- tank, PM- pump, AC- accumulator, PR – pressure regulator, RD – rupture disk, NV – needle valve, FM – (mass) flow meter, CV – control valve, CK – check valve, IF – inline filter, PV – pulsed valve, BPR – back pressure regulator, PS – pressure sensor, SP – specimen; suffixes 1, 2 and 3 refer to either liquid, gas, foam or dual valves in PV, respectively. The three dash boxes in (a) from top to bottom correspond to liquid and gas section, foam generation, and foam injection, respectively. 14
Figure 2 Components of liquid section, gas section, foam generation, and foam injection (from right to left) 14
Figure 3 Pressurization as a function of time for (a) static and (b) pulsed injection tests. PR3- pressure regulator for foam; PV1, and PV2 – pulsed valves whose status is 0 when closed and 1 when open. t1 and t2 define on and off durations at PV1. 16
Figure 4 Flowchart of testing procedures; CV1, CV2, and CV3 are control valves for liquid, gas, and foam; PR3 is pressure regulator for foam; PV2 is pulsed valve in discharge line; NV3 is needle valve for specimen; BPR is back pressure regulator. Refer to Figure 1 for relevant components. 17
Figure 5 (a) Diagram for assembling pressure tube with granite specimen, (b) an assembled specimen, G2 series. Specimen was assembled using a high temperature epoxy; 6.35 mm open hole section was designed as an injection zone, whose length is measured by L_p; specimens were air dry before testing. 18
Figure 6 Diagrams showing pressure as a function of (a) time and (b) mass. Definitions of injection modulus, injection modulus (IM) and filling amount identified, m_0; Pi, mi – pressure and injection mass at fracture initiation; Pb, mb – pressure and injection mass at breakdown. Markers have following meanings: triangle – pressurization initiation, inverted triangle – fracture initiation, square – breakdown. Same comments apply whenever applicable 20
Figure 7 Responses as a function of time for g2019: (a) pressure & mass rate, (b) injectivity index. INI – fracture initiation, BKD – breakdown; same comments apply in the following. 23
Figure 8 Pressure as a function of mass for g2019. 23
Figure 9 Video-based process for g2019, water as a fracturing fluid: for (a) event #1: 85.37 s, water leak in bottom as indicated by arrow; (b) #5: 93.23 s transverse crack coalescence on top, indicated by arrow; (c) #8: 94.22 s transverse crack coalescence extended; (d) #9: 95.38 s large fracture creation and outflow 24
Figure 10 (a) and (b) Images of tested specimen for g2019, showing a slant fracture in two orientations 24
Figure 11 Responses as a function of time for g3001: (a) pressure & mass rate, (b) injectivity index 25
Figure 12 Pressure as a function of mass for g3001. 25
Figure 13 Video-based process for g3001: (a) #1 at 152.05 sec, axial fracture and water leaking; (a) #4 197.05 sec, large water ejection 26
Figure 14 Image of tested specimen for g3001; no visible fracture on the surface of specimen after removed from the testing line. 26
Figure 15 (a) Pressure, (b) mass rate, and (c) injectivity index as a function of mass for G2 series water fracturing under monotonic injection. 28

Figure 16 (a) Pressure, (b) mass rate, and (c) injectivity index as a function of mass for G3 series water fracturing under monotonic injection 29
Figure 17 Responses as a function of time for g2013: (a) pressure, mass rate & density, (b) foam injectivity index, (c) density, (d) quality, (e) mass rate ratio, (f) mass rate 32
Figure 18 Pressure as a function of mass for g2013. 33
Figure 19 Video-based process for g2013 for events (a) #1: 49.55 s, fracture initiated; (b) #2: 56.51 s mixture ejection; (c) #5: 57.66 s increased ejection; (d) #6: 58.26 s, breakup. 34
Figure 20 (a) and (b) Images of tested specimen for g2013 in two orientations, showing a primary axial fracture with secondary transverse fracture. The red dash line illustrates the transverse fracture in one half of the split. 34
Figure 21 Responses as a function of time for g3011: (a) pressure, mass rate & density, (b) foam injectivity index, (c) density, (d) quality, (e) mass rate ratio, (f) mass rate. 36
Figure 22 Pressure as a function of mass for g3011. 36
Figure 23 Video-based process for g3011 for selected events. (a) #3: 36.27 sec, slant fracture emerged; (b) #6: 36.42 sec, breakup 37
Figure 24 (a) and (b) Images of tested specimen for g3011 in two different orientations. Red dash line delineates the secondary transverse fracture. 37
Figure 25 (a) Pressure, (b) mass rate and (c) injectivity index as a function of mass for G2 series foam fracturing under monotonic injection 38
Figure 26 (a) Density, (b) quality and (c) gas mass rate ratio as a function of mass for G2 series foam fracturing under monotonic injection; transient pulses/ pikes in density were removed. 39
Figure 27 (a) Pressure, (b) mass rate and (c) injectivity index as a function of mass for G3 series foam fracturing under monotonic injection 40
Figure 28 (a) Density, (b) quality and (c) gas mass rate ratio as a function of mass for G3 series foam fracturing under monotonic injection; transient pulses/ pikes in density were removed. 41
Figure 29 Bar graphs for (a) pressure, (b) mass rate, (c) injectivity index, and (d) mass. All the error bars have a half of standard deviation. IN – fracture initiation; BR – breakdown. 9.52 – G2 series hole diameter in mm; 4.76 – G3 series hole diameter in mm. 45
Figure 30 Bar graph for injection modulus. All the error bars have a half of standard deviation. 9.52 – G2 series hole diameter in mm; 4.76 – G3 series hole diameter in mm. 45
Figure 31 Cyclic injection responses as a function of time for g2009: (a) waveforms of pressure and mass rate, and (b) extreme values of pressure and mass rate, and (c) injectivity index; water as fracturing fluid. 47
Figure 32 Cyclic injection responses as a function time for g2009: pressure and mass rate during (a) middle life and (b) failure cycle, and instantaneous injectivity index during (c) middle life and (d) failure cycle; water as fracturing fluid. Numbers correspond to the events in the footage taken by video camera. 48
Figure 33 Images based on the footage of g2009 where the injection tube is on the right side. (a) #1: 287.69 sec, water leaked in the center upper half; apparently, fracture initiated ahead of the image; (b) #2: 299.36 sec, water eruption was seen; (c-d) #5, 6: 300.73, 300.82 sec, water eruption increased substantially with splash as a sign of breakdown 49
Figure 34 Images of tested specimen for g2009; (b) is the enlarged top part opposite of (a) showing longitudinal fracture. 49
Figure 35 Fatigue responses as a function of number of cycles for G2 series: (a) maximum pressure, (b) maximum mass rate, and (c) pressure peak-based injectivity index 51
Figure 36 Cyclic injection responses as a function of time for g2015 with foam as a fracturing fluid: (a) timed data for pressure, mass rate and density, (b-f) extremes for pressure and mass rate, injectivity index, density, quality, and mass rate ratios. N_f in title is a nominal number based on figure time and cycle period. 53

Figure 37 Cyclic injection responses as a function of time for g2015 with foam as a fracturing fluid: pressure and mass rate in (a) middle life and (b) final cycles, and instantaneous injectivity index in (c) middle life and (d) final cycles. 53
Figure 38 Video-based cyclic injection responses of g2015 with foam as fracturing fluid for events (a) #1: 28.90 s fracture initiated with foam leaking, (b) #4: 132.31 s mixture injection, (c) #5: 132.35 s increased ejection, (d) #6: 132.40 s breakup. 54
Figure 39 (a) and (b) Post-test images of g2015 induced by cyclic injection in two orientations showing axial fractures with secondary transverse fracture. 55
Figure 40 Cyclic injection responses as a function of time for g3014, foam as a fracturing fluid: (a) time data for pressure, mass rate and density, (b-f), extremes for pressure and mass rate, injectivity index, density, quality, and mass rate ratios. 56
Figure 41 Responses as a function of time for g3014: pressure and mass rate in (a) middle life and (b) final cycles, and instantaneous injectivity index in (c) middle life and (d) final cycles 57
Figure 42 Video-based cyclic injection responses of g3014 for events: (a) #2: 49.32 sec, hair crack initiated, (b) #4: 49.42 sec, mixture injection, (c) #5: 49.47 sec, increased ejection, (d) #9: 51.77 sec, breakdown where the foamed area extended more than 2/3 of specimen length. 57
Figure 43 Images of post-test specimen for g3014 in two orientations; red dash line delineates the axial fracture induced by cyclic injection. 58
Figure 44 Cyclic injection responses as a function of number of cycles of G2 series for (a) maximum pressure, (b) maximum mass flow rate; (c) pressure peak-based injectivity index; foam as a fracturing fluid. 59
Figure 45 Cyclic injection responses as a function of number of cycles of G2 series for (a) pressure peak -based density, (b) foam quality; (c) gas mass rate ratio; foam as a fracturing fluid. 60
Figure 46 Cyclic injection responses as a function of number of cycles of G3 series for (a) maximum pressure, (b) maximum mass flow rate; (c) pressure peak-based injectivity index; foam as a fracturing fluid. 61
Figure 47: Cyclic injection responses as a function of number of cycles of G3 series for (a) pressure peak-based density, (b) quality; (c) gas mass rate ratio; foam as a fracturing fluid. 62
Figure 48 Ratios of maximum pressure in cycling to breakdown pressure in monotonic injection as a function of number of cycles to failure: (a) P_{max}/P_b and (b) fitting for pooled data using $y = a + b*\log_{10}(x)$. g21wd – G2 series with water; g21fd – G2 series with foam; g31fd – G3 series with foam; BHC – blind hole cylinder; OHC – open hole cylinder, Mech. – mechanical fatigue. 65
Figure 49 (a) Failure mode and (b) fraction of failure modes. The blind hole is delineated by a dash rectangular box where the shadow area is bonding zone of tube, and the un-shadow area in the bottom is injection zone. 66
Figure 50 Fracture initiation pressures related to injection moduli based on monotonic tests. Labels L and S correspond to G2 and G3 series. Error bars have a half of standard deviation. Same comments apply in the following. 68
Figure 51 Responses of G2 series tests as a function of injection mass: injectivity index for (a) water fracture and (b) foam fracturing; surface fracture size for (c) water fracturing and (d) foam fracturing. 69
Figure 52 Responses of G3 series as a function of injection mass: injectivity index for (a) water fracture and (b) foam fracturing; surface fracture size for (c) water fracturing and (d) foam fracturing. 70
Figure 53 Characteristic injectivity indices based on monotonic injection as related to: (a) mass rate and (b) mass. Mass amount of filling internal tubes was removed. WinF – water in foamed fluid; INI- fracture initiation; BKD- breakdown are presented. 71

Figure 54 Characteristic pressures based on monotonic injection as related to: (a) mass rate and (b) mass. Dashed line delineates the water use reduction direction. Mass amount of filling internal tubes was removed. WinF – water in foamed fluid; INI- fracture initiation; BKD-breakdown are presented..... 73
Figure 55 Differential pressure versus differential mass based on monotonic tests, where the differences are evaluated between fracture initiation and breakdown. WinF – water in foamed fluid..... 74
Figure 56 Diagram of test apparatus for foam testing and characterization. ADP – air driven pump, PG – pressure gauge, NV – needle valve, PRV – pressure relieve valve, AU – accumulator, PR – pressure regulator, LFM – liquid flow meter, GFM – gas flow meter, FG – foam generator, BPR – back pressure regulator, M1 – microscope for foam height, M2 – microscope for foam bubble size, SVC – sapphire view cell, G1 – glass window for foam height, G2 – glass window for foam bubble size, M – reflecting mirror..... 78
Figure 57 Main components of foam testing and characterization system (from right to left): foam generation section, foam monitoring section, and view cell setup. 79
Figure 58 AOS + Crosslinker foams at 200°C and 1000 psi condition. The two images represent foam (a) after injection, (b) at 50% height..... 80
Figure 59 Thermal stability of foams with different surfactants at 400 psi. 80
Figure 60 Thermal stability of AOS foams at (A)100°C and (B) 200°C..... 81
Figure 61 Thermal stability of AOS + Guar foams at (A)100°C and (B) 200°C..... 81
Figure 62 Thermal stability of AOS + Clay foams at (A)100°C and (B) 200°C. 82
Figure 63 Thermal stability of AOS + Crosslinker foams at (A)100°C and (B) 200°C. 82
Figure 64 Thermal stability of AOS + SiO_2 foams at (A)100°C and (B) 200°C. 83
Figure 65 Thermal stability of AOS + GO foams at (A)100°C and (B) 200°C..... 83
Figure 66 Half-life as a function of temperature and pressure for various aqueous N_2 foams with candidate surfactants and stablizing agents tested in this study..... 84
Figure 67 Exponential fitting curves showing the effect of temperature on foam half-life at 1000 psi..... 85
Figure 68 Exponential and power law curve fitting showing the effect of pressure on foam half-life at 200°C. 86
Figure 69 Comparison of foam half-life data obtained in this study with the published data. 88

ACRONYMS AND ABBREVIATIONS

AC, AU	Accumulator
ADP	Air driven pump
AE	Acoustic emission
AOS	Alfa olefin sulfonate
BHC	Blind hole cylinder
BKD, BR	Breakdown
BPR	Back pressure regulator
CK	Check valve
CMC	Critical micelle concentration
CTAC	Cetyltrimethylammonium chloride
CV	Control valve
DOE	Department of Energy
EGS	Enhanced Geothermal Systems
FEA	Finite element analysis
FG	Foam generator
FM	Flow meter
GC	Gas cylinder
GFM	Gas flow meter
GO	Graphene oxides
GTO	Geothermal Technologies Office
HPG	Hydroxypropyl guar
ID	Inside diameter, identity
IF	Inline filter
II	Injectivity index
IM	Injection modulus
IN, INI	Fracture initiation
LFM	Liquid flow meter
MR	Mass rate
MRR	Mass rate ratio
NP	Nanoparticles
NP – 40	Tergitol™
NV	Needle valve
OD	Outside diameter
OHC	Open hole cylinder
ORNL	Oak Ridge National Laboratory
PG	Pressure gauge
PM	Pump
PR	Pressure regulator
PS	Pressure sensor
PV	Pulsed valve
RD	Rupture disk
SCG	Subcritical crack growth
SDS	Sodium dodecyl sulfonate
SP	Specimen
SS	Stainless steel
SVC	Sapphire view cell
TD	Timed data
TK	Tank

EXECUTIVE SUMMARY

The large thermal gradients and high subsurface temperatures of the western region of the U.S. hold great potential for the implementation of enhanced geothermal systems (EGS). The development of these potential EGS resources requires stimulation of the reservoir to enhance permeability and it has been widely reported that a substantial amount of water will be required should conventional hydraulic stimulation be used. This presents a huge challenge and a high risk to the geothermal development because the water stress[1] in these areas is already high or extremely high. The use of foam, a gas/liquid mixture predominantly composed of gas, in fracturing is considered and explored in this project as a potential approach to address water concerns with hydraulic stimulation in the development of EGS.

This project, led by Oak Ridge National Laboratory (ORNL) in collaboration with Temple University, was awarded in an open lab call in 2018, and was part of the DOE GTO waterless stimulation initiative. The goal of the project was to demonstrate the feasibility of foam fracturing for EGS development through two primary tasks: Task 1: Laboratory study of the effectiveness of foam fracturing for representative geological materials, including cyclic pressurization using foam (led by ORNL) and Task 2: High temperature foam material selection and characterization (led by Temple University).

In FY19, ORNL finished the critical review on serval issues associated with foam fracturing and the implementation of the proposed tasks in a lab study (Wang, et al., 2019), and completed the foam fracturing testing using cement as a model material (Wang, et al, 2020a). The work at ORNL was geared up to develop a brand-new foam testing system in FY20. The purchase of main components for the new system was finished in the first half of the FY20. The assembly of the foam testing system and foam fracturing testing were completed in the second half of the FY20 (Wang, et al., 2021a).

Task 1 required the development of a test system which can be used to perform hydraulic fracturing of geological specimens with both water and foamed liquids at pressure up to 6,000 psi (41.4 MPa). The system possesses several capabilities that conventional injection systems lack for hydraulic fracturing. In addition to its ability to generate foam with controlled quality, it is capable of cycling pressure levels between specified values up to frequencies of 50 Hz. The latter capability was developed to evaluate the hypothesis that cyclic loading of samples would produce enhanced fracturing. The system consists of two sections: one for foam generation and another for foam injection. The foam is generated through separate control and pressurization of liquid and gas phases with controlled flow rates. The injection section is equipped with a low-flow Coriolis flow that monitors the density of foam to ensure the injection is in the range of target foam quality[2].

Experimental results of foam fracturing are reported for cylindrical granite specimens using water and aqueous N_2 foam as the fracturing fluids. All experiments were performed for unconfined conditions. The effects of injection mode (i.e., monotonic vs cyclic pressurization) on breakdown pressure and failure response sample were investigated using water alone as a fracturing fluid and foams with a range of compositions. It was found that in the case of monotonic injection, the breakdown pressure of granite specimens tended to be slightly higher when fracturing with foam. Additionally, with a foam quality of 90%, the water use can be reduced by 50 to 84%, depending on hole size. On the other hand, it was observed that the breakdown pressure can be brought down to 70% of the monotonic breakdown pressure by using low cycle fatigue. Finally, discussions are presented regarding injectivity and water use reduction.

[1] Measures total annual water withdrawals (municipal, industrial, and agricultural) expressed as a percentage of water available

[2] Gas volumetric fraction in mixture

These experimental results and observations demonstrated in the lab the feasibility of using foam fracturing to reduce the use of water in hydraulic stimulation. Currently, the foam fracturing data on subject rock materials with EGS are not available, although the foam stimulation was practiced in oil and gas fields. This hinders the application of this technology under the conditions of EGS. The current study has established a solid foundation for pursuing advanced study in a more realistic simulating environment. The reduction of breakdown pressure is extremely important for the EGS development and has the potential to address another challenge of stimulation-induced reservoir micro-seismicity. The reservoir-related seismicity has paused several EGS projects around the world and is a critical issue confronted by the large-scale EGS development for geothermal power generation. In addition, the reduction of breakdown pressure can reduce the burden of the surface pumps. The benefits originating from the reduced breakdown pressure justify the application of cyclic injection in the EGS sites, although the use of such an injection scheme may require more pump energy.

Task 2 began with an extensive literature survey and an online database was developed to facilitate the identification of candidate foams. The literature survey revealed that there is no data available for foam stability at temperature levels relevant to geothermal applications. For example, prior work for high-temperature Oil & Gas applications performed testing only up to 150 ^{o}C. This absence of high-temperature foam stability data for industry standard foam compositions by itself highlights a significant gap that the project addressed in order to evaluate the potential use and effectiveness for geothermal applications.

A foam testing apparatus was built as part of task 2 to test and characterize the foam stability. The upper limit temperature and pressure capabilities of the apparatus evolved over the course of the project. Candidate foams with N_2 and CO_2 as a dispersed phase were identified and tested in FY19 (Thakore, et al., 2020). Foam testing and characterization in FY20 were continued on N_2 but with the temperature raised to 200^{o}C and pressure to 400 psi (2.8 MPa) (Thakore, et al., 2021). In FY21, the experimental work was carried out with the pressure range extended to 1,000 psi (13.8 MPa; Thakore, et al., 2022). The foam testing apparatus uses a water bath to pre-heat the foam line and an oil bath to maintain the target foam temperature and currently has a pressure limit of 2,000 psi (13.8 MPa). The system is equipped with a high-pressure view cell to visually monitor and quantitatively evaluate foam stability.

The high-temperature stability of aqueous N_2 foams with different surfactants and stabilizing agents was tested to 200^{o}C and 1,000 psi (6.9 MPa). Foam stability was characterized by the half-life, which is defined as the time a foam takes to decrease to 50% of its original height. The candidate surfactants included alfa olefin sulfonate (AOS), sodium dodecyl sulfonate (SDS), Tergitol^{TM} (NP – 40), and cetyltrimethylammonium chloride (CTAC). Besides guar gum, bentonite clay, crosslinker, recently emerged stabilizing agents were also studied, including SiO_2 nanoparticles (NP) and graphene oxide (GO) dispersion. The results showed that foam stability decreased as temperature increased as expected, but foams became relatively stable as pressure increased. Within the tested ranges of temperature and pressure, the crosslinker as a stabilizing agent demonstrated the best thermal stability performance, next came with GO and SiO_2 NPs. The maximum half-life of any foam tested at 200^{o}C and 1,000 psi (6.9 MPa) was approximately 20 minutes.

These results significantly advanced our understanding of the stabilizing agents such as crosslinker with the data available at much higher levels of temperature and pressure. Moreover, the identification of runner ups like SiO_2 and GO NPs is significant. It offers us the opportunity to further enhance the lifetime of foams for EGS with innovated technologies, especially considering that the conventional foams reach the limit on life time improvement, even with a high pressure.

In summary, the most noteworthy findings of this work are:

1. A foam fracturing test system has been developed at ORNL, which can be used to perform foam fracturing under pressure up to 6,000 psi. The system monitors foam density during fracturing online and is capable of testing materials in both monotonic and cyclic (up to 50 Hz) injections.
2. Foam fracturing tests were carried out on Charcoal black granite specimens with a blind borehole to the middle length. Two diameters of blind borehole were tested; G2 series: 9.53 and G3 series: 4.76 mm. N2-in-water foam was used with AOS as a surfactant.
3. There was a hole-size effect on fracture initiation pressure. The effect is smaller in the case of foam, which was influenced by the high penetrability of gas in foam. Breakdown pressure showed a behaver just as that of fracture pressure; namely an increased value for small hole samples, while the effect in water fracture was more impressive than in foam fracture.
4. Water mass was reduced in foam fracturing within similar range of breakdown pressures. In G2 series, it was decreased from 10.44 g for water fracturing to 5.17 g, representing more than 50% water reduction. Therefore, there is the potential to reduce water use in EGS stimulation through foam fracturing.
5. Use of cyclic injection has the potential to reduce the breakdown pressure and seismicity in EGS application. Experiments using 4-s cycle period found that specimens can be fractured with a low number of cycles. The fatigue pressure was approximately 64 - 77% of monotonic breakdown pressure for water fracturing and 58 - 94% of the breakdown pressure for foam fracturing.
6. A foam stability testing system has been developed that can test foam at 220 Deg C to 2,000 psi. Tested components of candidate foams included two gases: N_2 and CO_2; 4 surfactants: AOS, SDS, NP-40 and CTAC; 5 stabilizing agents: guar, bentonite clay, borate salt, silica NPs, and GO.
7. N_2 and AOS provided the most stable performance over the tested ranges. Furthermore, the AOS foam with stabilizing agents of guar and borate salt (crosslinker) offered the highest half-life of 20 minutes at 200 Deg C and 1,000 psi.
8. Arrhenius equation and modified power law have been demonstrated to fit well the half-time vs. temperature and pressure data, respectively. These relations can be useful to provide the suggestion for future foam stability study.

1. BACKGROUND

Foam fracturing is considered as a potential approach to address water availability challenges with development of enhanced geothermal systems (EGS). Currently, EGS relies on water for hydraulic stimulation to create the fracture network required for extraction of geothermal energy. One study of the use of water in geothermal plant development estimated that nearly 2 million gallons (7,570 m^3) per MW are required for EGS reservoir stimulation (Clark et al. 2011). To achieve the U.S. DOE goal of 60 GW of geothermal power generation capacity by the year 2050 (U.S. DOE, 2019), approximately 120 billion gallons (454 million m^3) of water would be needed for hydraulic stimulation if alternatives to hydraulic stimulation are not developed. This does not consider water needs for well construction such as drilling and cementing. The challenge of meeting resource needs for EGS well construction and completion is further compounded by the fact that the majority of the most promising potential EGS sources in the U.S. are located in the regions where water stress is high or extremely high (Blackwell et al., 2011; Freyman, 2014). Therefore, technology innovation is needed to overcome technical and non-technical barriers and to mitigate the upfront cost and risk with reservoir stimulation. This study aims at assessing the feasibility of foam fracturing to overcome these barriers as part of the U.S. DOE waterless stimulation initiative.

Foam is an immiscible mixture of liquid and gaseous phases that behaves quite differently from the individual constituent phases. For example, the viscosity of foam can be many times that of single phases like water or gas, depending on the quality of foam (gas volumetric fraction in mixture). The tunable properties of foam have been shown to be extremely attractive to EGS reservoir engineering. The high viscosity can reduce fluid leakage, increase fracture width, and improve proppant transportation, while it is compressible with high energy storage capabilities, providing sustained driving force for fracture propagation. Additionally, the gas has very high penetrability to the stressed body to create more complete fractures. Generally, an optimal foam performance can be obtained when the quality is 70% or higher (Faroughi et al., 2018). The implication is that a substantial amount of water can be replaced by the gaseous phase and, therefore, the usage of water can be reduced accordingly.

Foam fracturing has been used on a very limited basis in oil and gas fields dating back to the 1970's, primarily in low pressure and low permeability formations, but continues to be a subject of research investigation with additional technical challenges related to EGS implementation. EGS reservoir conditions and lithologies are substantially different from those of oil and gas. The earth stresses and temperature are generally higher and prospective EGS reservoirs are typically composed of rocks such as granite, which has higher strength and orders of magnitude less permeability than the typical sedimentary rocks in conventional oil and gas reservoirs. The stability and stimulation effectiveness of foam fluids for these conditions is an open question along with additional concerns related to mitigation of induced seismicity. We propose to evaluate the stability and effectiveness of foamed fluids for EGS scenarios and use pulsed or cyclic injection to address these challenges. This is a new concept with many potential advantages including more efficient and reduced water usage and improved control of reservoir seismicity. Some research considerations and preliminary work using model material have been reported previously (Wang et al., 2019; 2020a). In the following, a brief review on the relevant issues is provided.

2. INTRODUCTION

2.1 FOAM PREPARATION

2.1.1 General Requirements and Field Preparation

Foam is typically defined by a term called quality which specifies the volumetric fraction of dispersed phase (gas) in a mixture of gas and liquid. In the field, the pressurized liquid and gas phases of calculated mass flow rates are pumped separately and comingled to form the foam. To obtain target downhole quality, the surface quality needs to be prepared to accommodate the compressibility of the gas phase (Chambers, 1994). N_2 is in a gas phase when mixing with the liquid phase. CO_2 is in a liquid phase when mixing with the liquid phase on the surface, and it may transfer into a super-critical state or gas, according to the downhole temperature.

In the injection zone, the foam is characteristically polydisperse and disordered (Faroughi et al., 2018). Typically, a foam quality of around 70% is used for foam stimulation in oil & gas applications because it offers a viscosity that optimizes proppant transport capacity with foam characteristics.

2.1.2 Preparation in Laboratory

The success of foam stimulation in the field triggered substantial laboratory studies to understand the foam behavior and optimize the stimulation design by using the experimental results. Mixing is generally performed by one of two methods (Table 1). One method is the static mixer where the liquid and gas phases are mixed by either 1) opposite jets in the cases of low pressure (Fry and French, 1951; Khan et al., 1988; Wanniarachchi et al., 2018) and high pressure (Reidenbach et al.,1986; Herzhaft et al., 2005; Sun et al., 2014; Xue et al., 2016), or 2) side jet for low pressure (Saint-Jalmes et al., 1999) and for high pressure (Wendorff & Earl, 1983; Reidenbach et al., 1986; Enzendorfer et al., 1995; Gu and Mohanty, 2015; Akhtar, 2017). The term static refers to the absence of moving mechanical parts in the mixing process. In the case of side jet, the liquid is generally introduced into the flow line before the gas phase is injected through a downstream tee section or side inlet. Single or double inlets can be used. Additional internal structures can be added to this method to homogenize the foam including pebble bed, steel wools, gauge disks, and so on. The bubble snap-off and bubble division are involved, depending on the capillary number (Ca). It has been demonstrated that the relative bubble size (the ratio of bubble length to the capillary tube radius) decreased with the increasing Ca number.

Another method is the rotor (Kroezen et al., 1988) or the impeller blender (Hutchins and Miller, 2005; Ahmed et al., 2018). The gas and liquid are introduced simultaneously into a chamber where the mixing of gas and liquid are accomplished by rotating. There was no detailed explanation of the foaming mechanism of the impeller in the reported references. In the centrifugal field of a stator-rotor mixer, the air collects as a thin air conus around the shaft (Kroezen et al., 1988). The rest of the annular space is filled with the foam phase, which moves as a plug flow through the mixer in the axial direction. The mixing process consists of dispersing air from the gas conus into the foam phase. The mixing of air from the gas conus occurs by the dispersion of air from a cavity behind the rotor pins. As a result of the rotation of the rotor pins, a local under-pressure occurs at the back of the rotor pins. The gas flows from the gas conus to the cavity behind the rotor pins and is dispersed in the foam phase.

In both the static and dynamic mixers, the foamability of foam depends on the Reynold's number (Re) of wetting liquid phase with a sufficient Re number needed to obtain a uniform foam.

Table 1 Summary of foam generator designs

Designer	Type	Configuration	Inlets/ outlet	Ref.
MIT	Static mixer	Chamber 117 mm length, 4.57 mm ID (0.25" OD, 0.035" THK, 0.18" ID); packed with 1.6 g SS wool to 96.6 mm	Liquid 50 psi, N_2 40 psi	Khan et al, 1988
UCLA	Jet	Chamber 50 mm length, 5 mm ID, with a capillary hole of 2 mm length, 0.7 mm diam	Liquid 120 psi, N_2 80 psi	Saint-Jalmes et al., 1999
Leoben	Jet	Cell 120 mm length, including a capillary hole of 2 mm diam, a chamber filled with 20/40 mesh sand (main grain diameter 800 μm)	Liquid, N_2; foam pressure 9 MPa, temp 60°C	Enzendorfer et al., 1995
U Twente	Rotor	Chamber height 40 mm (8 × 5 mm), head diam 45 mm	Liquid, air	Kroezen et al., 1988
UT-Austin	Static mixer	Chamber 113 mm length, 3.8 mm ID, with glass bead diameter 180 μm, pore throat size 28 - 75 μm	Liquid, CO_2; foam pressure 20 MPa, 50°C	Xue et al, 2016
UC Berkeley	Static mixer	Capillary tube, 1 to 2 mm diameter in straight section, and 200 to 400 μm diameter in neck section	Liquid, air	Gauglitz et al., 1988

Depending on the purpose of the foam, a foam line can be designed to be single-pass or a closed loop as shown in Table 2. The single pass line is simpler in its system configuration, but foam control is more challenging for a single pass line because it requires significant trial and error attempts to tune injection parameters and obtain the desired uniformity of foam, especially in the case of the static mixer. In many cases, the foam quality is controlled by using the flow rates of the gas and liquid phase and the amount of injection time. Previous uses of this type of system include the viscosity studies at small and large amplitudes under ambient condition and experimentation related to foam fracturing. The single pass line was very popular in earlier days, and the foam is generated at a low pressure (around 100 psi), so that it doesn't need high-pressure equipment.

The closed loop is the main approach currently used for foam characterization, especially the viscosity. Reported systems have been designed to be pressurized to as high as 69 MPa to study pressure effects on foam stability (Wendorff & Earl, 1983). Some reported systems are equipped with heating features for the study of temperature effects. The loop is usually configured with several pipes with varying inside diameters to test the foam in different shear rates. Because of the loop feature, the foamed fluid can be circled as long as it is required to obtain a desired uniformity of foam. A densitometer and view cell are usually included for online foam monitoring. Closed loop systems can be very long depending on the length of piping required for the establishment of laminar flow.

Table 2 Classification according to pressure level

Pressure level	Configuration	Working mode	Case
Low pressure	Single-pass	Simultaneously mixing	Fry and French, 1951; Khan et al., 1988;
Low pressure	Single-pass	Addition & flow controls	Saint-Jalmes et al., 1999
High pressure	Single-pass	Simultaneously mixing	Kroezen et al., 1988; Sun et al., 2014;
	Single-pass	Addition & flow controls	Wendorff & Earl, 1983; Enzendorfer et al., 1995;
High pressure	Loop	Addition	Akhtar, 2017;
	Loop	Simultaneously mixing & addition	Herzhaft et al., 2005; Hutchins & Miller, 2005;

2.2 FOAM APPLICATION

2.2.1 Foam Generation and Delivery

Maintaining foam stability and viscosity is critical to create a required width of fracture and ensure proppant transport capacity of foam for the subsequent stimulation and after-fracturing pressure release (Valko & Economides, 1997; Faroughi et al., 2018). In the latter, the proppants are used to keep the fracture stimulated open. There is some discussion regarding the use of proppant in an enhanced geothermal system to uphold the conductivity of rock mass obtained by the stimulation (McClure & Horne, 2014; Mattson et al., 2016).

The foam generated by field surface equipment (typically a fluid pump, N_2 pump, and liquid additive pump for surfactant) is pumped downhole to the injection zone for a stimulation job. This journey through the wellbore and into the reservoir has motivated much prior study related to its effects. Pressure head loss and the stability of the foam in the downhole condition are among two critical issues that have been investigated by others.

The pipe viscometer has been used to investigate the viscosity of foams so that pressure loss in the wellbore can be calculated. The study of foam viscosity under various environmental condition can be used to address the effect of temperatures and pressures in the field (Reidenbach et al., 1986; Faroughi et al., 2018) so that stimulation, particularly the pump, can be designed.

The aging or stability of foam has received considerable research attention and is affected by both environmental change during downhole foam delivery and the residence time in subsequent foam injection. Both static and dynamic stability testing methods are used. In the former, a freshly prepared foam is injected into a graduated tube or cell, and the foam height is monitored. In the latter, the foam is circled within a pipe viscometer and viscosity and bubble appearance are monitored. In both cases, the degradation of foam is signified by a reduction of monitored parameters, for example, foam height (Chambers, 1994; Gu and Mohanty, 2015) and viscosity (Reidenbach et al., 1986; Hutchins and Miller, 2005). The degradation mechanism of foam has been studied quite intensely, including liquid drainage, bubble coarsening, and so on. The breakdown of foam is generally seen with bubble coalescence and collapse (Reidenbach et al., 1986; Harris & Reidenbach, 1987; Faroughi et al., 2018).

2.2.2 Foam Injection and Fracturing

2.2.2.1 Foam injection

Foam stimulation has not yet been practiced in geothermal applications but practiced in shallow and deep oil & gas fields since the 1980's (Harris et al., 1984; Warnock et al., 1985); however, reported details are sparse. On the other hand, those of water injection in conventional hydraulic stimulation are available and thus reviewed here. The injection schedule is carefully planned, executed, and monitored based on formation lithology, reservoir conditions, and desired foam properties. A typical stimulation usually starts with a pilot or pre-stimulation injection with a low rate to detect the injectivity of wellbore, and then a regular injection (MIT, 2006). The soft or cyclic stimulation has been proposed (Zimmermann et al., 2010; Zang et al., 2013), demonstrated by mine-scale experiments in the Aspo Hard Rock Laboratory, Sweden (Zang et al., 2017; Zang et al., 2019; Zimmermann et al., 2019), and recently deployed in Pohang EGS site in Korea with some success (Hofmann et al., 2018; Hofmann et al., 2019).

The injection scheme consists of multi-steps with different periods in cycles varying from hours to days in long term injection, from minutes to hours in mediate term, and from seconds to minutes in short term or pulsed injection (Hofmann et al., 2018). Stepwise injection rate is integrated into the pressurization and de-pressurization half cycles. The different time periods of design take care of energy release and fatigue of rock under various magnitudes of injection rate. The acoustic events serve as an input for the evaluation of related seismicity and offer a guidance for the next injection implementation. Another common consideration in field stimulation is mitigation of side effects to the environment. The control of induced seismicity in particular has received considerable attention because of its societal impacts and potential to cause project suspension (Majer et al., 2007; McGarr, 2014; Lee et al., 2019).

The use of cyclic injection for hydraulic stimulation is not common field practice but is being actively investigated in several labs around the world, including those studying sandstone (Patel et al., 2017) and granite (Zhuang et al., 2019b). Data from cyclic injection experiments on geological materials are consistent with fatigue theory with failure resulting from the growth of cracks within the material (Cerfontaine & Collin, 2018). Water is also believed to play a role in the process by weakening the chemical bond of the material near the crack tip due to stress corrosion. In most of the experiments published so far, the amplitude used in cyclic injection is close to the pressure of fracture initiation in a monotonic injection. Monitoring of acoustic events during pressurization has been associated with the propagation of cracks within the sample prior to catastrophic failure, and the number of cycles to failure for pressure levels near monotonic breakdown pressures is generally low. However, the maximum pressure required for breakdown in cycling experiments has been shown to be generally lower than the breakdown pressure in a monotonic injection. This is significant because it can potentially reduce the stresses on pumping equipment, reducing maintenance costs, and can potentially reduce induced seismicity onset. Cyclic injection has also been reported to produce a fracture network with more small-scale cracks with better connectivity (Zang et al., 2013; Hofmann et al., 2018).

2.2.2.2 Fracturing

The goal of hydraulic stimulation is to enhance the permeability of rock by creating an interconnected fracture network. In the field, this is achieved through either reactivating a natural fracture system or creating a new fracture system (McClure & Horne, 2014; Xie et al., 2015). Both approaches are relevant for future EGS applications, but the current study investigates approaches for producing new fractures in rock.

Rock fracture is initiated by stress conditions and depends on material mechanical properties that are influenced by composition, microstructure, secondary phase content, and external parameters like strain/ loading rate (Hubbert & Willis, 1957; Haimson and Fairhurst, 1969). The porosity and the connectivity of pores play an important role in the hydraulic fracture as the pressurized fluid would be coupled with the solid; the pore pressure of the liquid phase alters the stress state and affects the failure, and the stress of the solid structure also influences the permeability (Detournay and Cheng, 1988).

The penetrability of the fluid also has an impact on the fracturing process, depending on the viscosity of the fluid (Christopher, 2015). It has been observed that the fracture breakdown pressure is related to the viscosity of the fracturing fluid with a higher viscosity corresponding to a higher fracture breakdown pressure (Valko & Economides, 1997). This has been demonstrated in fracturing of both single-phase fluids (Li et al., 2015; Jia et al., 2018) and foamed fluids (Wanniarachchi et al., 2018). The effects of pressure loss and energy dissipation due to flow resistance through the wellbore and from the wellbore to the fracture tip has also been considered in past work (Munson et al., 2009; Valko & Economides, 1997).

Fracture typically initiates when bulk material strength is locally exceeded due to a combination of in situ stress state and stress concentration factors. Once initiated, the fracture follows a path of minimum

resistance and propagates (Wang and Tao, 1995; Valko & Economides, 1997). It has also been observed that the fracture morphology can depend on the ability of fracturing fluid to penetrate into pore space and release stored energy. For example, Jia et al. (2018) and Wanniarachchi et al. (2018) have shown that fracture path exhibits more tortuosity when a compressible phase was used for both single phase and foamed fluids. This is generally dominated by the high gas permeability of the subject rock. Moreover, the fracturing induced by foam was found to be more extensive than that by water due to the compressibility of the foam and its ability to continue to deliver energy to the crack tip after fracture initiation (Young & Graham, 1999).

2.3 FOAMS

2.3.1 Compositions

Foams are classified as aqueous or non-aqueous, depending on liquid phase. For the aqueous foams, the liquid phase is water. In the case of non-aqueous foams, liquid phases can be hydrocarbons (Chambers, 1994).

There are mainly two dispersed phases used currently in foam stimulation in oil and gas fields (Chambers, 1994; Kohshour et al., 2017; Faroughi et al., 2018). N_2 is the most widely used gas because of its chemical inertness and availability. It can also be isolated by liquefaction and fractional distillation. The main drawback of N_2 is its low density and its application in stimulation is mainly for shallow reservoirs. CO_2 foam has also been successfully applied in the stimulation of several unconventional oil and gas reservoirs where it has improved reservoir productivity (Harris et al., 1984; Warnock et al., 1985). It can be obtained from pre-existing CO_2 reservoirs, chemical plants, and coal power plants (Jacobs, 2014; Olasolo et al., 2016). The density of CO_2 is much higher than N_2. CO_2 is less stable than N_2 and it can dissolve in liquids in a certain temperature range which limits its use as a foam.

Air is less reported as the dispersed phase in foam stimulation. Air foam was explored by Young and Graham (1999) and Young (2002) to fracture concrete and rocks as an alternative to explosive for concrete stripping and rock breakage. There is a potential for gas phase in foam application as the chemical and physical properties of air approach those of N_2, and air is readily available.

It is well known that the foam is subject to aging. This is significant for at least two aspects: 1) there is a need to maintain the structural integrity of the foam for it to function as a pressurizing medium as designed, and 2) the need also exists for the foam to maintain the desired viscosity in fracturing for fracture width and proppant transport (Valko & Economides, 1997). If aged, the gas bubbles could be coarsened or coalesced and finally broken, leading to separation of the liquid phase from the gas phase. The surface tension and behavior of the liquid film interface dominates these processes and the stability of foams. For a foam to be practically usable in reservoir stimulation, surfactants are usually used to reduce the surface tension. In this case, the surfactant is mixed with the liquid phase solution in a specified concentration before foam generation. There exists a concentration level, called critical micelle concentration (CMC) (Abdul et al., 1990). Above this limit, the surfactant stays free in the aqueous phase, and surface tension remains constant. Alfa olefin sulfonate (AOS), an anion surfactant, is most widely used in the field and most widely studied in the laboratory. Other popular surfactants include sodium dodecyl sulfonate (SDS), Tergitol ™ (NP – 40), and cetyltrimethylammonium chloride (CTAC). Gelling agents are also introduced to tune the performance of the liquid phase, where the increase in viscosity can mitigate or stop the drainage in the plateau (Faroughi et al., 2018).

2.3.2 Effects of Temperature and Pressure

The aging of foam depends on the temperature and pressure. Increased temperature accelerates the diffusion of the gas phase and thinning of the liquid phase. This enhances the coarsening and coalescence of gas bubbles and drainage of liquid, ultimately reducing foam life (Harris and Reidenbach, 1987; Harris, 1995; Faroughi et al., 2018). The effect of pressure on foam stability has received less research attention in the past. At a given temperature and concentration of stabilizing agents, one may find that the foam stability increases with increasing pressure (Cawiezel and Niles, 1987; Gu and Mohanty, 2015): 1) the overall effect of pressure depends greatly on the surfactant type and concentration (Liu et al., 2005). 2) The properties of the gaseous dispersed phase, including gas permeability and solubility in the aqueous phase, also affect the foam stability. For example, the degree of pressure's effect appeared to be higher in CO_2 than N_2 due to its closeness of density to water in an aqueous foam (Harris, 1995; Faroughi et al., 2018).

2.3.3 Stabilizing Agents and Emerging Strategy

Stabilizing agents are added to the liquid solution to enhance the foam stability in extreme environments. Gelling agents like hydroxypropyl guar (HPG) have been studied for this purpose. At ambient conditions, these polymer solutions may raise viscosities of foams to 0.1 Pa*s at the expected shear level found in a fracture. At temperatures below 115^{o}C, borate cross linkers may be workable. But for higher temperatures, organometallic crosslinkers are necessary (Valko & Economides, 1997).

Recently, solid nanoparticles like silica (SiO_2) and graphene oxide (GO) have been introduced into the liquid phase to extend the foam life (Cote et al., 2011; Lv et al., 2015; Faroughi et al., 2018). It was observed that the nanoparticles in the film or plateau can reduce surface tension and reduce drainage. The hydrophobicity of particles obtained by surface coating was shown to increase the lifetime of the foam (Yu et al., 2014).

2.4 TECHNICAL GAPS

Foam generation is practiced from case to case without a standardized procedure. There is no specification of Ca and Ra numbers to generate a uniform foam. No commercial products for a foam generator are available either.

Stimulation in unconventional oil & gas fields is typically around 3 km terminal depth but can occur in the 4-5 km range. For EGS, well terminal depth is expected to range between 4-6 km and formation temperatures are expected to be significantly higher than for oil & gas applications (Beckers et al., 2014). In situ stress will also be higher than is typical for oil & gas. There is very limited data on the performance of foams in such conditions.

With respect to cyclic injection, prior experimental work in hydraulic fracturing is generally limited to water as a fracturing fluid. The pressurization and de-pressurization have typically been controlled either through operation of pumps or electric valves and the frequency of pressurization has tended to be low, typically no greater than 5 Hz. There has also been very limited study of the use of foamed and other energized (compressible) for rock fracturing.

This project addresses the following gaps related to the use of foam fracturing and cyclic pressurization for EGS:

- Evaluation of the stability of foams at high temperature conditions (i.e., temperatures above 200 ^{o}C)

- Evaluation of the effects of high frequency cyclic pressurization on rock fracture (on the order of 1 Hz) including comparison of fracture behavior using liquid and foam fluids

2.5 OUTLINE OF REPORT

This project performed laboratory studies to evaluate the potential for foam fracturing as a waterless approach to the stimulation of enhanced geothermal systems. The main efforts were to develop a foam fracturing testing system, to perform experimental work on the foam fracturing of rocks, to identify the candidate foams, and to perform testing and characterization of foams at target temperatures and pressures.

The report is structured as follows. In Chapter 3, ORNL's foam fracturing testing system is introduced. The system has a capability of conducting foam fracturing in both monotonic and cyclic injection modes with a pressure rating of 6,000 psi (41.4 MPa). Unlike a conventional system relying on operation of a pump or electric valve for cyclic injection, the new system employs dual pneumatically- driven valves to generate pressure pulses. The system offers a wide range of cycling frequency, enabling the investigation of rock fracture in various domains. In Chapter 4, the experimental techniques are presented, including test plan, specimen preparation, and data processing.

Experimental results for granite fracture testing are presented in Chapters 5 to 7. The granite specimens tested were cylindrical in shape and were pressurized through blind holes along the axis of the sample. The diameter and height of the specimens were 2" (50.8 mm) and 4" (101.6 mm), respectively.

The research activities at Temple University are described in Chapter 8. This work was focused on high temperature characterization of foams. To accomplish this goal, an apparatus was developed that can perform the foam testing at temperatures up to 200°C, and pressures up to 2,000 psi (13.8 MPa). The candidate surfactants included AOS, SDS, NP – 40, and CTAC. Besides guar gum, bentonite clay and crosslinker, recently emerged stabilizing agents were also studied, including SiO_2 nanoparticles, and graphene oxide dispersion. The results showed that foam stability decreased dramatically as temperature increased.

Finally in Chapter 9, the conclusions and discussions are given regarding the future work to address the immediate experimental needs in foam fracturing, and to understand the competing mechanisms of pressure and temperature in the foam stability through data analysis and experimentation with an extended testing range.

3. FOAM FRACTURING TESTING SYSTEM

The foam fracturing testing system consists of a foam generation section, foam injection section and specimen section. A schematic of the system is shown in Figure 1. Images of the gas, liquid, foam generation and foam injection sections are shown in Figure 2.

Foam is produced by mixing pressurized liquid and gas phases in a pre-determined volumetric ratio. In the liquid line, a solution is pressurized using an air-driven pump (PM1) that has a maximum outlet pressure of 8,875 psi (61.2 MPa). A 1-gallon bladder accumulator (AC1) is used to attenuate the pressure fluctuation and to store the liquid for subsequent operation. A pressure regulator (PR1) is used to set the pressure level with the help of a needle valve (NV1). Thereafter, an electric control valve (CV1) is used to control the flow rate of the liquid line with the input from a thermal mass flow meter (FM1). In parallel to the gas line, a second electric control valve (CV2) is used to control the flow rate of gas with the input from another thermal mass flow meter (FM2). The pressurized gas is supplied by a 6,000- psi (41.4 MPa) gas cylinder. The pressure level and flow rate are also preset by the pressure regulator and an installed needle valve. Both lines have a check valve (CK1 or CK2) to prevent backflow before they mix at the tee connector.

The foam mixture is homogenized by passing through an in-line filter (IF) before being stored in another bladder accumulator (AC3). The pressure and flow rate in the foam line are preset by a pressure regulator PR3 and a back pressure regulator BPR; the foam flow rate is controlled by an electric control valve (CV3) with the input from a Coriolis mass flow meter (FM3). Flow control valves CV1, CV2, and CV3 are operated using a WATLOW controller. In cyclic injection mode, valves PV1 and PV2 are used to increase or decrease pressure delivered to the specimen (SP). PV1 and PV2 are electrically controlled, pneumatically driven valves. The dual valves are controlled by a timer to cycle pressure for pulsed fracturing experiments. The WATLOW controller and the timer for PVs are mounted in a control panel.

Pressure gauges are installed next to the pressure sources to monitor the outlet pressures including pump, gas cylinder, and pressure regulators. A pressure sensor is installed ahead of the specimen to measure the pressure applied. The signals from the pressure sensor and the mass flow meters are acquired using an MC USB-230 series device. The foam density signal measured by FM3 is acquired by a Bronkhorst FlowPlot. A client server, FlowDDE, needs to be started to run the FlowPlot. A video camera is set aside to record the fracturing process. The video data were processed and synchronized with the signals from the data acquisition offline.

316 stainless steel (SS) tubes are used in all the sections but with different sizes. The gas line is sized with 1/16” (1.588 mm) outside diameter (OD) and 0.022” (0.559 mm) inside diameter (ID); the liquid and foam lines are sized with ¼” (6.350 mm) OD and 0.152” (3.861 mm) ID.

All the devices, tubes and fittings are rated to pressure of at least 6,000 psi (41.4 MPa). The specifications of the main components can be found in Appendix A.

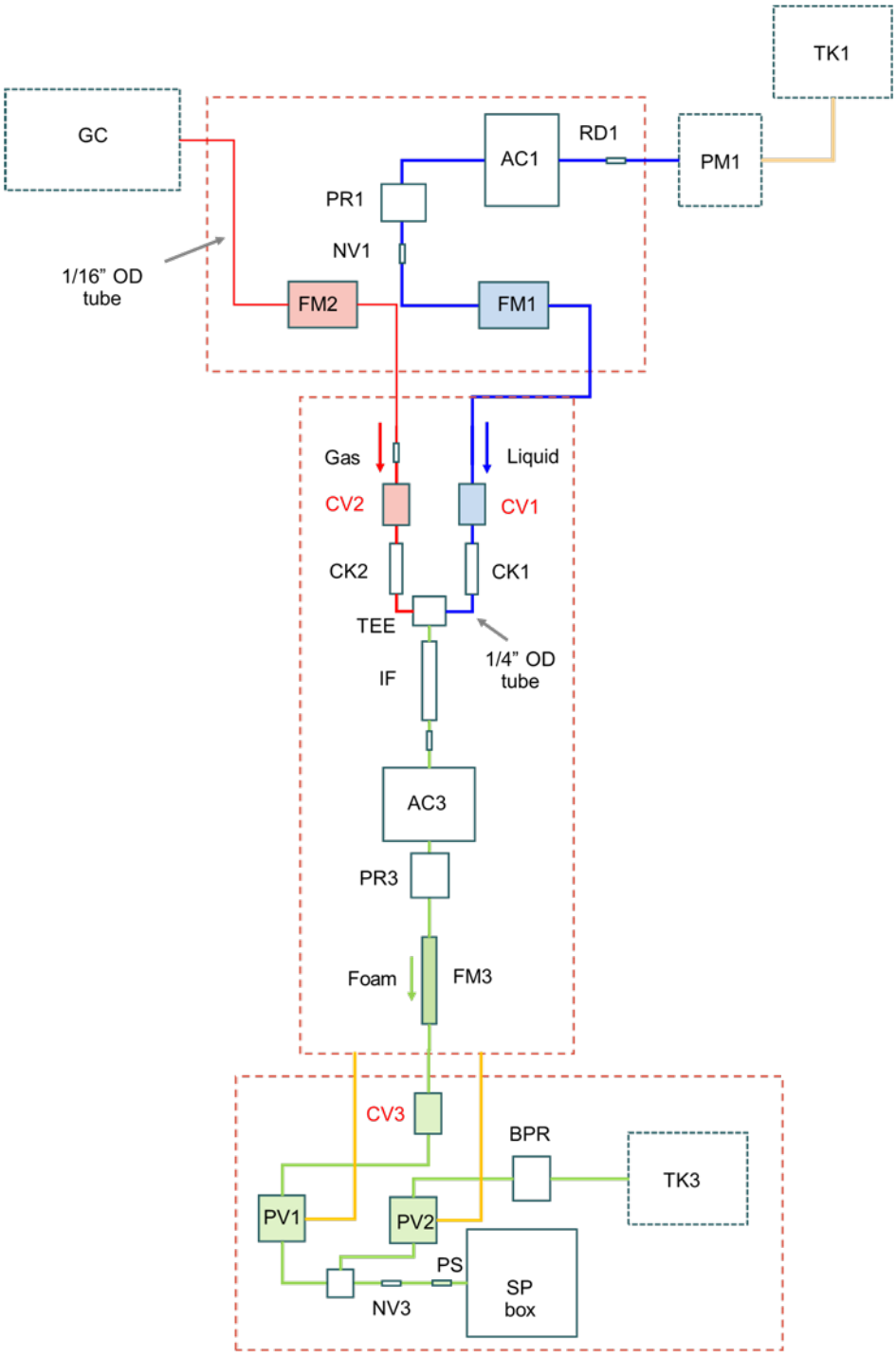
TK1
GC
AC1
RD1
PM1
PR1
NV1
1/16" OD
tube
FM2
FM1
Gas
Liquid
CV2
CV1
CK2
CK1
TEE
1/4" OD
tube
IF
AC3
PR3
Foam
FM3
CV3
BPR
TK3
PV1
PV2
PS
SP
box
NV3

(a)

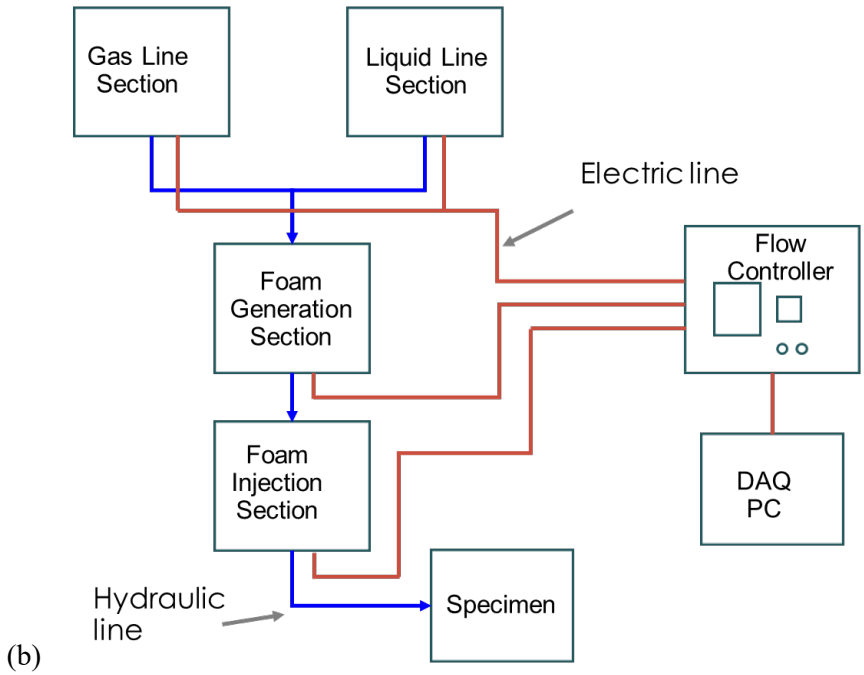

Figure 1 Schematics of (a) layout and (b) controlling lines for foam testing system. GC- gas cylinder, TK- tank, PM- pump, AC- accumulator, PR – pressure regulator, RD – rupture disk, NV – needle valve, FM – (mass) flow meter, CV – control valve, CK – check valve, IF – inline filter, PV – pulsed valve, BPR – back pressure regulator, PS – pressure sensor, SP – specimen; suffixes 1, 2 and 3 refer to either liquid, gas, foam or dual valves in PV, respectively. The three dash boxes in (a) from top to bottom correspond to liquid and gas section, foam generation, and foam injection, respectively.

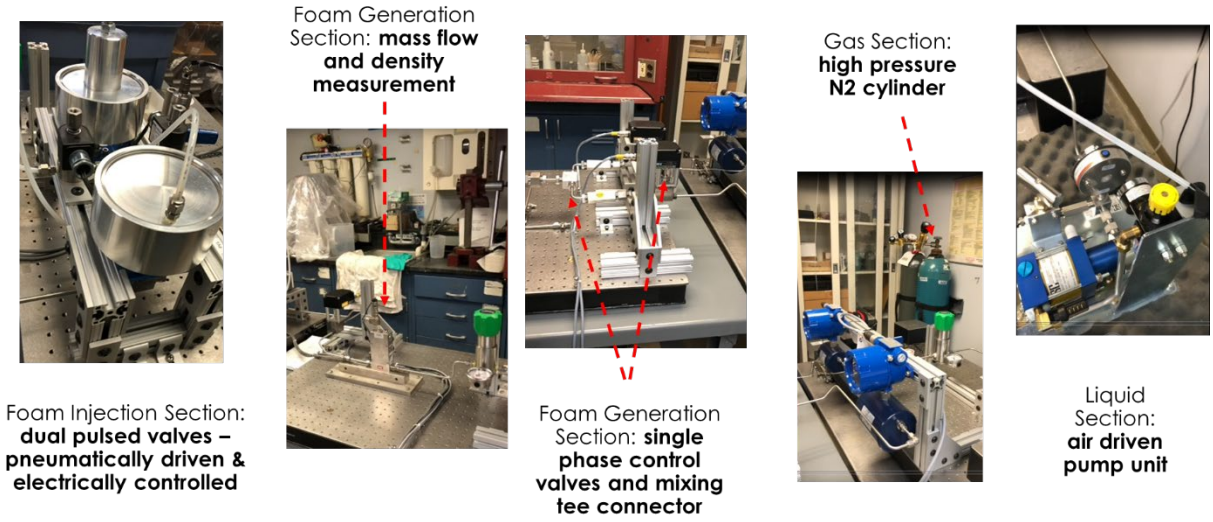

Figure 2 Components of liquid section, gas section, foam generation, and foam injection (from right to left)

4. FOAM FRACTURING TESTING TECHNIQUE

4.1 TEST PLAN

4.1.1 Monotonic Injection

Testing under monotonic is designed to be quasi-static such that the pressurizing rate, defined by P_{max}/t_{max} (Figure 3), has insignificant effect on data interpretation.

No standard is available currently for hydraulic fracturing testing. The test plan utilized for the project references standard ASTM D3967-16, which specifies that loading rates between 0.05 and 0.35 MPa/s can be used for quasistatic loading. This is consistent with prior laboratory and field test experiences (Li et al., 2015; Wanniarachchi et al., 2018; Valko and Economides, 1997).

4.1.2 Cyclic injection

Cyclic or pulsed injection tests vary pressure values between a maximum pressure, P_{max}, and a minimum pressure, P_{min}, as shown in Figure 3. With the current configuration, P_{min} can be as low as zero. In this study, tests were performed at a pulse rate of 0.25 Hz with 50% duty cycle. Given a pulse frequency, the pressure curve can be characterized using pressure amplitude,

$$P_a = (P_{max} - P_{min})/2, \quad \textit{Equation 1}$$

and mean pressure,

$$P_m = (P_{max} + P_{min})/2, \quad \textit{Equation 2}$$

During the cycling, the status of PV1 and PV2 altered out-of-phase while the outlet pressure at PR3 is being maintained at a target level. The cycling goes to pressurization when PV1 is open and PV2 is closed, and to de-pressurization vice versa.

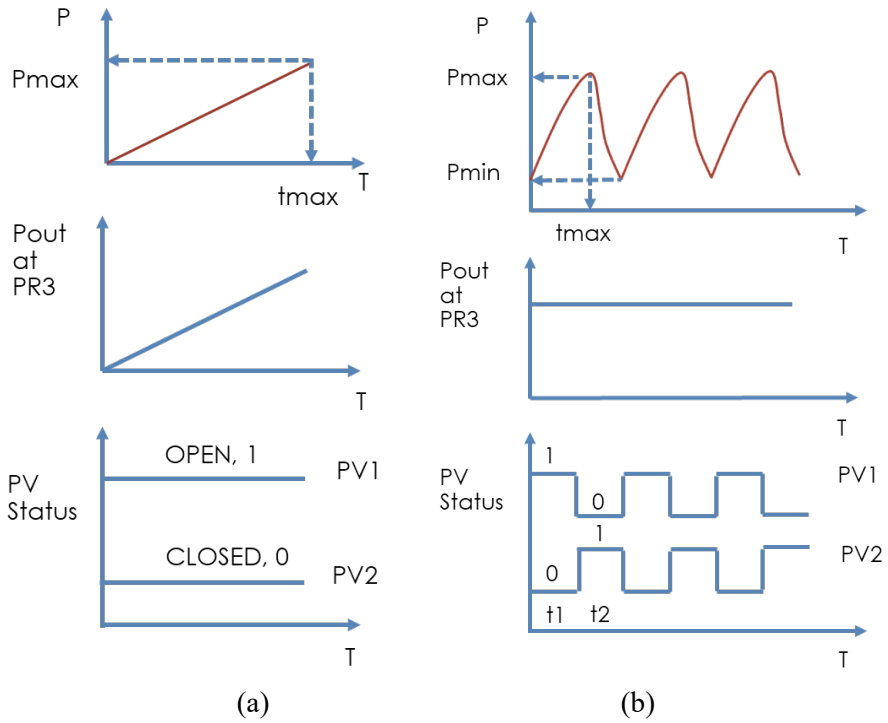

Figure 3 Pressurization as a function of time for (a) static and (b) pulsed injection tests. PR3- pressure regulator for foam; PV1, and PV2 – pulsed valves whose status is 0 when closed and 1 when open. t1 and t2 define on and off durations at PV1.

4.2 PROCEDURES

A typical test generally consists of two steps (Figure 4): foam generation and foam injection. The former begins with setting up the pressure and mass flow rate in the gas and liquid lines. The process then uses PR3 and BPR to maintain a specific foam mass rate set point while adjusting CV1, CV2 and, if necessary, CV3 to achieve a target foam density. The adjustment of these CVs is done manually on the controller. After the target foam density has been obtained, foam is injected into the test specimen.

In the case of monotonic injection, the pressurization is applied by manually turning the PR3. For the cyclic injection, a timer is used to automate the process. In this study, a 4-sec period was used in cyclic injection defined by a 2-sec pulse length and a 2-sec pulse delay, equivalent to 50% duty cycle. The pressure is oscillated between high- and low- pressure values.

Cyclic stimulation has been used in EGS field development before (Zimmermann et al., 2010; Chabora and Zemach, 2013). These previous efforts controlled pumping operations at the surface with pressure cycling accomplished by intermittent fluid injection over periods of hours or days. The approach in this study is quite different in that high frequency pressure cycling is explored without cessation of pumping (i.e., pressure is cycled between a high- and low- pressure value). This functionality is accomplished by the active control of flow valves and enables controlled exploration of the potential for stimulating rock failure by fatigue.

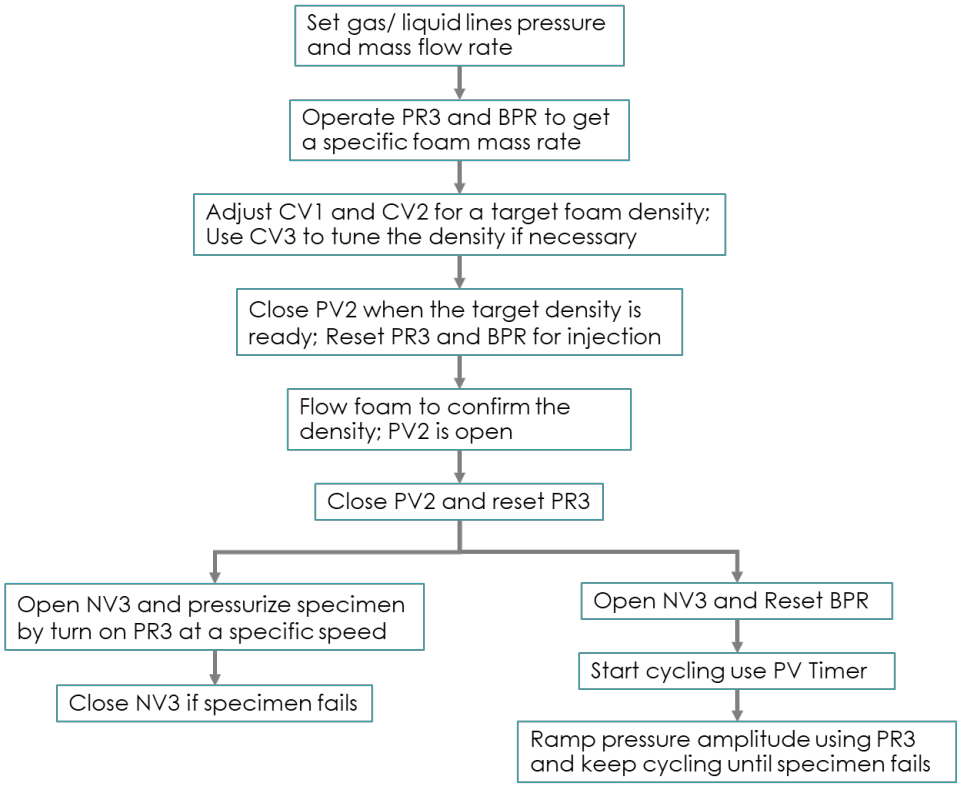

Figure 4 Flowchart of testing procedures; CV1, CV2, and CV3 are control valves for liquid, gas, and foam; PR3 is pressure regulator for foam; PV2 is pulsed valve in discharge line; NV3 is needle valve for specimen; BPR is back pressure regulator. Refer to Figure 1 for relevant components.

4.3 MATERIALS AND SPECIMEN PREPARATION

Granite is one type of rocks widely seen in EGS sites around the world (Xie et al., 2015) and was therefore examined in this work. Charcoal Black granite used in this study was supplied by Coldspring (Cold Spring, MN). This material was studied previously (Lu et al., 2015). The modulus of rupture is 16.7 MPa based on ASTM C99 according to the supplier (Coldspring, 2022). The longitudinal wave velocity was measured in this study to be 4,082 ± 111 m/s, and the shear wave velocity was measured to be 2,711 ± 91 m/s. The sound velocities obtained fall within the range of typical granite (Jaeger et al., 2007).

Granite specimens were cylinders sized with 50.80 mm in diameter, and 101.60 mm in length. All samples were internally pressurized through a blind borehole drilled to the axial mid-point of the specimen. The blind hole specimen was employed because the configuration resembles the stimulation condition in the field (Li et al., 2015; Wanniarachchi et al., 2018). There were two series of specimens tested: G2 series with hole diameter 3/8” (9.530 mm), and G3 series with hole diameter 3/16” (4.763 mm). All the specimens were air dried.

A 316 SS tube served as a fluid conduit to the borehole. The tube was sized with 6.35 mm OD × 3.861 mm ID for G2 series, and 1.588 mm OD × 0.559 mm ID for G3 series. The OD of the tube was bonded to the hole surface using a high-strength epoxy (3M DP420, St. Paul, MN), which was allowed to cure for at least 24 hours before fracturing testing. The low-end 6.35 mm of the tube/ borehole was free of epoxy, serving as an injection zone. The tube was also extended about 44.45 mm out of the specimen for a fitting connection. Two O-rings were installed to prevent the epoxy from flowing to the bottom of the blind hole. The length of bonding was selected to withstand pullout of the tube at a specified pressure level. The

same configuration of specimen – tube assembly was used in the study of cement foam fracturing (Wang et al., 2020a). The relevant specimen information related to the tests in this report can be found in Figure 5 and Table 3.

A range of candidate foams were studied for the potential use in waterless stimulation of EGS. For the fracturing study, the primary candidates of interest were aqueous N_2-based foams. Experimental fracturing testing to date has used N_2 as a gaseous phase. The foam quality was more than 90% in monotonic injection and a little lower in cyclic injection. AOS with 1 wt.% concentration was used as a surfactant. The relevant properties of the aqueous N_2 foams can be found in Thakore et al. (2020; 2021; 2022).

A total of 40 specimens were prepared for monotonic and cyclic injections. The specimens for various injection conditions and fracturing fluids are summarized in Table 4.

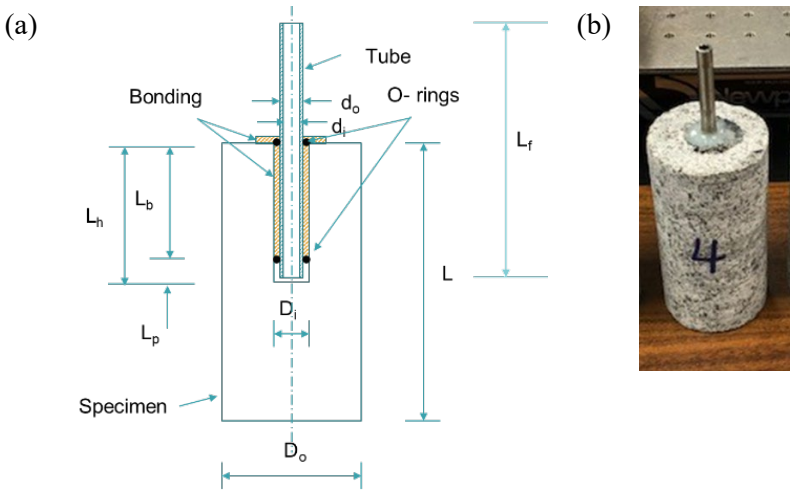

Figure 5 (a) Diagram for assembling pressure tube with granite specimen, (b) an assembled specimen, G2 series. Specimen was assembled using a high temperature epoxy; 6.35 mm open hole section was designed as an injection zone, whose length is measured by L_p; specimens were air dry before testing.

Table 3 Dimensions of blind hole specimens in mm

	L	Do	Di	do	di	Lh	Lb	Lp	Lt
G2	101.600	50.800	9.525	6.350	3.861	50.800	44.450	6.350	95.25
G3	101.600	50.800	4.763	1.588	0.559	50.800	44.450	6.350	95.25

Note: refer to Figure 5 for the quantities in the Table

Table 4 Granite specimens and fracturing conditions

Injection mode	Monotonic		Cyclic		Spec. label
Fluid	Water	Foam	Water	Foam	
G2 series	#3,4,5,19,20	#11,12,13,22,23	#6,7,8,9,10	#14,15,16,17,18	g20*
G3 series	#1,2,3,4,5	#6,7,8,9,10,11,12,13		#14,15,16,17	g30*

Note: g2022: preloaded; g2023: no density data; g3006,07,08: density was too high; g3012: no sensor data; g3017: no cycling involved with the failure

4.4 DATA PROCESSING

4.4.1 Monotonic Injection

Data processing for monotonic injection testing was performed to obtain a set of quantities for characterization, including injectivity index (II), injection modulus (IM), foam quality (Γ), and mass rate ratios (MRR, η) of gas and water. Generally, the timed data were obtained, and the characteristic points of the quantities corresponding to fracture initiation and breakdown were identified.

The mass for each phase is obtained through an integral of mass (flow) rate or

$$m_i = \int \dot{m}_i \, dt,$$

Equation 3

where m is the mass in grams and $\dot{m}$ the mass rate output from the flow meters, g/min; subscript i = f, g, w, each representing foam, gas, and water, respectively. The mass flow meter, calibrated by the manufacturer, was also verified in the lab by using the mass collected at a specified time.

The foam quality (Γ), defined as a ratio of gas volume to foam volume (gas plus liquid), can be expressed by

$$\Gamma = \frac{\rho_w - \rho_f}{\rho_w - \rho_g},$$

Equation 4

where subscripts w, g and f have same meanings as before. ρ_w= 1000 kg/m^3 and ρ_f is measured by the Coriolis mass flow meter. The gas density, ρ_g, is estimated according to

$$\rho_{g2} = \frac{P_2}{T_2}\frac{T_1}{P_1}\rho_{g1},$$

Equation 5

where ρ is density in kg/m^3; T temperature in ^{o}C; subscripts 1 and 2 represent gas conditions; and P pressure in MPa measured by the pressure sensor (Valvias, 2020). Because our tests were carried out at room temperature, we have T_1= T_2; the two items thus cancelled out in Equation 5. In this study, conditions 1 and 2 refer to ambient and pressurized conditions, respectively. At the ambient condition, P_1 = 14.5 psi (0.1 MPa), N_2 density ρ_{g1} = 1.25 kg/m^3. Once the gas pressure is given, the gas density under pressurized condition can be calculated.

The gas mass rate, $\dot{m}_g$, can be estimated according to

$$\dot{m}_g = \Gamma \frac{\rho_g}{\rho_f}\dot{m}_f,$$

Equation 6

and water mass rate, $\dot{m}_w$, can be obtained using mass equilibrium by

$$\dot{m}_w = \dot{m}_f - \dot{m}_g.$$

Equation 7

Injectivity index, denoted by II, is a measure of fluid taken in a specified time under a specified pressure. For each phase, it is calculated by

$$II_i = \frac{\dot{m}_i}{P},$$

Equation 8

where II is in g/(min*MPa), subscript i = f, g, w as defined above. The II was utilized also in previous experimental work to evaluate the effect of hydraulic fracturing (Zhuang et al., 2019).

Furthermore, mass ratio (MR, ξ) and mass rate ratio (MRR, η) are defined to characterize the extent of water reduction or replacement,

$$\xi_i = \frac{m_i}{m_f},$$

Equation 9

$$\eta_i = \frac{\dot{m}_i}{\dot{m}_f},$$

Equation 10

where subscript i = g, w as defined above.

The injection quantities can be presented in the time domain or expressed as a function of injected fluid mass (Figure 6). In the time domain, the events of fracture initiation and breakdown in a fracturing test can be identified from timed sensor data and verified by video data. The fracture initiation is generally related to the change of pressurization rate and the first discontinuous mass rate rise. Meanwhile, the breakdown was identified with either peak pressure or the second abrupt mass rate rise. The videos revealed the water leaking following the fracture initiation and fracture propagation, and the water ejection with the breakdown; these events can be used to confirm the identified fracture initiation and breakdown. The fracture initiation and breakdown were reported and investigated in previous studies on hydraulic fracturing with pressurization rate control (Zoback et al., 1977; Detournay & Carbonell, 1997), and were examined in this project. On the other hand, data presented in terms of mass allows us to focus more on fracturing responses of rock tested.

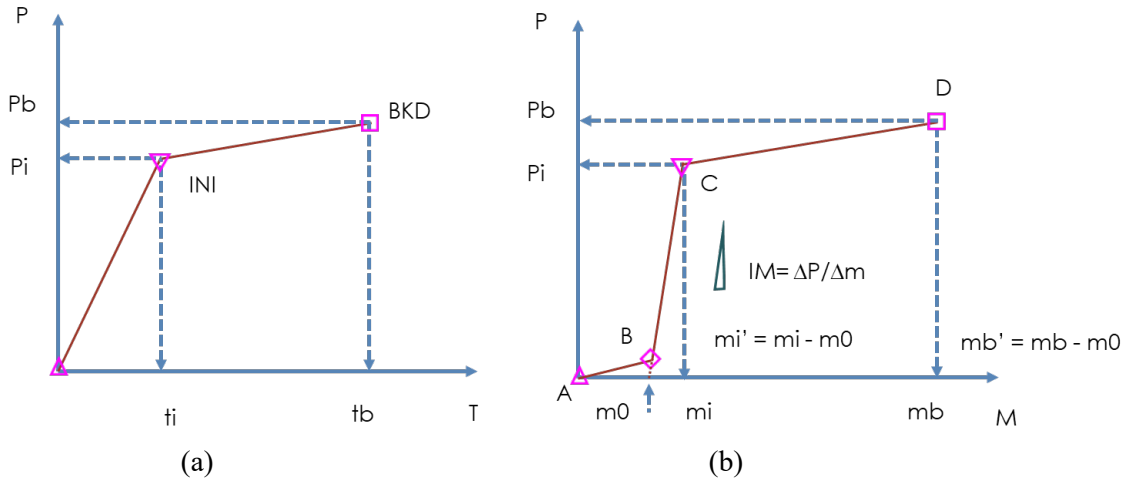

Figure 6 Diagrams showing pressure as a function of (a) time and (b) mass. Definitions of injection modulus, injection modulus (IM) and filling amount identified, m_0; Pi, mi – pressure and injection mass at fracture initiation; Pb, mb – pressure and injection

mass at breakdown. Markers have following meanings: triangle – pressurization initiation, inverted triangle – fracture initiation, square – breakdown. Same comments apply whenever applicable.

4.4.2 Cyclic Injection

Data processing for cyclic injection testing examines the waveform of timed data of pressure, mass rate, injectivity index, and additional quantities including density, foam quality, and mass rate ratio when the fracturing fluid is foam.

Furthermore, the cyclic data were analyzed to obtain the maximum and minimum values of monitoring quantities in each cycle. They include pressure, mass rate, density, and derivatives such as injectivity index, foam quality, and mass (rate) ratios. These quantities are used in the subsequent characterization of material responses.

5. RESULTS OF MONOTONIC INJECTION

5.1 WATER FRACTURING

5.1.1 G2 Series

Monotonic injection tests were completed for five samples in the G2 series: g2003 to g2005, g2019 and g2020. All the specimens were tested to failure in around 110 sec with breakdown pressures ranging from 14.6 to 21.6 MPa. No surface fracture can be seen for post-tested g2003 to g2005, while g2019 and g2020 showed a slant fracture. Experiment videos were recorded for g2019 and g2020 for offline data analysis. This subsection provides main experimental results with an example and a summary of the results.

5.1.1.1 Pressure, mass rate, and injectivity index

Pressure increased steadily as the blind hole of the specimen was filled with a slight decrease in rate at the point of fracture initiation and a maximum pressure value achieved at the point of breakdown. Mass flow rate for a typical experiment is described by the following pattern. There was a brief rise-and-fall in the beginning of the experiment as the hole in the sample is filled followed by a rapid decrease as the sample begins to pressurize. The mass flow rate then increased, indicating fracture initiation and growth. A period of flat rate was seen before another abrupt jump at the breakdown.

The variations with pressure and mass flow rate of g2019 are shown in Figure 7 with fracture initiation and breakdown marked as INI and BKD, respectively. The fracture initiation corresponded to a sudden rise of mass rate near 74 sec. The specimen breakdown was signified by a sudden pressure drop near 94 sec. The breakdown in this specimen was not exactly at the time when the second jump of mass rate occurred but was delayed by about 3 sec. The specimen was still capable of withstanding pressurization before the final failure.

The injectivity index generally decreases with the saturation of rock mass. The events like fracture initiation and specimen breakdown prompted a sudden rise as can be from Figure 7 for g2019. The multi-step intermittent rise of injectivity index reveals that a monotonic injection features a series of cycles of discontinuous energy accumulation and release driven by pressurization and rock fracture.

A plot of pressure as a function of the total mass accumulated, Figure 8, shows a linear increase of pressurization up to the fracture initiation point, INI, and yielding to ultimate breakdown at BKD. A small slope stage preceding the linear pressurization is easily seen, which was attributed to filling of the internal tube as discussed in Section 4.4.1.

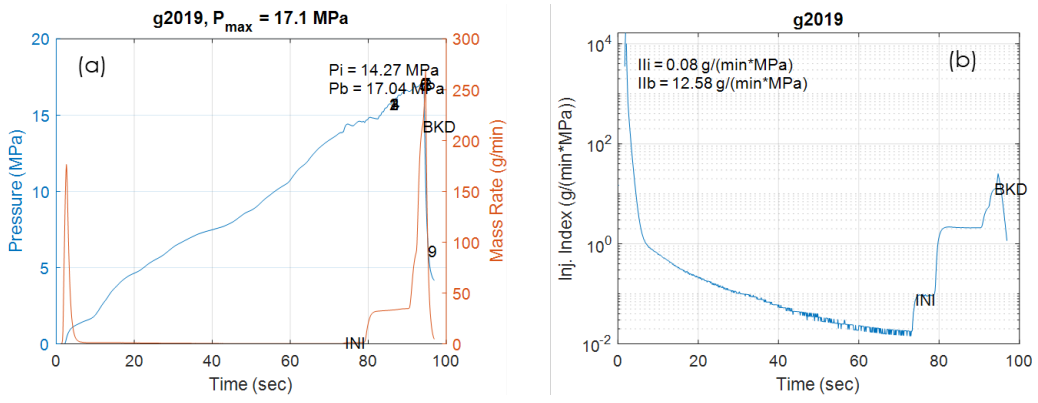

Figure 7 Responses as a function of time for g2019: (a) pressure & mass rate, (b) injectivity index. INI – fracture initiation, BKD – breakdown; same comments apply in the following.

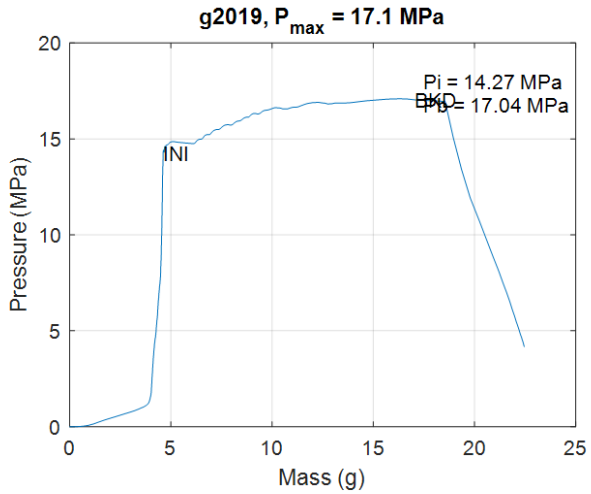

Figure 8 Pressure as a function of mass for g2019.

5.1.1.2 Video and post-test images

Video data offer the evidence of fracture initiation and breakdown identified from the sensor data. At the same time, it also assists us in understanding the failure mechanism involved. In general, water leaking could be seen from fracture initiation and subsequent internal propagation. The wet area became increasingly large when the crack grew, and additional cracks were developed. Finally, water erupted as the cracks/ fractures coalesced and the breakdown took place.

Figure 9 shows a series of images from a footage captured during the test for g2019, as described above, with the following events. The figure times are marked in Figure 7.

- #1: figure time 85.3 sec, water leaked out bottom from back side of specimen; it started earlier than that recorded as seen from flow rise in the figure at 79 sec. The first flow rise signifies the initiation of fracture. The pressure was 14.9 MPa.
- #5 and 8: figure time 93.3 sec and 94.22 sec, transverse cracks formed and coalesced; it is a sign of breakdown. The pressure peaked prior to the breakdown. On the pressure - mass curve, mass was between 14.7 and 18.2 g when the breakdown was approaching.
- #9: figure time 95.3 sec, large fracture creation and outflow.

(a)  (b) 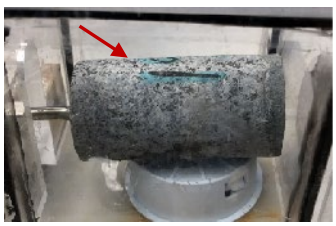

(c) 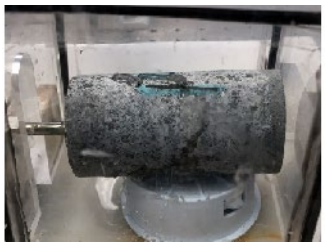 (d) 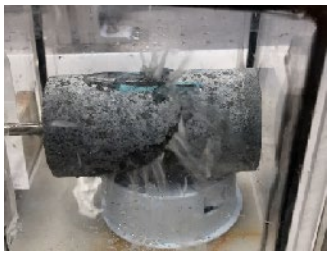

Figure 9 Video-based process for g2019, water as a fracturing fluid: for (a) event #1: 85.37 s, water leak in bottom as indicated by arrow; (b) #5: 93.23 s transverse crack coalescence on top, indicated by arrow; (c) #8: 94.22 s transverse crack coalescence extended; (d) #9: 95.38 s large fracture creation and outflow.

A diagonal fracture near the injection zone was seen from the post-test images of the specimen as shown in Figure 10, corresponding to the video observation.

(a)  (b) 

Figure 10 (a) and (b) Images of tested specimen for g2019, showing a slant fracture in two orientations

5.1.2 G3 Series

Five tests were completed for this series with a typical duration of 100 seconds (g3001 to g3005). The test for g3001 was slightly longer than average with a duration of 182 sec. All the specimens were tested to failure with sensor and video data acquired for all tests. The breakdown pressures ranged from 17.7 to 29.7 MPa. Generally, the surface cracks are barely visible on the post-test specimens. Two specimens, g3003 and g3004, were displayed double axial fractures appearing on the upper half of specimens.

5.1.2.1 Pressure, mass rate and injectivity index

Fracturing of the G3 series exhibited pressurization and mass flow rate behavior similar to the G2 series. The curves of g3001 are given in Figure 11 and Figure 12. Fracture initiation occurred around 151 sec as indicated by a sudden rise in mass flow rate and local drop in pressure. Breakdown took place at approximately191 sec with a substantial increase in mass flow rate as can be seen from the video screen shot shown in Figure 13b.

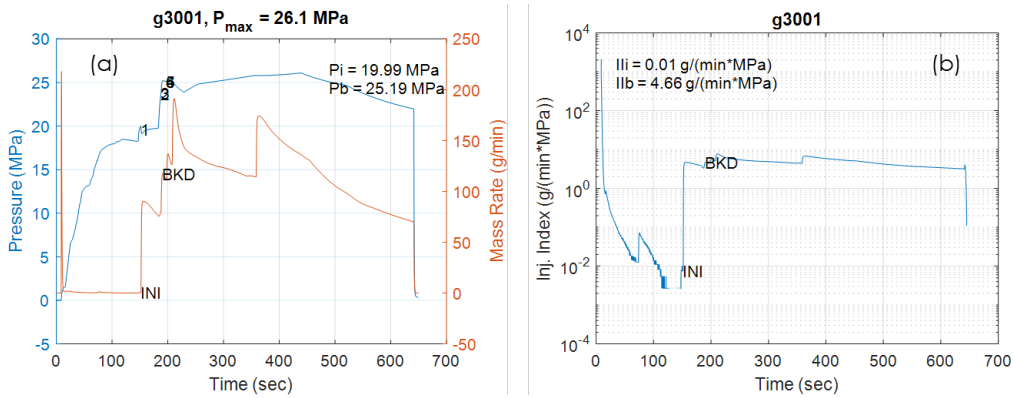

Figure 11 Responses as a function of time for g3001: (a) pressure & mass rate, (b) injectivity index

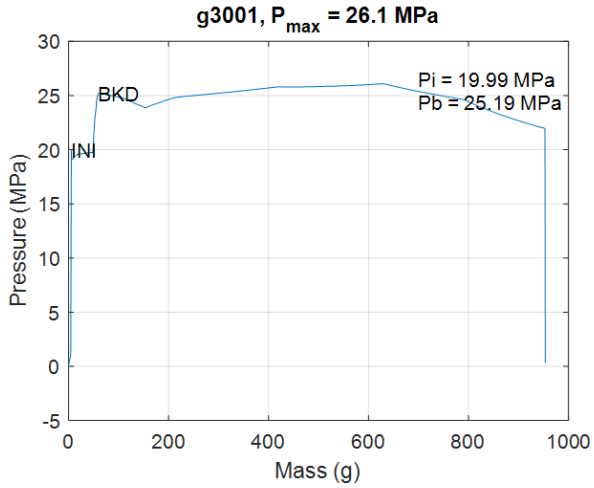

Figure 12 Pressure as a function of mass for g3001.

5.1.2.2 Video and post-test images

The following observations were made from the analysis of experiment videos:

1) The fracture was usually initiated either axially or in a small angle to the axial direction near the bottom of blind hole
2) Surface crack growth from the fracture initiation and outcrop to the final breakdown can be measured
3) Breakdown featured a sizable water eruption, but did not break the specimen into pieces

Figure 13 shows a series of images from footage captured during the test for g3001 with the following events. Figure times are marked as was done for Figure 11.

- #1: figure time 152.05 sec, corresponding to the discontinuous flow rate rise; water leaking with axial fracture sized more than ½ specimen length; fracture initiated apparently before the image
- #4: figure time 197.05 sec, breakdown with large and strong water eruption; fracture extended to 72% of specimen length.

The post-test specimen image in Figure 14 shows no surface fracture even though water is observed exiting the specimen from the video footage. The fracture appears to have closed after the specimen was depressurized. X-ray images were taken for this specimen showing a complex fracture system with axial fractures and transvers fractures near the injection zone (Zhang, 2021).

(a)  (b) 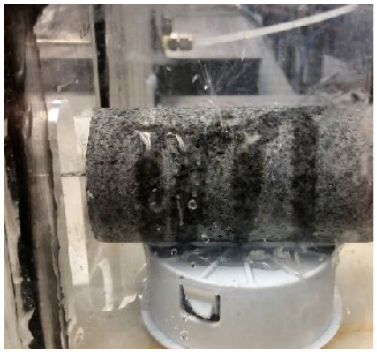

Figure 13 Video-based process for g3001: (a) #1 at 152.05 sec, axial fracture and water leaking; (a) #4 197.05 sec, large water ejection

Figure 14 Image of tested specimen for g3001; no visible fracture on the surface of specimen after removed from the testing line.

5.1.3 Data Summary

5.1.3.1 Comparison of experimental results by series

G2 series

The responses of the rock for this set of experiments are aggregated in Figure 15 as a function of mass injected accumulatively.

- The pressure profile was nominally bilinear with a sharp slope change in pressure between the linear sections of the profile. The higher slope stage ended at fracture initiation around 13.3 – 17.8 MPa with a breakdown pressure of around 14.6 – 21.6 MPa. There was a wide variation range of injected mass at breakdown.
- All mass flow rate curves exhibited a sharp drop near fracture initiation. The minimum was located between 0.2 and 6.5 g/min in the vertical direction.
- The II curves, as defined in Sect. 4.4.1, had a similar shape as the mass rates. Its bottom level was ranged between 0.016 and 0.367 g/(min*MPa). There were multi-steps prior to the breakdown, reflecting the discontinuous injectivity increase due to fracturing; the breakdown II was about one or two magnitude orders higher than pre-fracture level.

(a)

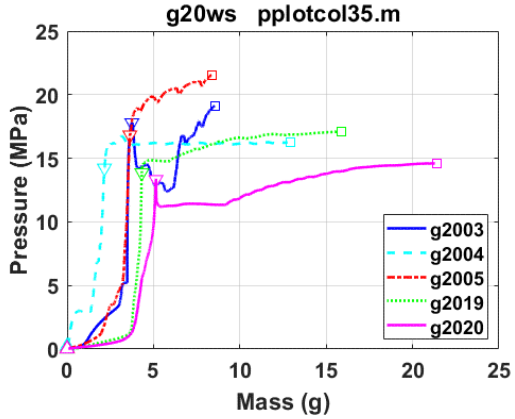

(b)

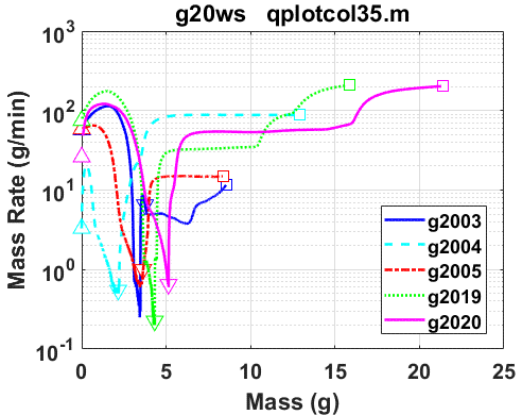

(c)

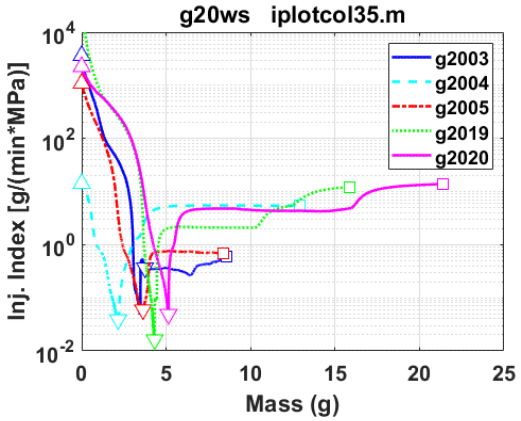

Figure 15 (a) Pressure, (b) mass rate, and (c) injectivity index as a function of mass for G2 series water fracturing under monotonic injection.

G3 series

Plots for G3 series are given in Figure 16.

- The linear stage of pressure curves exhibited a relatively high slope compared to the G2 series. The fracture initiation and breakdown pressures appeared to be higher. The breakdown injection mass was also larger.
- Two specimens, g3003, g3004, exhibited a shorter crack growth process (i.e., breakdown was almost immediate after fracture initiation). These specimens experienced double axial fractures in the upper half of the specimens.
- A relatively long plateau or flat segment in the II curves was developed, especially for g3001 and g3005. These specimens took a little longer time than others to breakdown, resulting in a larger amount of mass.

(a)

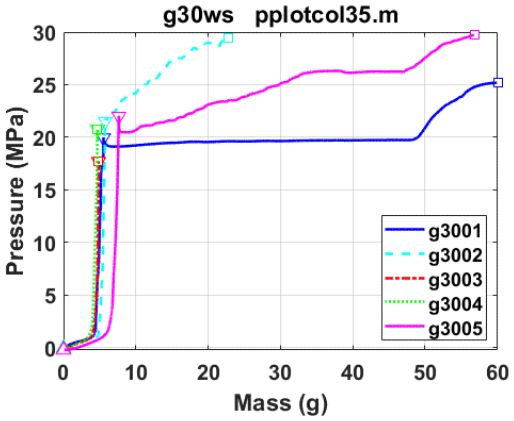

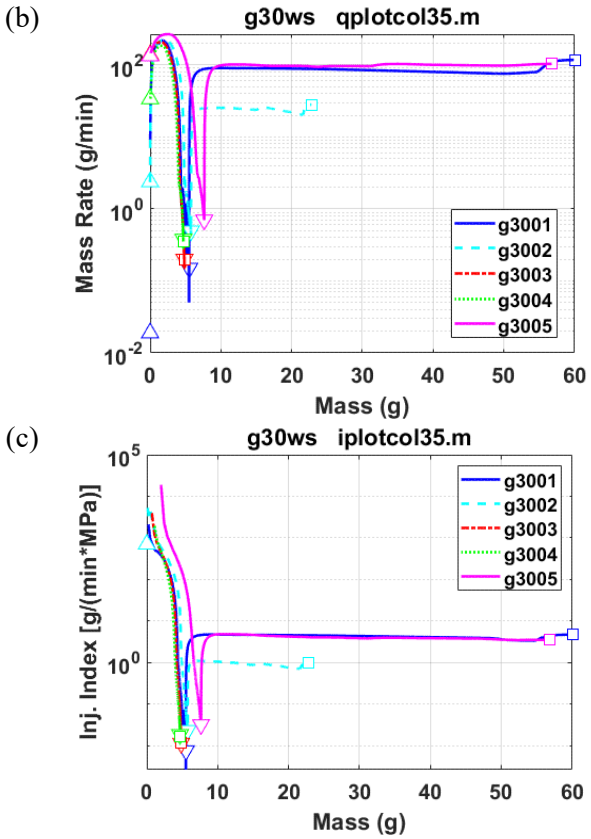

Figure 16 (a) Pressure, (b) mass rate, and (c) injectivity index as a function of mass for G3 series water fracturing under monotonic injection

5.1.3.2 Summary of water fracturing experimental results

The tests were completed with a pressurization rate between 0.14 to 0.52 MPa/s. The rates obtained were either within or close to the range of loading rates as discussed in Section 4.1.1. The rate beyond the fracture initiation generally diminished.

Fracture characteristics

The identification of characteristic quantities can be achieved using sensor data and video data. The fracture initiation can be generally detected by the mass rate changing direction and by extended pressurization. The breakdown can be associated with the momentary mass rate rise and pressure drop. For the uncertainty with the identification like that in small hole size specimens, the video data can assist in clarifying if the breakdown is attained.

Observations of results

The observations based on water fracturing of two series can be summarized below.

1) The pressure response of rock depends more on the total mass rather than the injection time, especially when flow rate varies.
2) There are multiple steps in mass flow rate response that can be related to fracture initiation, coalescence, and breakdown.

3) The breakdown of material may not necessarily result in an immediate pressure drop, especially for the specimens with a small diameter blind hole.
4) Ratio of fracture initiation to breakdown pressures was more than 73%.
5) The fracture initiation and breakdown pressures were affected by the hole size.

Statistics of results of two series

The experimental results are presented in the tables below in terms of mean and standard deviation (Table 5 to Table 7). g25wsm and g35wsm correspond to specimen groups in the G2 and G3 series, respectively. The mass rate and mass had a large standard deviation for both fracture initiation and breakdown and is attributed to the fracture pattern of the specimen.

Table 5 Pressure and mass rate for water fracturing under monotonic injection

grps	mpri	spri	mfli	sfli	mprb	sprb	mflb	sflb
	MPa		g/min		MPa		g/min	
g25wsm	15.205	1.976	1.789	2.660	17.724	2.698	105.134	96.622
g35wsm	20.378	1.692	0.385	0.224	24.568	5.295	49.904	56.645

Note: 1) grps – specimen groups; m*i – mean at fracture initiation; s*i – standard deviation at fracture initiation; m*b – mean at breakdown; s*b – standard deviation at breakdown. 2) *pr* – pressure; *fl* - fluid mass rate. In all the notes, symbol * is a space holder for either a physical or statistic quantity; same comments apply in the following.

Table 6 Injectivity index and injection mass for water fracturing under monotonic injection

grps	miii	siii	mmsi	smsi	miib	siib	mmsb	smsb
	g/(min*MPa)		g		g/(min*MPa)		g	
g25wsm	0.106	0.147	0.818	0.403	6.561	6.257	10.436	5.258
g35wsm	0.018	0.010	0.755	0.390	1.825	2.128	24.924	26.639

Note: *ii* – injectivity index; *ms* – injection mass with filling amount removed.

Table 7 Injection modulus for water fracturing under monotonic injection

grps	mprmk	sprmk
	MPa/g	
g25wsm	27.495	24.487
g35wsm	44.362	30.029

Note: *prm* – injection modulus.

5.2 FOAM FRACTURING

5.2.1 G2 Series

Foam monotonic injection tests were completed for five specimens: g2011 to g2013, g2022 and g2023. All specimens were tested to failure. Specimen g2022 experienced a pilot cycle of pressurization to 3.8 MPa and depressurization before the test to failure. Pressure, mass flow rate and density data were acquired for all tests except g2023 due to a malfunction with the RS233 data acquisition. Videos were taken for all the tests.

The tests mostly were finished between 50 to 68 sec except g2011, which was completed at 133 sec. Breakdown pressures were between 13.4 and 20.1 MPa. Specimen g2011 exhibited a fracture oriented diagonally to the specimen axis while all others exhibited axially and transversely aligned fractures. This subsection provides main experimental results with g2013 as an example and a summary of the results.

5.2.1.1 Pressure, mass rate, density, quality, and gas mass rate ratio (MRR)

Specimen pressurization was nominally linear, but mass flow rate oscillated with transients related to initiation of pressurization, fracture initiation, and breakdown. Pressure variation appears to be correlated with density response.

The foam fracturing responses are shown in Figure 17 and Figure 18 with specimen g2013 as an example. The fracture initiation and breakdown can be identified in a manner similar to the water fracturing experiments. On the pressure curve, these events corresponded to a small drop in pressurization rate at fracture initiation, followed by a peak and rapid pressure drop, at around 46 and 59 sec, respectively. Mass flow rate tended to decline during the pressure ramp up to breakdown with several transient events occurring during fracture initiation and final breakdown. Particularly, a brief drop in mass flow rate was seen right before the breakdown; the mechanism involved is not quite clear.

The injectivity index of the foam continued falling after the initiation of pressurization and went up rapidly upon the breakdown. A small drop in injectivity index took place right before the breakdown due to the mass rate drop as mentioned above. The bottom index was found to be around 0.82 to 1.58 g/(min*MPa).

Density measurements for foam experiments were very sensitive to the mass flow rate. As a result, there was a strong spike at the fracture initiation. Overall, there was a clear increasing trend in density during pressurization, mainly attributed to the increase in gas density; the quality of the foam stayed quite high near 93%.

The water mass rate in the fluid decreased when the gas mass rate increased. This is significant because it showed the replacement of water could be substantial, especially at the high level of pressurization.

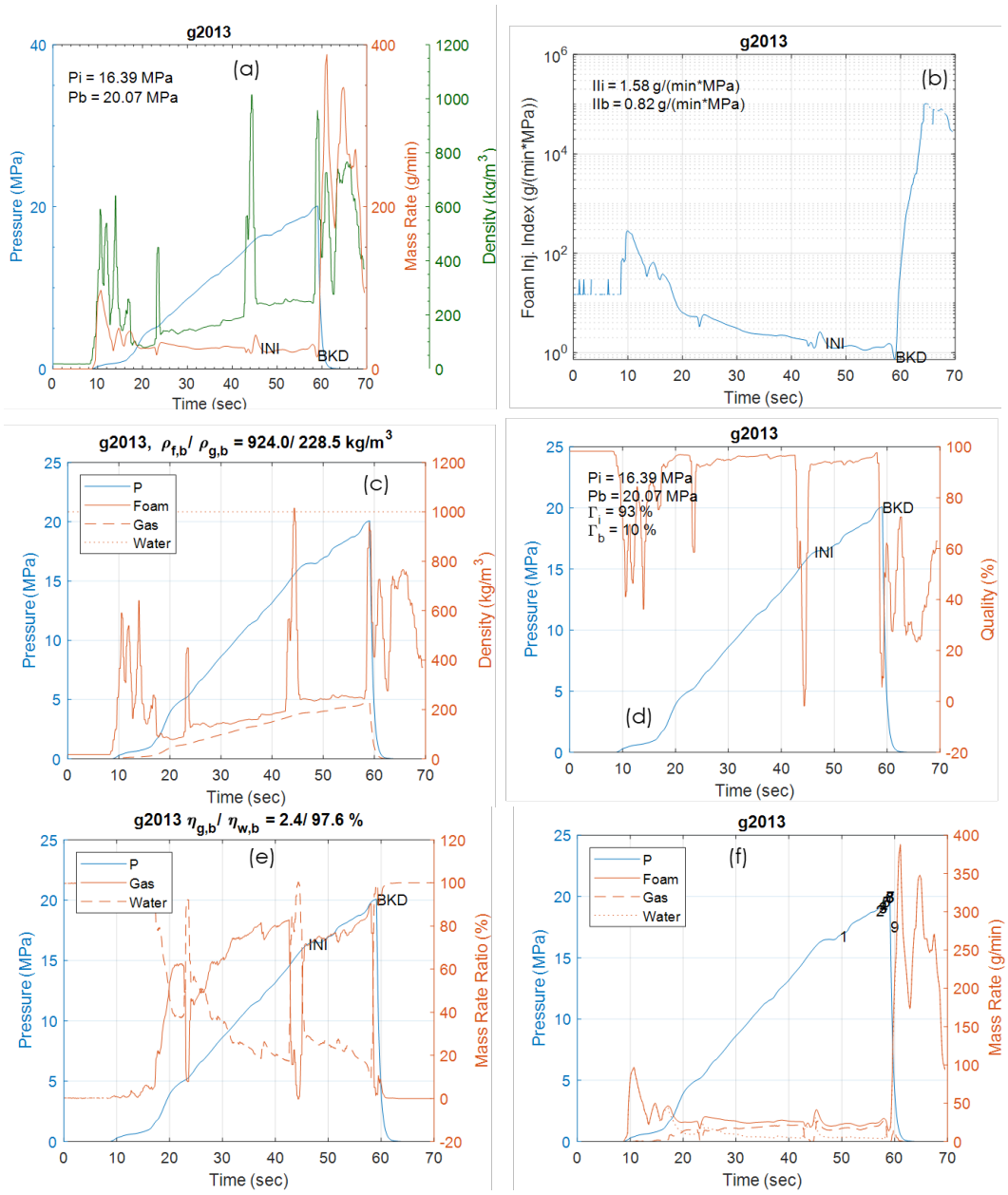

Figure 17 Responses as a function of time for g2013: (a) pressure, mass rate & density, (b) foam injectivity index, (c) density, (d) quality, (e) mass rate ratio, (f) mass rate

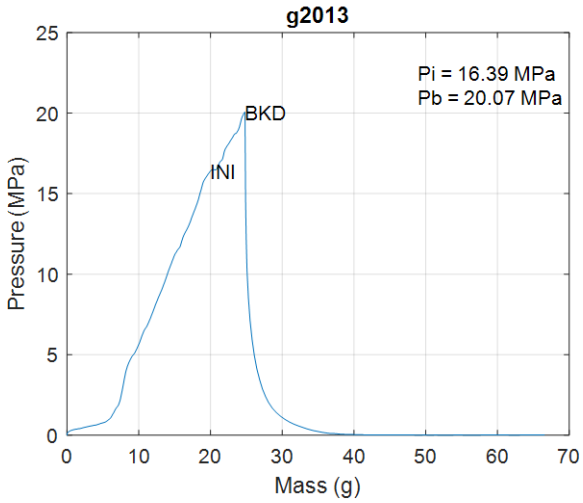

Figure 18 Pressure as a function of mass for g2013.

5.2.1.2 Video and post-test images

Fracture initiation and breakdown can be validated from image captures from the video as demonstrated in Figure 19 for g2013. Figure times correspond to those of Figure 17. Foam fracturing results feature a primary axially aligned fracture with a secondary transverse fracture as signified by the leaking foam on the surface of the specimen.

- #1: figure time 49.55; axial fracture pre-existing and developed ahead of the frame.
  - A local pressure fluctuation was seen at 44.5 sec with local maximum flow, which was identified as fracture initiation.
- #2, 5: figure times 56.51 and 57.66 sec; mist ejected from fracture
- #6: figure time 58.26 sec; broken into small pieces. Simultaneous pressure drop was observed.

(a) 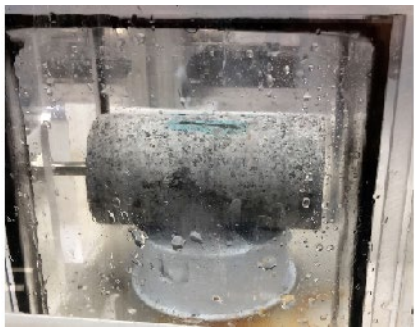

(b) 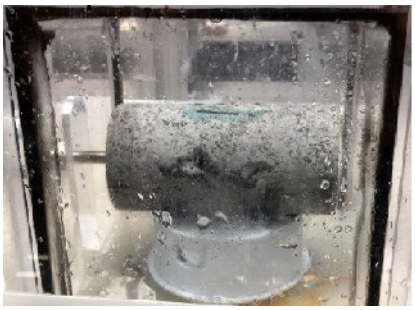

(c) (d)

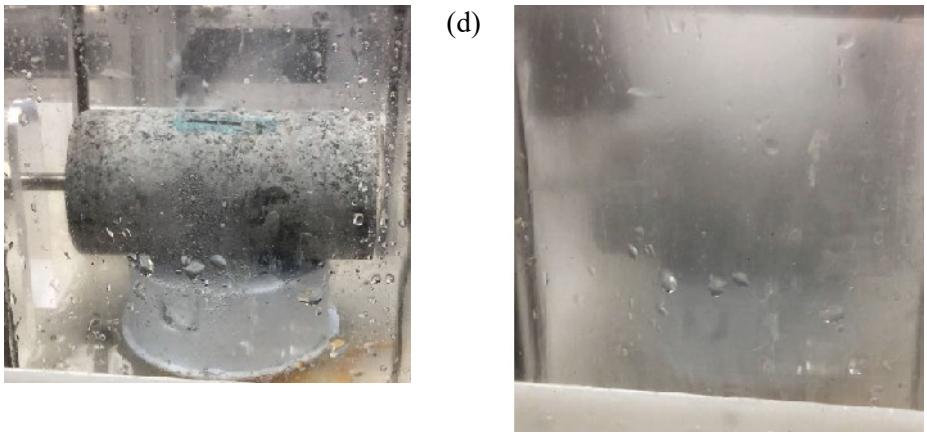

Figure 19 Video-based process for g2013 for events (a) #1: 49.55 s, fracture initiated; (b) #2: 56.51 s mixture ejection; (c) #5: 57.66 s increased ejection; (d) #6: 58.26 s, breakup.

Axially aligned and transversely aligned fracture (highlighted by red dash line) can be seen from the post-test image as shown in Figure 20.

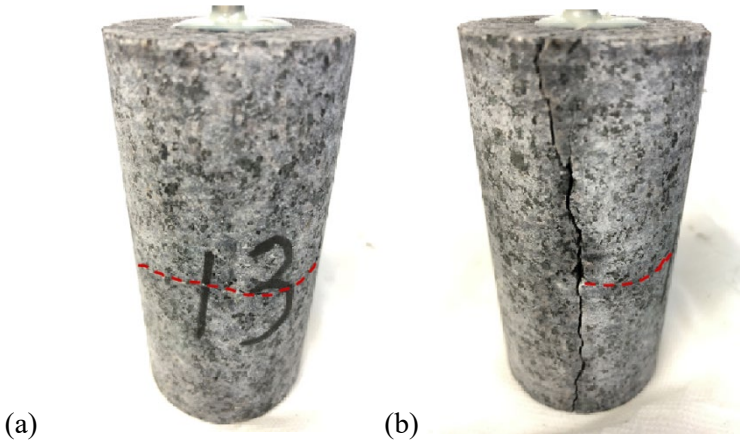

(a) (b)

Figure 20 (a) and (b) Images of tested specimen for g2013 in two orientations, showing a primary axial fracture with secondary transverse fracture. The red dash line illustrates the transverse fracture in one half of the split.

5.2.2 G3 Series

Foam monotonic injection tests were completed for 8 specimens in G3 series: g3006 – g3013. All the specimens were tested to failure. Pressure, mass flow rate and density data were acquired for all the tests except g3012 (the signals acquired by USB were mistakenly not saved for g3012). No online video is available for tests of g3008 and g3013. The densities in tests of g3006 – g3008 were quite high and almost approaching that of water and thus are excluded in the discussion of this series.

The tests mostly were finished between 29 and 52 sec. Breakdown pressures ranged between 15.8 and 23.3 MPa. The failure was observed in a compound mode of axial and transverse aligned fractures.

5.2.2.1 Pressure, mass rate, density, quality, and gas mass rate ratio

The mass flow rate generally responded with a decreasing trend for this set of experiments. Pressure decreased at breakdown, but in contrast to the G2 series of experiments maintained a level just below breakdown for up to approximately 15 seconds. Density continued to increase following breakdown indicating the escape of the gas phase from the specimen.

The fracturing responses of g3011 are given in Figure 21 and Figure 22 as an example. The falling trend of mass rate can be seen easily with fracture initiation and breakdown identified near 36 and 37 sec, respectively. Video footage clearly shows a fracture in the specimen around 37 sec while pressure is maintained at a level slightly below breakdown. The injectivity index minimum is around 0.88 g/(min*MPa) and increases to 7.59 g/(min*MPa) after complete fracture.

The density responded with a fluctuating oscillatory pattern that tended to increase with pressurization. The foam quality at the failure was 93%.

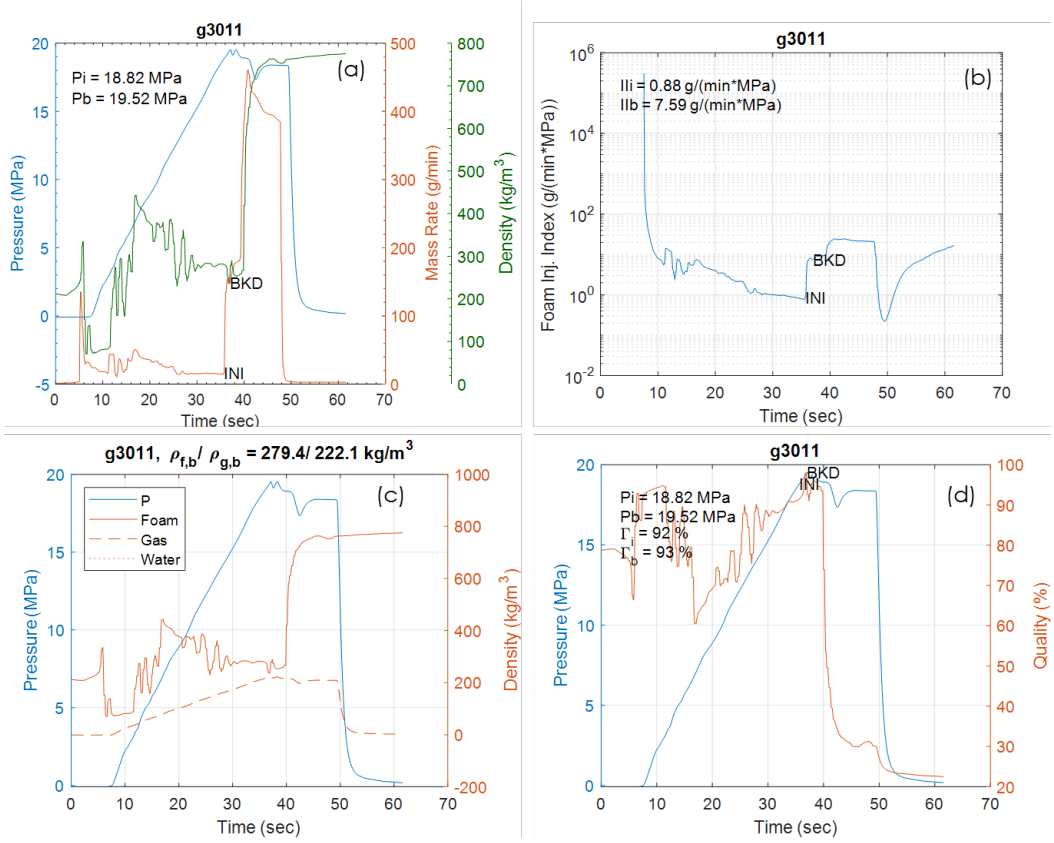

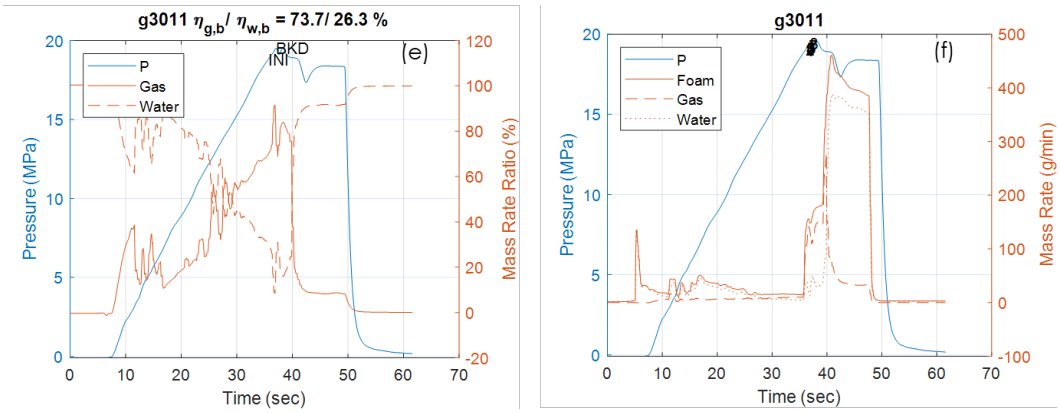

Figure 21 Responses as a function of time for g3011: (a) pressure, mass rate & density, (b) foam injectivity index, (c) density, (d) quality, (e) mass rate ratio, (f) mass rate.

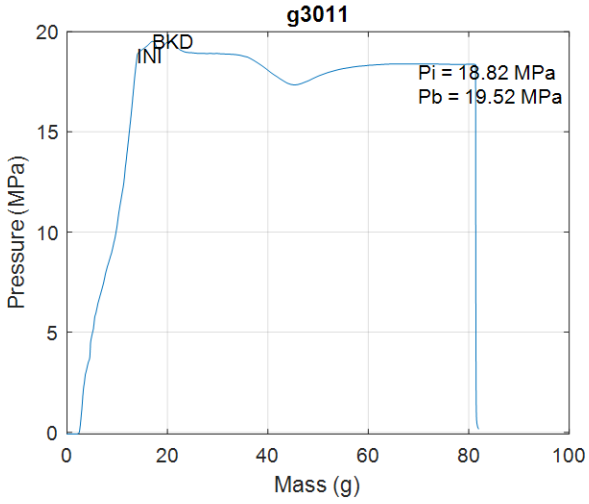

Figure 22 Pressure as a function of mass for g3011.

5.2.2.2 Video and post-test images

Images taken from the footage are shown in Figure 23 with the following characteristic events, where the figure times correspond to Figure 21 (f).

- #3: 36.27 sec, axial fracture with a small angle to the longitudinal axis of specimen emerged
- #6: 36.42 sec, breakup occurred. The upper half of specimen tried to fly up, but was restrained by the connecting tube

Pressure and flow rate data for this specimen indicate that the process from fracture initiation to breakdown took about ¼ sec. There was a delay of the pressure peak with respect to flow rate rise. The axial split and secondary transverse fracture appear to be related to the continued pressurization of the sample following breakdown.

(a) 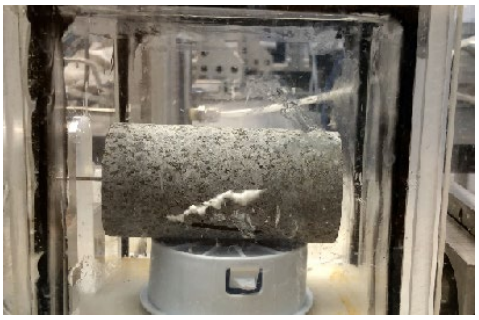 (b) 

Figure 23 Video-based process for g3011 for selected events. (a) #3: 36.27 sec, slant fracture emerged; (b) #6: 36.42 sec, breakup

The primary axial split and secondary transverse fracture can be seen clearly from the post-test image as shown below, Figure 24.

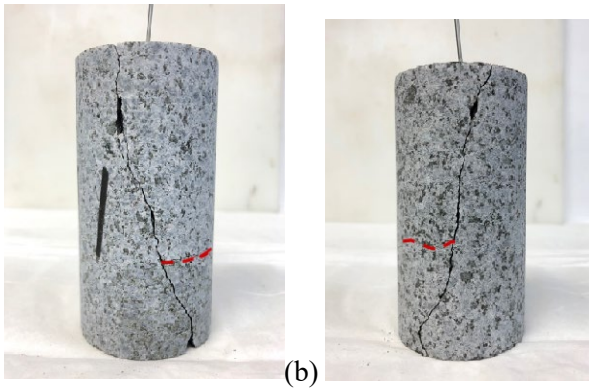
(a) (b)

Figure 24 (a) and (b) Images of tested specimen for g3011 in two different orientations. Red dash line delineates the secondary transverse fracture.

5.2.3 Data Summary

5.2.3.1 Comparison of experimental results by series

G2 series

The responses of the rock for this set of experiments are aggregated in Figure 25 and Figure 26 as a function of total mass injected.

- Generally speaking, pressure curves displayed a linear stage followed by a period with reduced pressurization rate due to fracture initiation, as seen in water fracturing. The initiation and breakdown pressures were generally higher than the water fracturing results, ranging between 12.11 and 17.86 MPa at initiation and 13.36 and 20.07 MPa at breakdown.
- There was an insignificant increase in mass flow rates between fracture initiation and breakdown. However, it was generally higher than water fracturing at fracture initiation but lower at breakdown.
- The II curves of foam exhibited a gradual, rather than sharp, drop compared to water experiments. This is expected given the compressibility of the foam and comparatively smaller rise in pressure

that would be associated with continued injection of mass into the blind hole of the specimen after initial fill. Continued water injection after initial filling, by comparison, rapidly increases pressure in the specimen due to its incompressibility with a resultant reduction in II. The II at the fracture initiation was seen to range between 0.59 and 1.64 g/(min*MPa) and enhanced to 0.75 – 2.54 g/(min*MPs) prior to breakdown. The initiation II level was apparently higher than in water fracturing, whilst the breakdown II was lower.

- The quality generally stayed at a high level above 90% with small fluctuation for individual test.
- The mass rate ratio for gas exhibited a steady increase with accumulated mass, around 80% near breakdown, because of increased replacement of water.

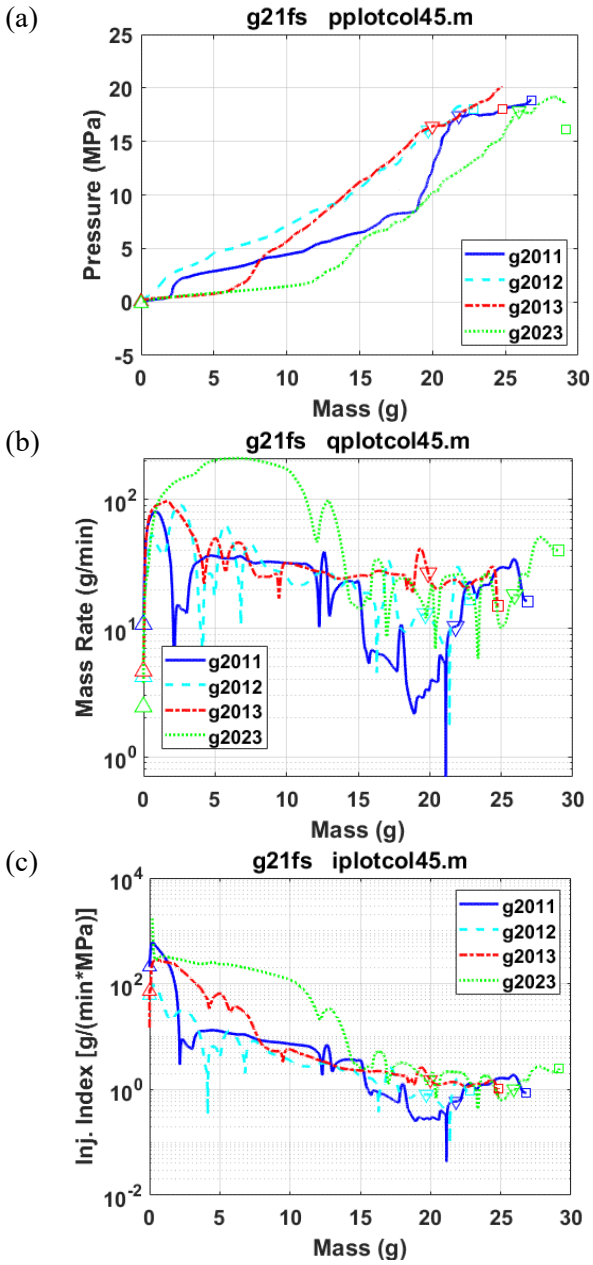

Figure 25 (a) Pressure, (b) mass rate and (c) injectivity index as a function of mass for G2 series foam fracturing under monotonic injection

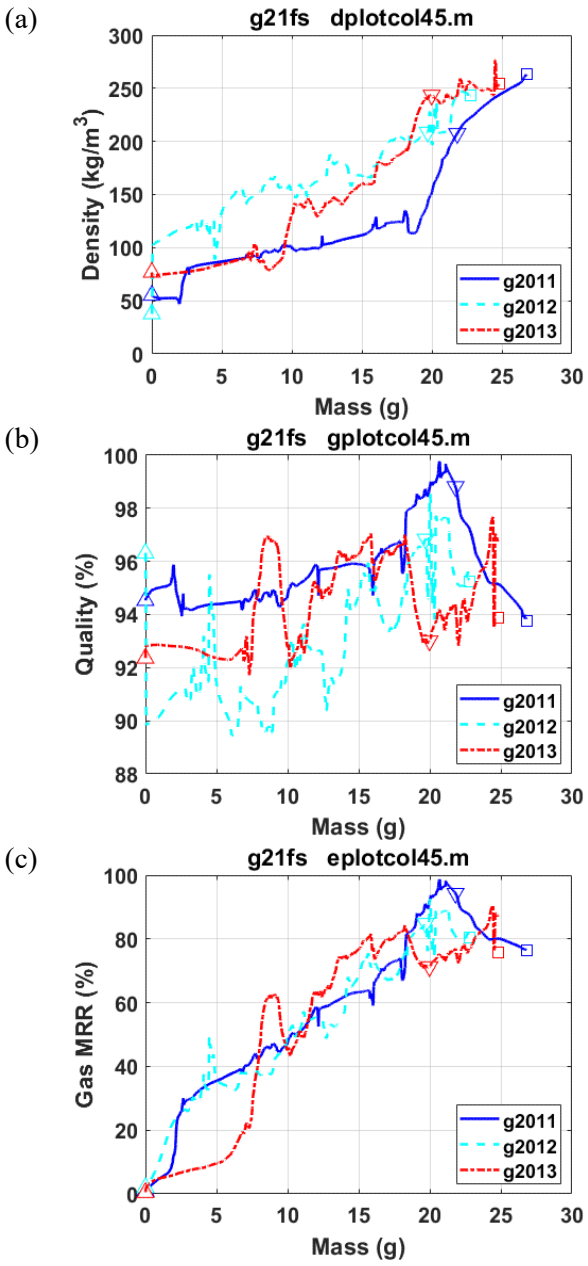

Figure 26 (a) Density, (b) quality and (c) gas mass rate ratio as a function of mass for G2 series foam fracturing under monotonic injection; transient pulses/ pikes in density were removed.

G3 series

Plots for G3 series are aggregated in Figure 27 and Figure 28:

- The initiation and breakdown pressures in G3 series were both higher than for G2 series, ranging between 14.7 and 22.9 MPa at initiation and 15.8 and 23.3 MPa at breakdown.
- The increase in mass flow rate between fracture imitation and breakdown was larger than in G2 series.

- II curves were similar to foam experiments for G2 series; the level of II at fracture initiation was located between 0.30 and 1.19 g/(min*MPa), and higher than G2 series at breakdown ranging between 4.46 and 9.18 g/(min*MPa).
- The quality was generally obtained at a high level of about 90% with small fluctuation, even though it varied between specimens.
- The mass rate ratio for the gas exhibited a steady increase with accumulated mass, around or higher than 80% near fracture initiation and break, because of increased replacement of water.

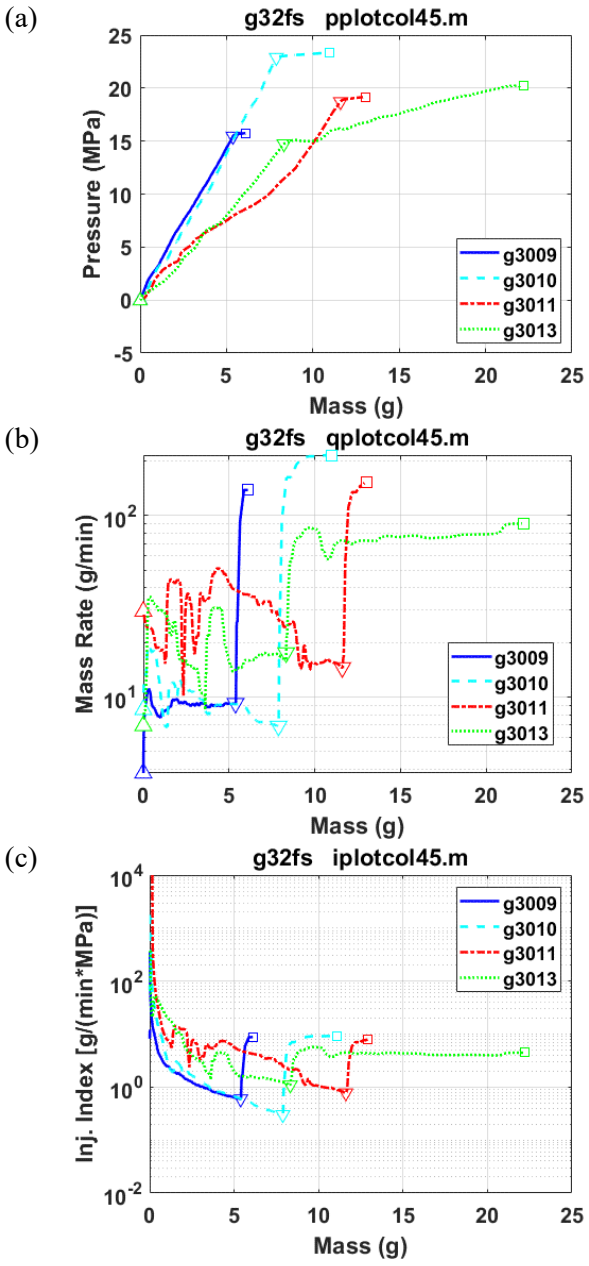

Figure 27 (a) Pressure, (b) mass rate and (c) injectivity index as a function of mass for G3 series foam fracturing under monotonic injection

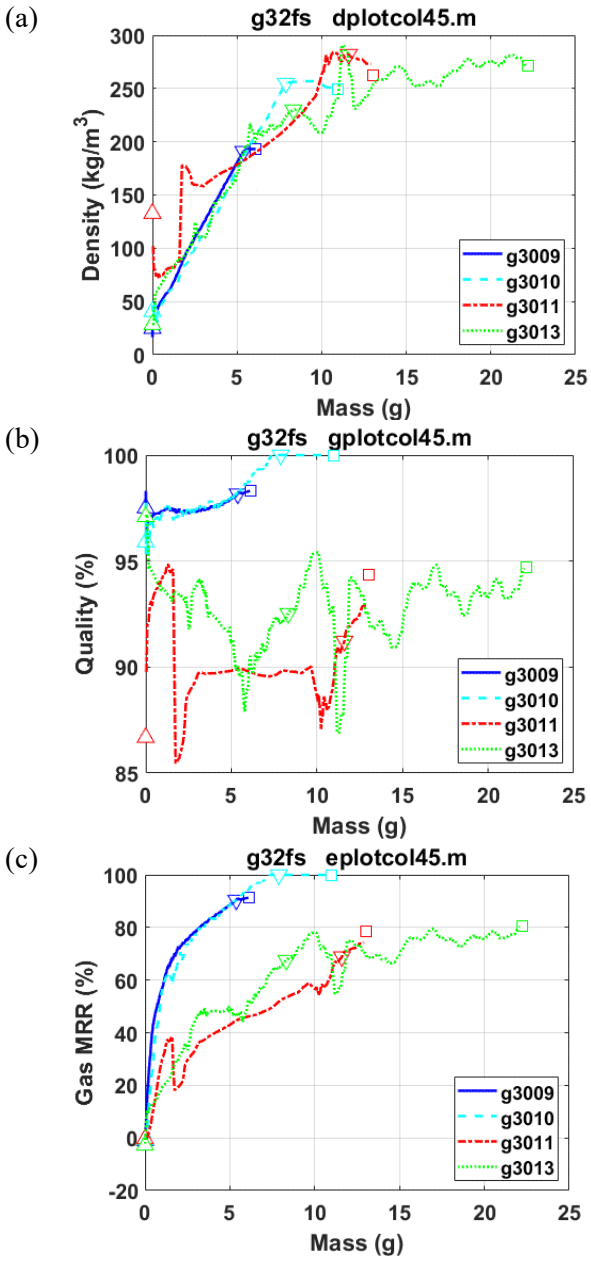

Figure 28 (a) Density, (b) quality and (c) gas mass rate ratio as a function of mass for G3 series foam fracturing under monotonic injection; transient pulses/ pikes in density were removed.

5.2.3.2 Summary of foam fracturing experimental results

The pressurization rates before fracture initiation ranged between 0.147 and 0.664 MPa/s. These rates are close to those discussed in Section 4.1.1. The rates after fracture initiation were generally lower with a range between 0.100 and 0.494 MPa/s.

Fracture characteristics

Fracture initiation can be detected by 1) a sudden increase in mass flow rate, 2) local fluctuation of density, and 3) sustaining pressurization. The breakdown can be associated with the momentary mass flow rate rise and pressure drop. As previously discussed, video data of experiments was useful for identifying the specific point in time that breakdown occurred when it was less obvious in pressure and mass flow rate data.

Experimental results

1) In the time domain, breakdown occurs close to the fracture initiation in foam fracturing, especially for those tests with high quality foam. This is likely due to stored energy in the foam, due to its compressibility, contributing to fracture propagation. For comparison purposes, water fracturing requires continued injection of fluid to provide energy to drive fracture propagation.
2) As in water fracturing, the fracturing initiation and breakdown pressures can be easily identified in the pressure vs. mass curve.
3) Unlike water fracturing, no steep rise was seen in mass flow rate following a fracture initiation.
4) Density tends to increase with the increasing pressure, whilst quality doesn't show any appreciable variation trend.
5) The breakdown pressure for foam fracturing was slightly higher than for water fracturing.
6) The fracture initiation and breakdown pressures obtained for a specimen with a small diameter blind hole were higher than those for large diameter blind hole specimens. This is expected based on the higher hoop stress level associated with the smaller borehole.
7) The degree of breakage completion depended on the foam quality with a higher quality (drier) foam more likely to break the specimen into small pieces. This is also expected based on the energy released by the expansion of the gas phase of the foam.

Statistics of results of two series

A summary is provided in the tables below (Table 8 to Table 13). g26fsn, and g35fsn are specimen groups of G2 and G3 series, respectively. The mass flow rate and mass had a quite large standard deviation at both fracture initiation and breakdown. Such large variation should be related to the fracture pattern or failure mode developed.

Table 8 Pressure and mass rate for foam fracturing under monotonic injection

grps	mpri	spri	mfli	sfli	mprb	sprb	mflb	sflb
	MPa		g/min		MPa		g/min	
g26fsn	15.960	2.273	15.798	6.966	17.790	2.583	24.377	11.660
g35fsn	17.945	3.719	12.037	4.838	19.628	3.132	148.877	51.085

Note: 1) grps - specimen groups; m*i – mean at fracture initiation; s*i – standard deviation at fracture initiation; m*b – mean at breakdown; s*b – standard deviation at breakdown. 2) *pr* – pressure; *fl* - fluid mass rate.

Table 9 Injectivity index and injection mass for foam fracturing under monotonic injection

grps	miii	siii	mmsi	smsi	miib	siib	mmsb	smsb
	g/(min*MPa)		g		g/(min*MPa)		g	
g26fsn	0.988	0.398	11.841	3.910	1.444	0.831	15.555	3.678
g35fsn	0.716	0.371	7.462	1.345	7.596	2.152	12.243	6.685

Note: *ii* – injectivity index; *ms* – injection mass with filling amount removed

Table 10 Injection modulus for foam fracturing under monotonic injection

grps	mprmk	sprmk
	g/MPa	
g26fsn	1.546	0.843
g35fsn	2.437	0.489

Note: *prm* – injection modulus

Table 11 Foam density and quality for foam fracturing under monotonic injection

grps	mdni	sdni	mqli	sqli	mdnb	sdnb	mqlb	sqlb
	Kg/m^3		%		Kg/m^3		%	
g26fsn	209.485	23.040	95.985	2.136	240.614	22.895	94.951	1.199
g35fsn	239.462	38.715	95.479	4.262	243.939	35.098	96.841	2.766

Note: *dn* – density; *ql* – foam quality

Table 12 Mass rate and mass of water in fluid for foam fracturing under monotonic injection

grps	mrwi	srwi	mmwi	smwi	mrwb	srwb	mmwb	smwb
	g/min		g		g/min		g	
g26fsn	3.276	2.704	4.381	2.008	4.760	3.109	5.174	1.985
g35fsn	2.772	2.756	3.004	1.534	15.541	13.462	4.048	3.052

Note: *rw* – mass rate of water in fluid; *mw* – mass of water in fluid with filling amount removed

Table 13 Gas mass rate ration for foam fracturing under monotonic injection

grps	mgmrri	mgmrrb
	%	%
g26fsn	83.410	84.378
g35fsn	76.975	89.561

Note: *gmrr* – gas mass rate ratio

5.3 COMPARISON OF WATER AND FOAM FRACTURING FOR MONOTONIC INJECTION

Comparison plots of water and foam response are shown in Figure 29 and Figure 30. It has been observed that there was a fair amount of fracture propagation after fracture initiation in our tests with both water and foam. The fracture propagated in both radial and axial directions and the pressure was increased during the process so that the fracture propagation was stable. The breakdown occurred when the propagation became unstable, which usually followed with an overshoot in mass flow rate and fluid ejection. The same phenomenon has been observed in hydraulic fracturing with pressurization rate control by Zoback et. al. (1977), investigated by Detournay and Carbonell (1997), and recently by Chen et al. (2022). A summary of observations highlighting the differences between water and foam fracture initiation and breakdown for monotonic injection is provided below.

5.3.1 Fracture Initiation Characteristics

- As expected, based on the calculated maximum stress levels for an internally pressurized borehole, there was a hole-size effect on fracture initiation pressure, but the initiation pressure was more variable in the case of foam and could be either higher or lower than nominally expected. This variability could be related to the high penetrability of gas in the foam and activation of smaller fractures within the specimen. Meanwhile, the pressure at fracture initiation of foam was higher than of water as expected because of different viscosities. But the difference appeared to be not significant.
- In general, the mass flow rate for foam was significantly higher for a given hole size. This is presumably due to a combination of serval factors, including higher fracture initiation pressure (higher pressure drives a larger flow rate), the creation of a larger fracture opening than for water fracturing experiments, and gas compressibility within foam. The mass flow rate was generally lower for specimens with smaller diameter boreholes.
- Accordingly, injection modulus showed a significant decrease in foam fracturing and a higher value for specimens with smaller borehole diameters.

5.3.2 Breakdown Characteristics

- The pressure increase from initiation to breakdown is apparently less in foam than in water for both sizes of blind hole. This is mainly attributed to the short period of subcritical crack growth (SCG); the head loss in fracture flow initiated in foam fracturing might be different from water fracturing and contributed to the difference in pressure increase observed.
- Owing to the short SCG period, the increases in mass flow rate, II, and mass from fracturing initiation to breakdown of foam fracturing were obviously less than those of water fracturing. Further analyses are given in Sects. 7.3 and 7.4 with special attention paid on the water amount contained within a foamed fluid.

5.3.3 Fracture Surface Characteristics

- The breakage generated by water was generally partial, and fractured rock specimen still maintained its geometrical shape with sizable bridges. On the other hand, the foam produced a more complete fracture that broke the specimen into multiple pieces. Based on fracture surface reconstructed using the surface trace coordinates of fractures, it was estimated the fracture area by foam is at least 24 to 39% larger than that by water. More data related to fracture surface morphology are being collected.

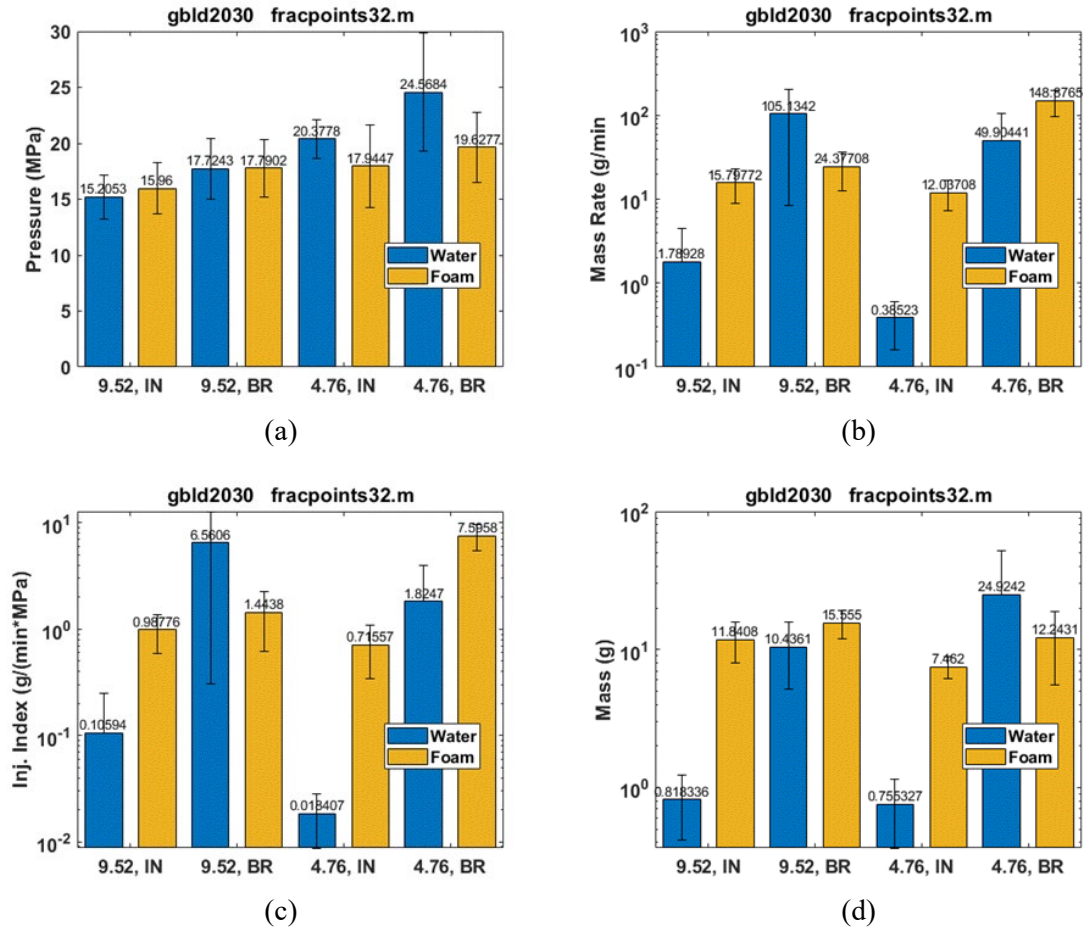

Figure 29 Bar graphs for (a) pressure, (b) mass rate, (c) injectivity index, and (d) mass. All the error bars have a half of standard deviation. IN – fracture initiation; BR – breakdown. 9.52 – G2 series hole diameter in mm; 4.76 – G3 series hole diameter in mm.

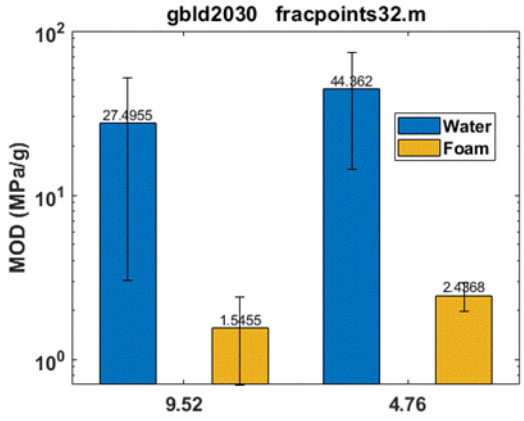

Figure 30 Bar graph for injection modulus. All the error bars have a half of standard deviation. 9.52 – G2 series hole diameter in mm; 4.76 – G3 series hole diameter in mm.

6. RESULTS OF CYCLIC INJECTION

6.1 WATER FRACTURING

6.1.1 G2 Series

Cyclic water injection tests were completed for 5 specimens in the G2 series: g2006 – g2010. The maximum pressures in the test ranged from 11.3 to 13.7 MPa with the minimum pressures around zero. The maximum pressures are 64 to 77% of the breakdown pressure under monotonic injection. The cycling started either with the amplitude ramped to a target level, g2006, or after the pressure was driven monotonically to target levels like in g2007- g2010. All the sensor data are available; the video is only available for g2009.

The number of cycles to failure was ranged from 4 to 78. Specimens were not broken into smaller pieces by the produced fractures. Bimodal failures occurred with an axial fracture and a transversely aligned fracture that spanned approximately half of the cross section. One post-test specimen didn't show any visible fracture on the surface.

6.1.1.1 Timed data and peaks/ valleys

While the peak pressure was mostly maintained at a constant level during the cycling, mass rate varied along with the alternation of fracturing and saturating during the process.

The responses of granite with g2009 as an example are shown in Figure 31 and Figure 32. The peak pressure was about 68% of the monotonic breakdown pressure. The number of cycles to failure was 78. While the peak pressure for this specimen stayed around 12 MPa throughout the cycling, the mass rate appeared with four rise-and-fall events near 15, 150, 200, and 300 sec.

The II ranged from 0.3 to 30 g/(min*MPa), which had a range similar to the II of the monotonic injection. This corresponds to fill and discharge of the flow line and borehole and indicates that the material condition of specimen used in cyclic injection was same as that in monotonic injection.

It was observed that the pressure peak was not synchronized with mass flow rate and had a typical delay of less than 2 sec. In other words, the mass flow rate increased faster, reached its peak earlier, and decreased while the pressure continued to rise. The pressurization after the mass rate peak would be more related to the interaction of fluid and rock. This can be seen from mid-life curves in Figure 32. The II decreased while the pressure continued increasing after the mass flow rate peaked at point A. The declination of II from A to B reflects a process of pressurization imposed on the specimen. This is what was observed in the monotonic injection; namely, the specimen was increasingly saturated before fracture initiation while the II was decreasing. The pressure peak delay shall be related to the factors such as upfront pressure system components and the material condition including blind hole, new fracture, and permeability of the rock. The rapid mass rate rise and pressure build-up reflected the characteristics of these factors. When the pressure system is unchanged, any change in pressure/ flowrate peak and peak offset is possibly indicative of alteration of the material due to fatigue.

Another noted observation of the experimental data shows that while the pressure profile remains nominally the same with subsequent cycles, the mass flow rate exhibited a tendency to reach higher value with each new cycle. This trend is also captured in the II plots in the same figure.

The deformed shape of flow rate peak was seen on the failure cycles of other specimens. The size of pressure peak was also seen to be diminished in failure cycles.

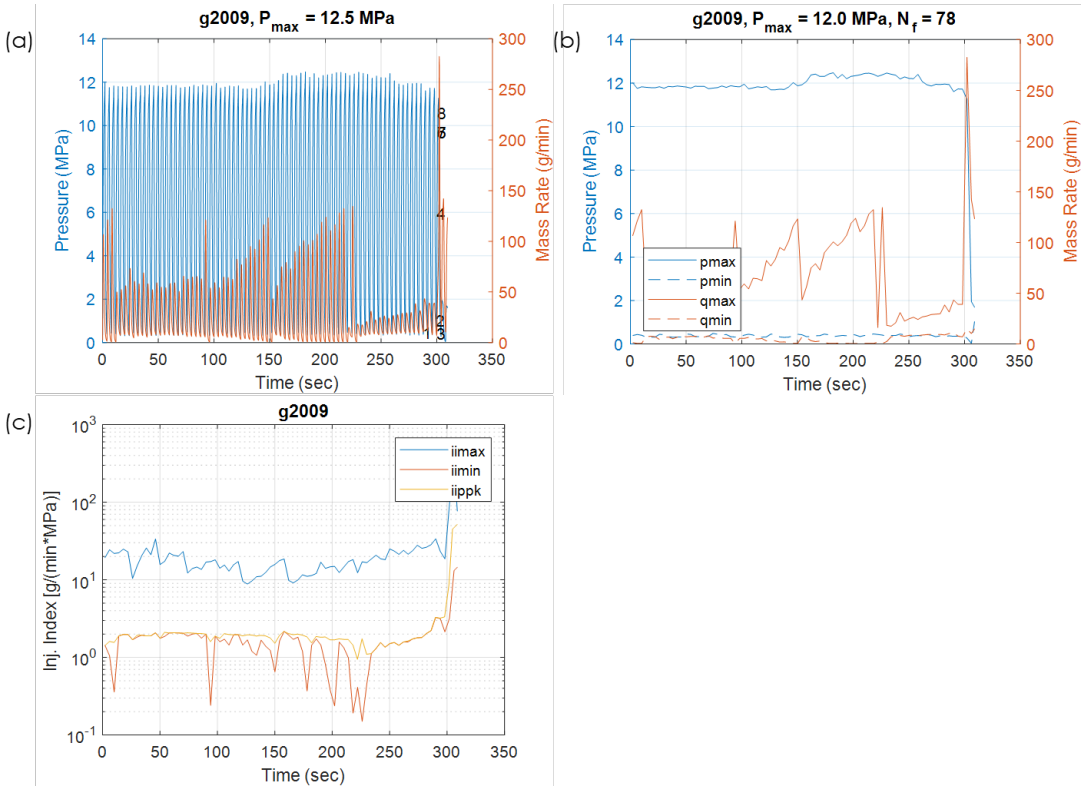

Figure 31 Cyclic injection responses as a function of time for g2009: (a) waveforms of pressure and mass rate, and (b) extreme values of pressure and mass rate, and (c) injectivity index; water as fracturing fluid.

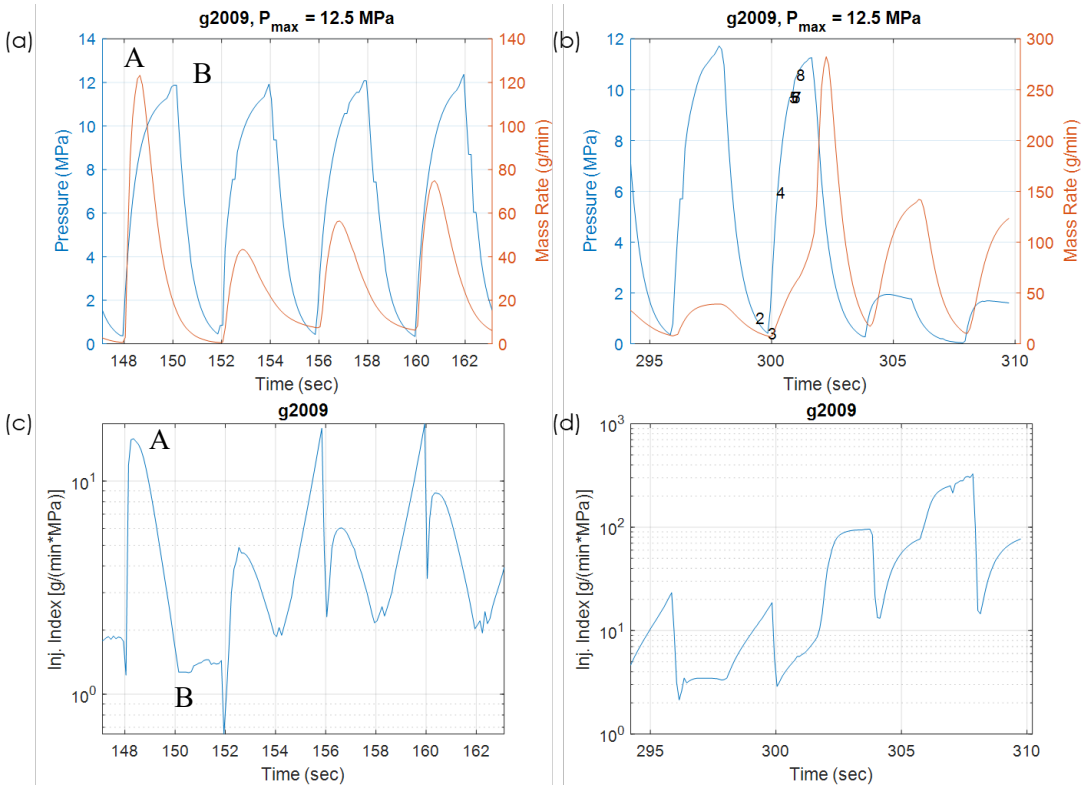

Figure 32 Cyclic injection responses as a function time for g2009: pressure and mass rate during (a) middle life and (b) failure cycle, and instantaneous injectivity index during (c) middle life and (d) failure cycle; water as fracturing fluid. Numbers correspond to the events in the footage taken by video camera.

6.1.1.2 Video data and post-test images

The following observations are made for the images shown in Figure 33, where the figure times correspond to those event numbers marked in Figure 31 and Figure 32.

- #1: 287.69 sec, a small amount of water is seen exiting the specimen indicating fracture to the outer surface of the specimen
- #2: 299.36 sec, a significantly larger volume of water is seen exiting the specimen
- #5, 6: 300.73, 300.82 sec, a complete penetration of the fracture through the specimen outer surface is seen along with a large pressure drop indicative of the flow system unable to maintain pressurization of the specimen

The post-test of specimen is shown in Figure 34 indicating the axial fracture near the top. The summary of the distribution of failure patterns including those induced by cyclic and monotonic injections is provided in Section 7.1.

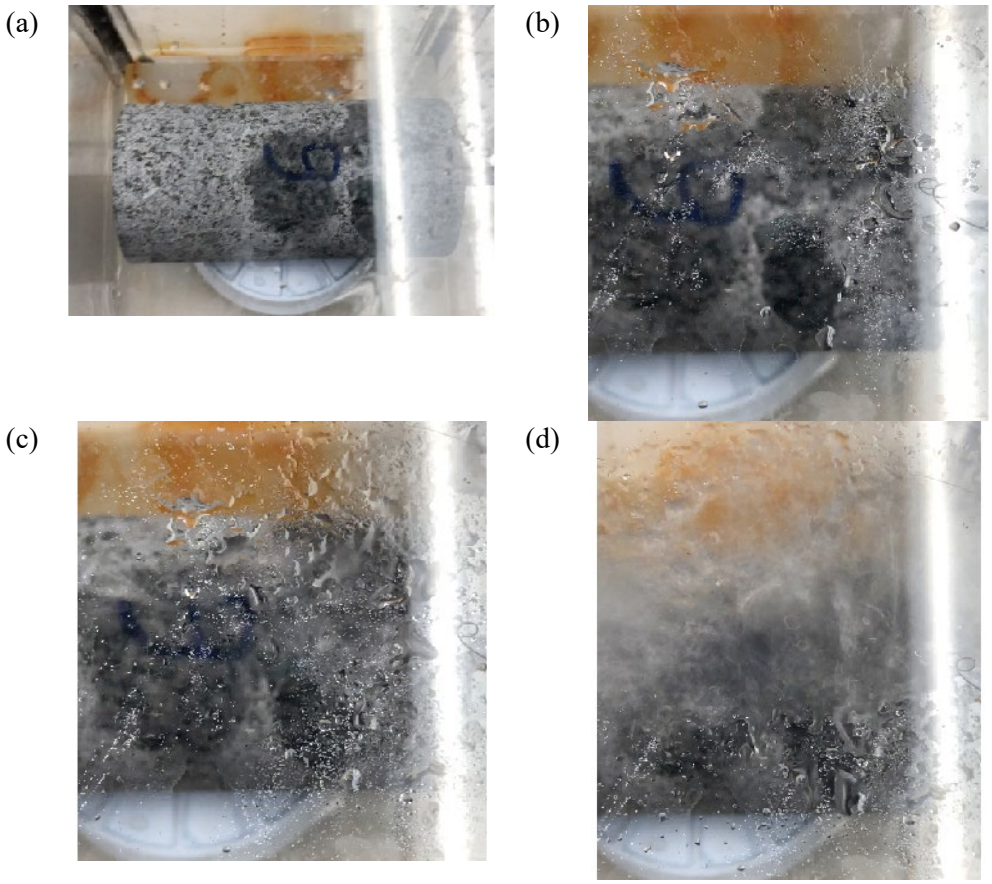

Figure 33 Images based on the footage of g2009 where the injection tube is on the right side. (a) #1: 287.69 sec, water leaked in the center upper half; apparently, fracture initiated ahead of the image; (b) #2: 299.36 sec, water eruption was seen; (c-d) #5, 6: 300.73, 300.82 sec, water eruption increased substantially with splash as a sign of breakdown

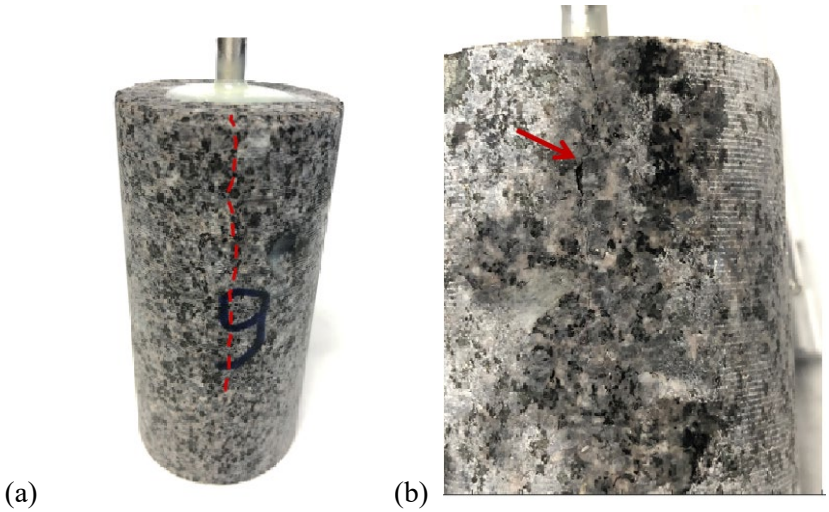

Figure 34 Images of tested specimen for g2009; (b) is the enlarged top part opposite of (a) showing longitudinal fracture.

6.1.2 Data Summary

6.1.2.1 Fatigue curves

The fatigue fracturing responses under water cyclic injection are summarized and presented in Figure 35 in terms of maxima of pressure, pmax, and mass rate, qmax, and pressure peak-based injectivity index, IIppk.

There is not a clear relationship evident in the data between the fatigue life and maximum pressure. The increase in injectivity index per cycle appeared is highest for the specimen with the shortest fatigue life. Higher initial injectivity indices could be related to pre-existing fractures in the specimen and induced damages during cycling.

(a)

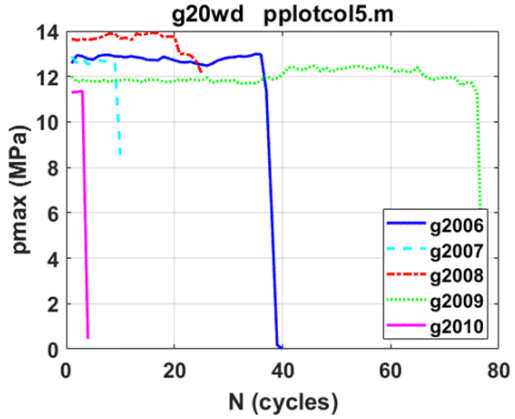

(b)

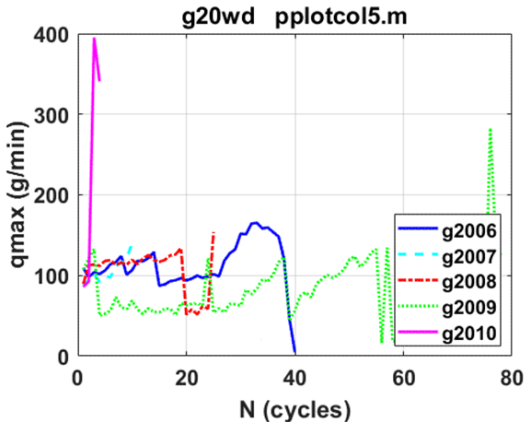

(c)

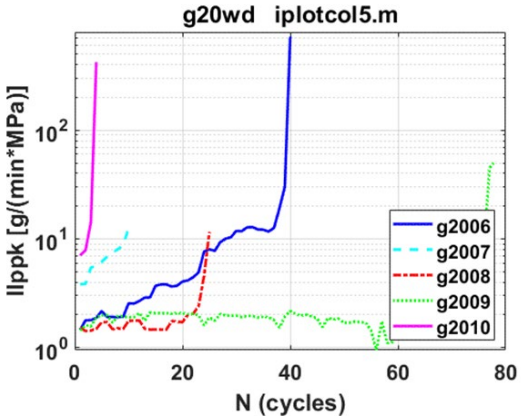

Figure 35 Fatigue responses as a function of number of cycles for G2 series: (a) maximum pressure, (b) maximum mass rate, and (c) pressure peak-based injectivity index

6.1.2.2 Summary of cyclic water fracturing experimental results

Cycling and fracturing mechanism

The pressurizing half cycle provides high speed impact and serves as the primary damage mechanism. The depressurizing creates a tensile release stress wave within the stressed body that can be a secondary damage mechanism. The depressurizing half cycle also lowers downstream pressure and creates a returning flow to remove debris. Such repeated pressurization-depressurization actions can result in more control fracturing than a conventional fracturing process.

With a 4-sec pulse period, the blind hole granite specimen can be fractured with a specified pressure amplitude. Cyclic fracturing can be accomplished with reasonable cycles when the fracture is initiated by a cyclic ramping or monotonic pressurization process. Subsequent cycling serves as a driving force for sub-critical crack growth or re-fracturing.

Statistics of results

The cyclic test results are summarized in Table 14, where the lifetime of rock under cyclic injection is described in terms of maximum or peak pressure to monotonic breakdown pressure. Generally, the fracturing can be achieved by using a ratio of 0.64 to 0.77, and the lifetime ranged between 4 and 78. In such range of variation, no relation between lifetime and pressure amplitude was seen.

Table 14 Cyclic results with water as fracturing fluid

grps	sps	p_{max}	N_f	p_b	p_{max}/p_b
		MPa	Cycles	MPa	
g21wd	g2006	12.60	38	17.70	0.71
	g2007	12.70	9	17.70	0.72
	g2008	13.70	25	17.70	0.77
	g2009	12.00	78	17.70	0.68
	g2010	11.30	4	17.70	0.64

NOTE: sps – specimens; p_{max} – maximum pressure; N_f – number of cycles to failure; p_b – monotonic breakdown pressure

6.2 FOAM FRACTURING

6.2.1 G2 Series

Foam cyclic injection tests were completed for 5 specimens in the G2 series: g2014 – g2018. The maximum pressures in the tests ranged from 10.4 to 13.3 MPa with the minimum pressures around zero. The maximum pressures were 58 to 75% of the breakdown pressure measured for monotonic injection. The cycling started with the amplitude ramped to the target level in g2014, g2016 and g2017. A low amplitude pre-fatigue cycling was carried out in two specimens: 6.5 MPa peak pressure with 350 cycles

for g2015, and 11.5 MPa peak pressure with 163 cycles for 2018. No visible change in injectivity index was seen in the pre-fatigue cycling indicating no fatigue response in the materials at this pressure level. Sensor data was recorded for all of the tested specimens, but the online video was unavailable for g2015 and g2018.

The number of cycles to failure ranged from 7 to 225. The specimens were split into two pieces (g2017) or experienced axially-aligned fractures with secondary transversely-aligned fractures developed in half of the cross section (g2014- g2016, g2018).

6.2.1.1 Timed data and peaks/ valleys

Fatigue responses of g2015 are presented in Figure 36 and Figure 37. The peak pressure for this specimen was nominally constant during the cycling, 12.8 MPa, about 72% of breakdown pressure under monotonic injection. Number of cycles to failure is 34.

The peak mass flow rate fluctuated slightly around the level of 300 g/min. At approximately 133 seconds, the mass flow rate profile changes direction (i.e., transitions from declining to increasing) without an accompanying increase in pressure indicating fracture of the rock. This abrupt change is also reflected in the injectivity index plot, and this behavior is consistent with the behavior of other tested specimens.

Density varied substantially over the course of each test on the order of approximately ± 45% (see the figure title) but was not correlated to pressure cycling. This variation was likely due to foam generation system challenges related to producing foam with consistent quality while simultaneously cycling specimen pressure. The pressure peak-based density had an averaged value of 588 kg/m^3. The foam quality was 48%, and max mass rate ratio of gas was 28% overall.

(a)

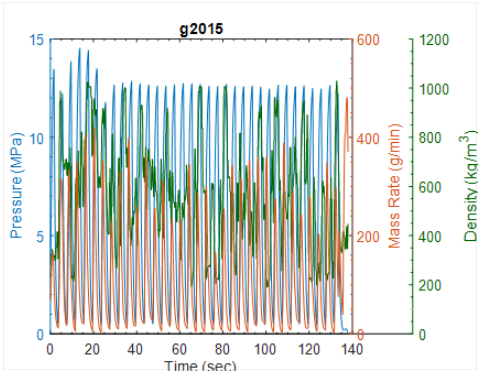

(b)

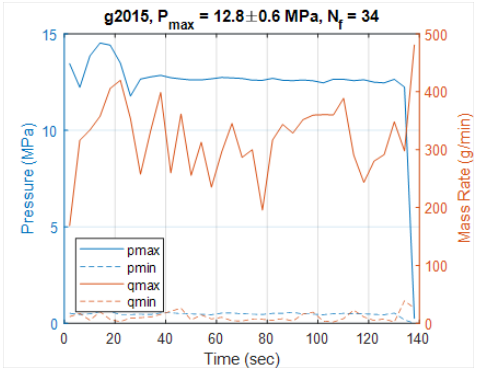

(c)

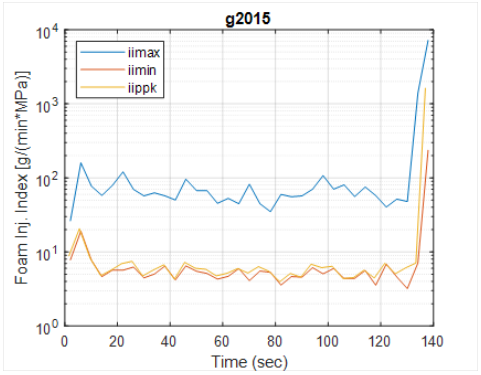

(d)

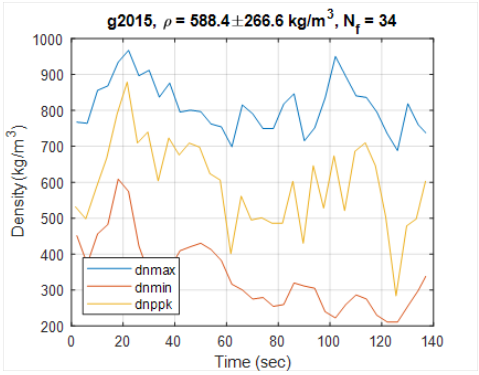

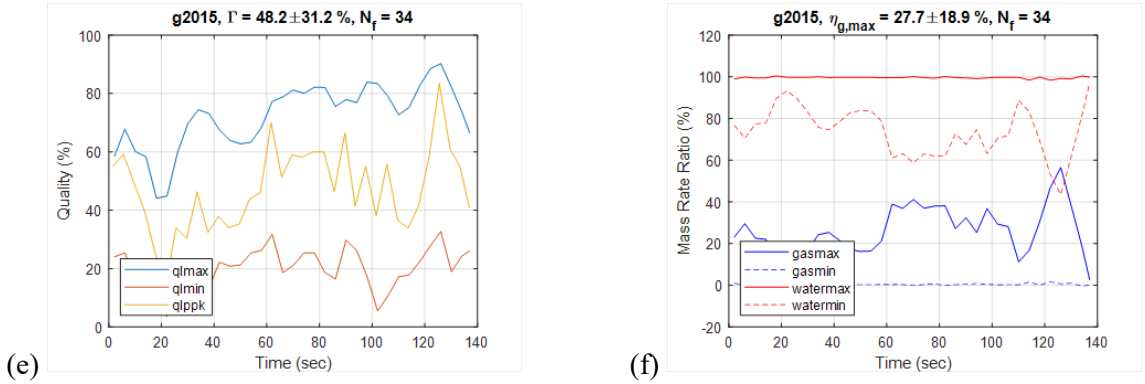

Figure 36 Cyclic injection responses as a function of time for g2015 with foam as a fracturing fluid: (a) timed data for pressure, mass rate and density, (b-f) extremes for pressure and mass rate, injectivity index, density, quality, and mass rate ratios. N_f in title is a nominal number based on figure time and cycle period.

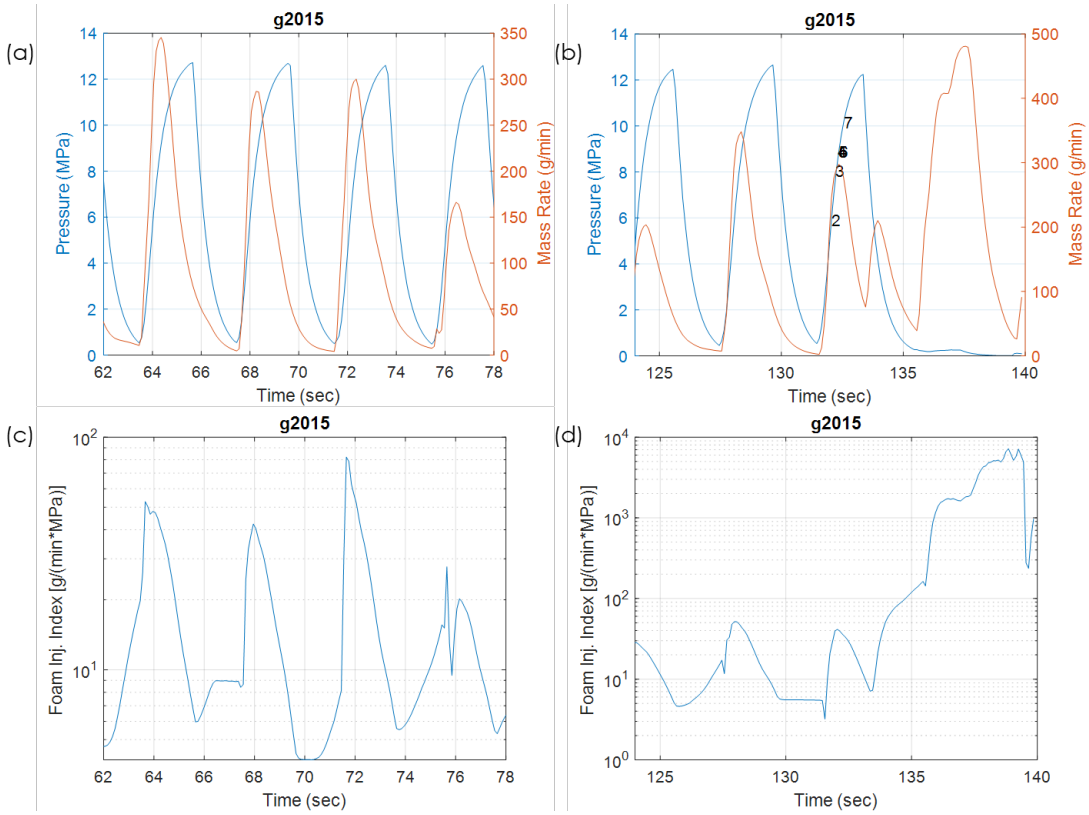

Figure 37 Cyclic injection responses as a function of time for g2015 with foam as a fracturing fluid: pressure and mass rate in (a) middle life and (b) final cycles, and instantaneous injectivity index in (c) middle life and (d) final cycles.

6.2.1.2 Video and post-test images

The following observations are made for the images shown in Figure 38, where figure times correspond to those marked by the number in Figure 37. The following events are notable:

- #1: figure time, 28.90 sec, pre-existing fracture in center half of specimen, water leak synchronized with open of PV1
- #4, 5, 6: figure time, 132.31- 132.40 sec, water leak extended from PV1 open to PV1 close in previous cycle in video, and break up occurred in the following cycle as marked above

The images of the post-test specimen in Figure 39 illustrate the axial split and secondary transverse fracture.

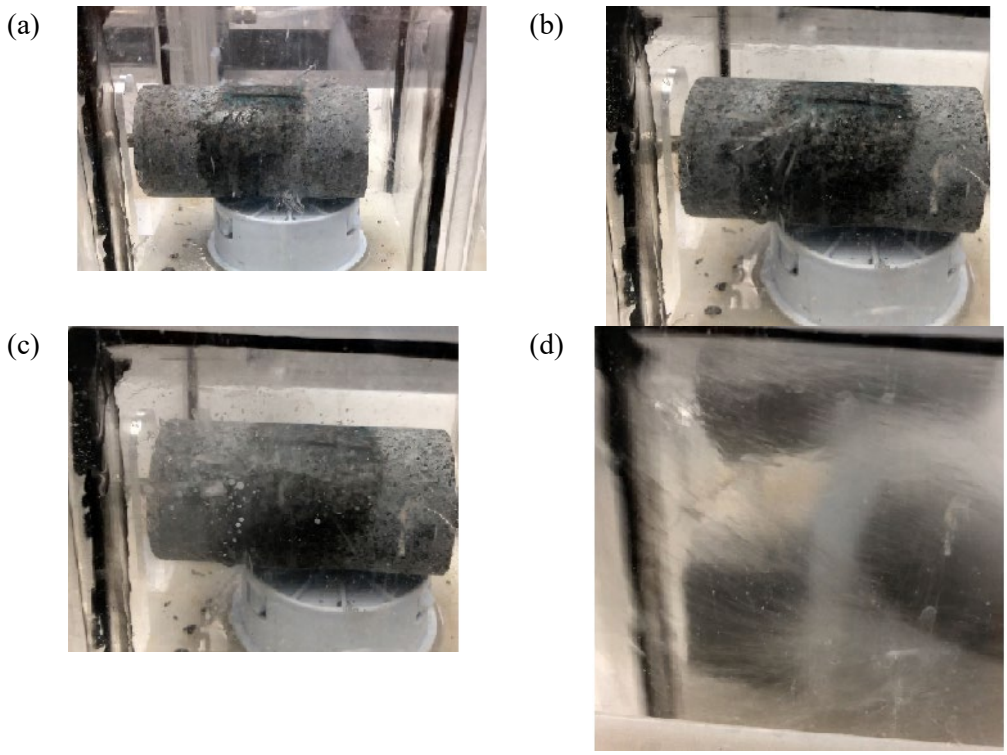

Figure 38 Video-based cyclic injection responses of g2015 with foam as fracturing fluid for events (a) #1: 28.90 s fracture initiated with foam leaking, (b) #4: 132.31 s mixture injection, (c) #5: 132.35 s increased ejection, (d) #6: 132.40 s breakup.

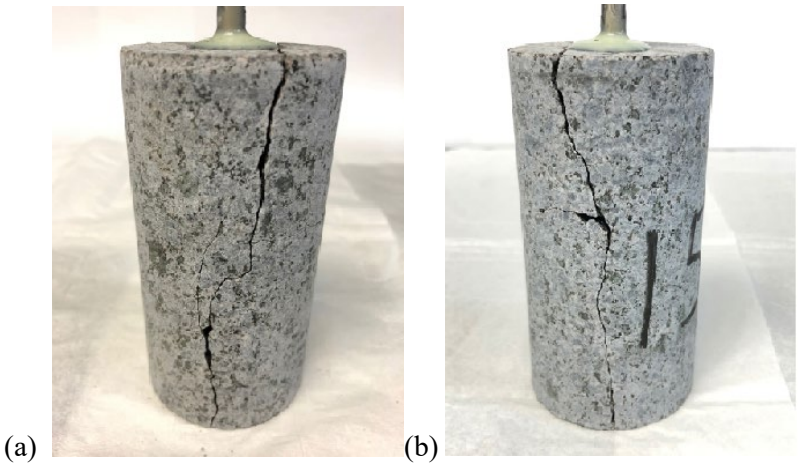

Figure 39 (a) and (b) Post-test images of g2015 induced by cyclic injection in two orientations showing axial fractures with secondary transverse fracture.

6.2.2 G3 Series

Foam cyclic injection tests were completed for 4 specimens in G3 series: g3014 – g3017. Specimen g3017 failed accidentally in a shutdown process and is excluded from the following discussion. The maximum pressures ranged from 13.5 to 18.4 MPa with the minimum pressures around zero. The maximum pressures are 69 to 94% of the monotonic injection breakdown pressure. The cycling started with the amplitude ramped to the maximum level for g3014. For g3015 and g3016, a low-amplitude pre-fatigue cycling was carried out: 13.8 MPa peak pressure with 225 cycles for g3015, and 15 MPa peak pressure with 175 cycles for g3016. No visible variation in injectivity index was seen in the pre-fatigue cycling. All the sensor data and online video are available for the tested specimens.

The number of cycles to failure was 1 to 13. The specimens failed with either axial fracture or in a compound mode showing a primary axial split with transverse fracture developed in half of the cross section. No breakage occurred to g3014, while the other two specimens were broken into the typical three pieces.

6.2.2.1 Timed data and peaks/ valleys

Fatigue responses of g3014 are presented in Figure 40 and Figure 41. The peak pressure for this specimen was at a relatively constant level during the cycling, 13.5 MPa, about 69% of breakdown pressure under monotonic injection. The number of cycles to failure was 13.

The peak mass flow rate fluctuated around a nominal value of 300 g/min. The pressure peak-based injectivity index was relatively flat staying near 4 g/(min*MPa) and increased a little upon the failure. Density peak has a rise and fall variation in earlier cycles and then reached a plateau for the majority of cycling process. The pressure peak-based density had an averaged value of 405 kg/m^3. The foam quality was 70%, and maximum mass rate ratio of gas was 28%.

The system was still capable of holding pressure after specimen failure indicating fracture closure following depressurization. No change in pressure and mass flow rate waveforms was seen in the final cycle of this specimen.

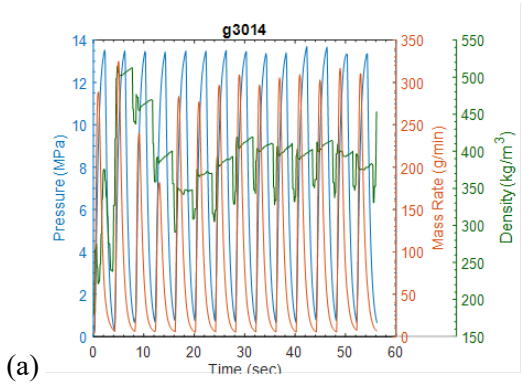

(a)

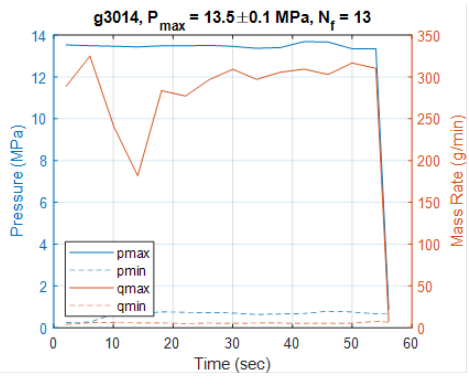

(b)

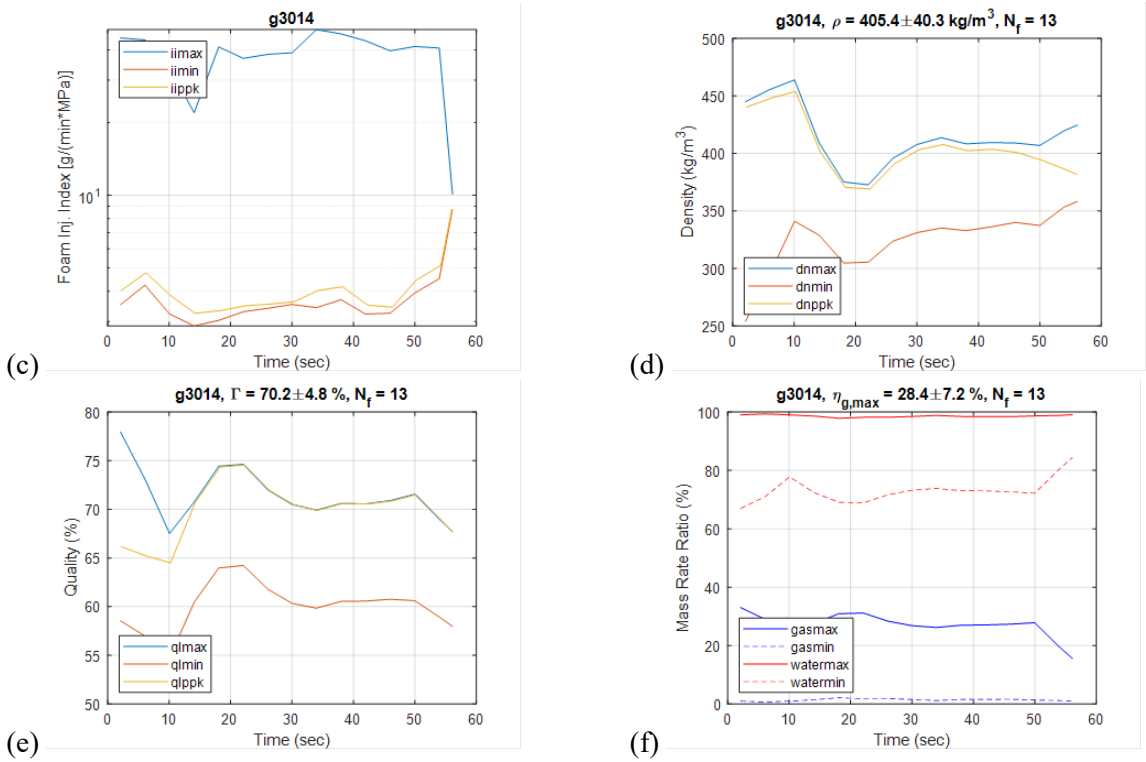

Figure 40 Cyclic injection responses as a function of time for g3014, foam as a fracturing fluid: (a) time data for pressure, mass rate and density, (b-f), extremes for pressure and mass rate, injectivity index, density, quality, and mass rate ratios.

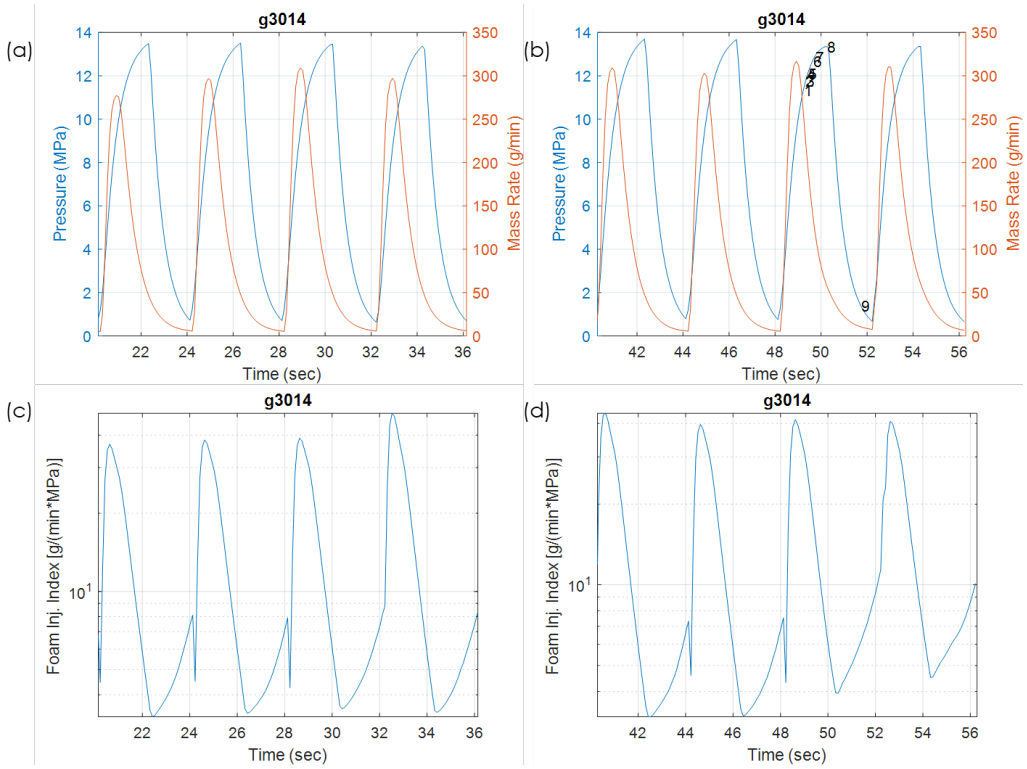

Figure 41 Responses as a function of time for g3014: pressure and mass rate in (a) middle life and (b) final cycles, and instantaneous injectivity index in (c) middle life and (d) final cycles.

6.2.2.2 Video and post-test images

The following observations are made for the images shown in Figure 42 with the following events, where the figure times correspond to those of the number shown in Figure 41.

- #2: 49.32 sec, hairline fracture initiated in middle of specimen.
- #4 and #5: 49.42 and 49.47 sec, foam visibly exiting specimen.
- #9: 51.77 sec, foam ejection increased substantially in the failure cycle; mass flow rate and density both increased; no pressure drop was seen.

The image of the tested specimen is provided in Figure 43, where the surface fracture can be identified along the axial direction with a small angle.

(a) (b)

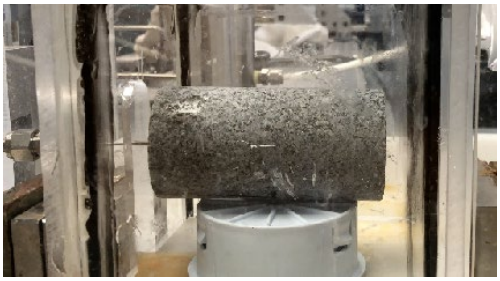

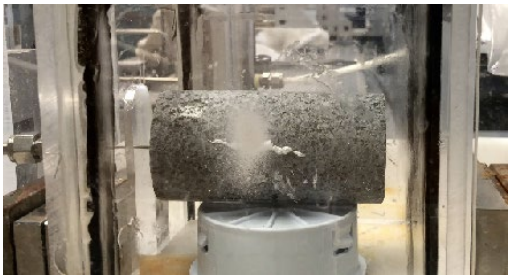

(c) (d)

Figure 42 Video-based cyclic injection responses of g3014 for events: (a) #2: 49.32 sec, hair crack initiated, (b) #4: 49.42 sec, mixture injection, (c) #5: 49.47 sec, increased ejection, (d) #9: 51.77 sec, breakdown where the foamed area extended more than 2/3 of specimen length.

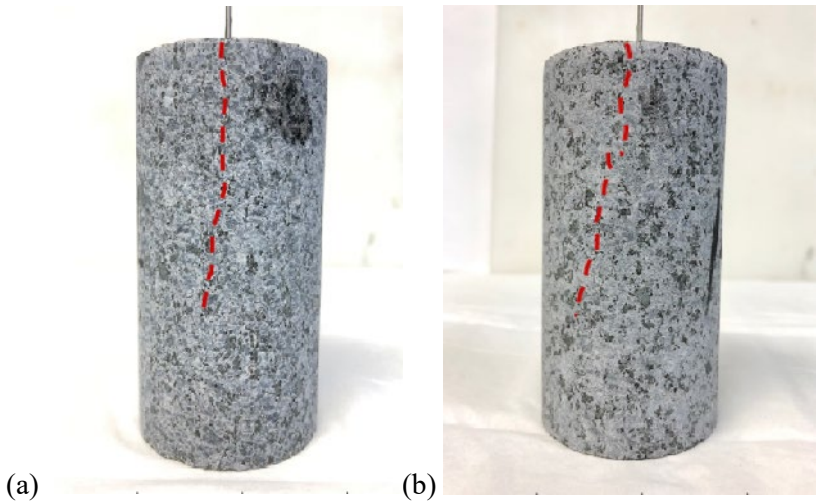

Figure 43 Images of post-test specimen for g3014 in two orientations; red dash line delineates the axial fracture induced by cyclic injection.

6.2.3 Data Summary

6.2.3.1 Fatigue curves

G2 series

The fatigue curves are presented in Figure 44 and Figure 45 in terms of maximum pressure, maximum mass flow rate, and peak pressure- based injectivity index. The maximum pressures for g2016 and g2018 were adjusted slightly during the tests, but are reported as an averaged constant value for each cycling experiment. The injectivity index was observed to increase with cycling. This appears to be a measurement of the degree of fatigue.

For the same peak pressure levels used for the water cycling tests, the mass flow rate for the foam cycling appeared to be higher (Figure 35). This resulted in a higher level of injectivity index. The same trend of mass flow rate was observed in the monotonic injections of water and foam around fracture initiation.

Peak densities were generally higher for cyclic tests compared to monotonic injection. This is likely due to inertial effects related to flow dynamics when filling a closed volume. As a result, the foam quality and gas mass flow rate ratio were relatively lower than for monotonic injection.

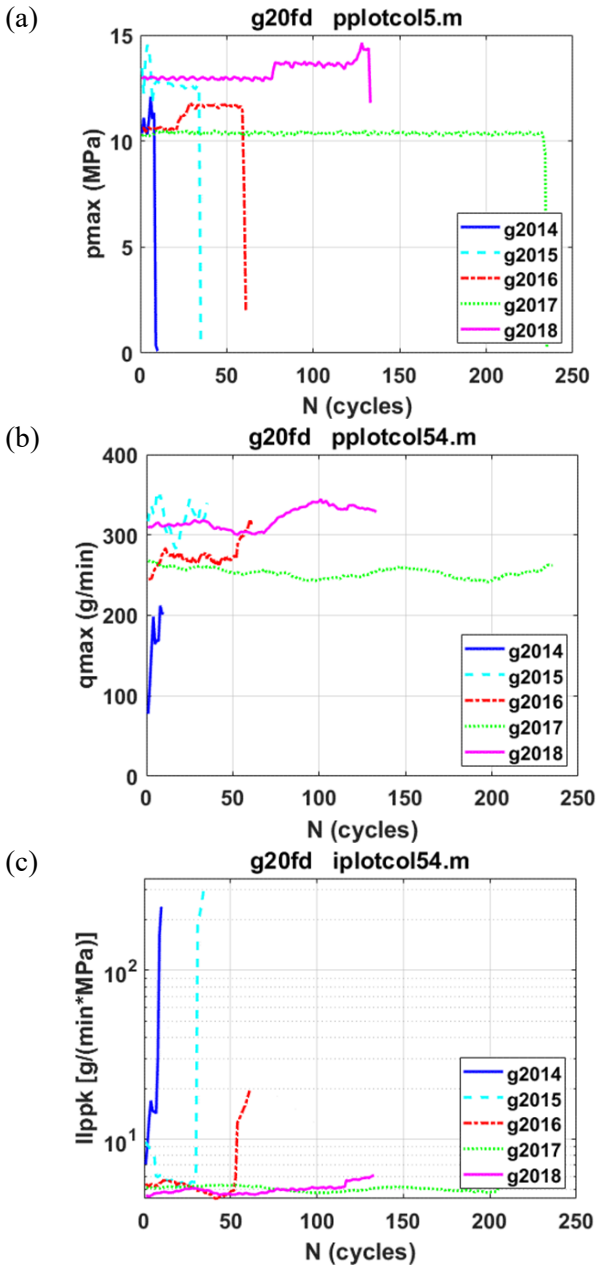

Figure 44 Cyclic injection responses as a function of number of cycles of G2 series for (a) maximum pressure, (b) maximum mass flow rate; (c) pressure peak-based injectivity index; foam as a fracturing fluid.

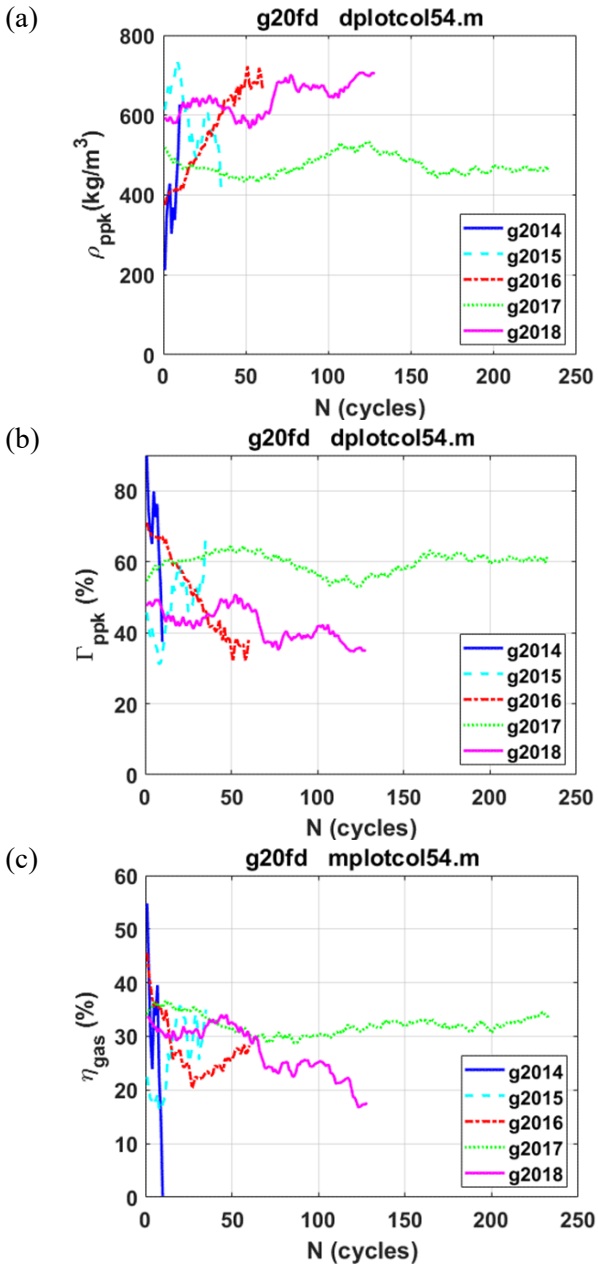

Figure 45 Cyclic injection responses as a function of number of cycles of G2 series for (a) pressure peak -based density, (b) foam quality; (c) gas mass rate ratio; foam as a fracturing fluid.

G3 series

The fatigue curves of cyclic injection for G3 series are illustrated in Figure 46 and Figure 47. The test for g3016 had a relative high density, almost the same level as water, but is still presented in this group. The other two specimens, g3014 and 3015 had a density around 400 Kg/m^3, providing a level of foam quality like that of G2 series foam cycling. The qmax for the latter two specimens dropped for some reason unknown, but the injectivity index showed an inclination of increasing in the cycling, especially in the case of g3014.

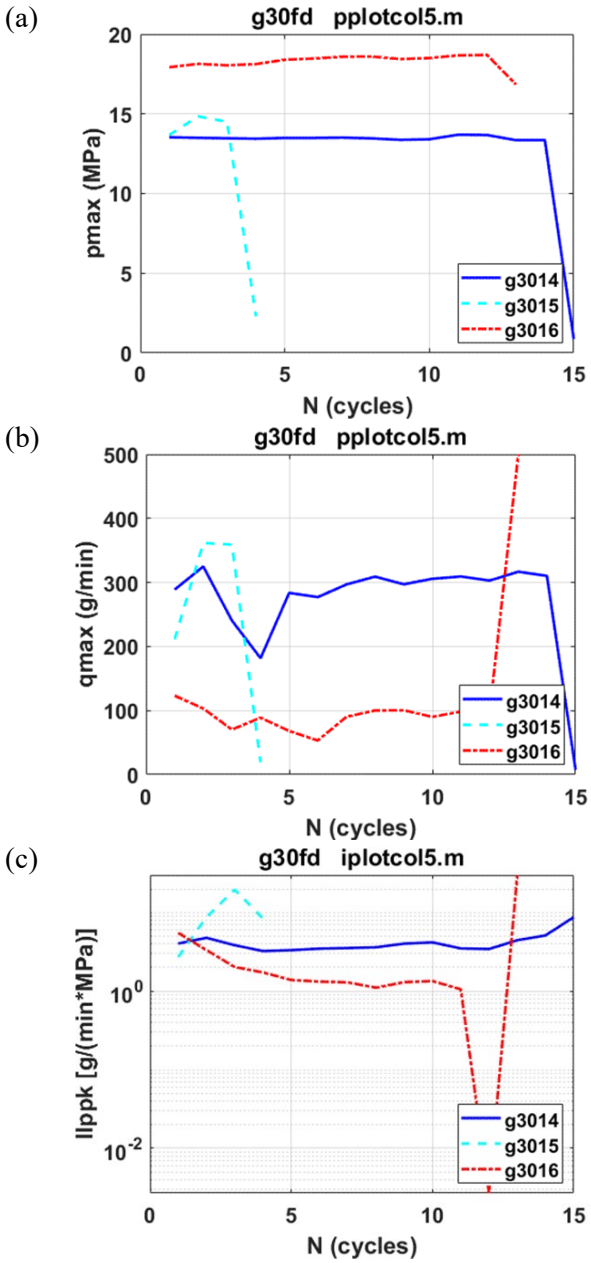

Figure 46 Cyclic injection responses as a function of number of cycles of G3 series for (a) maximum pressure, (b) maximum mass flow rate; (c) pressure peak-based injectivity index; foam as a fracturing fluid.

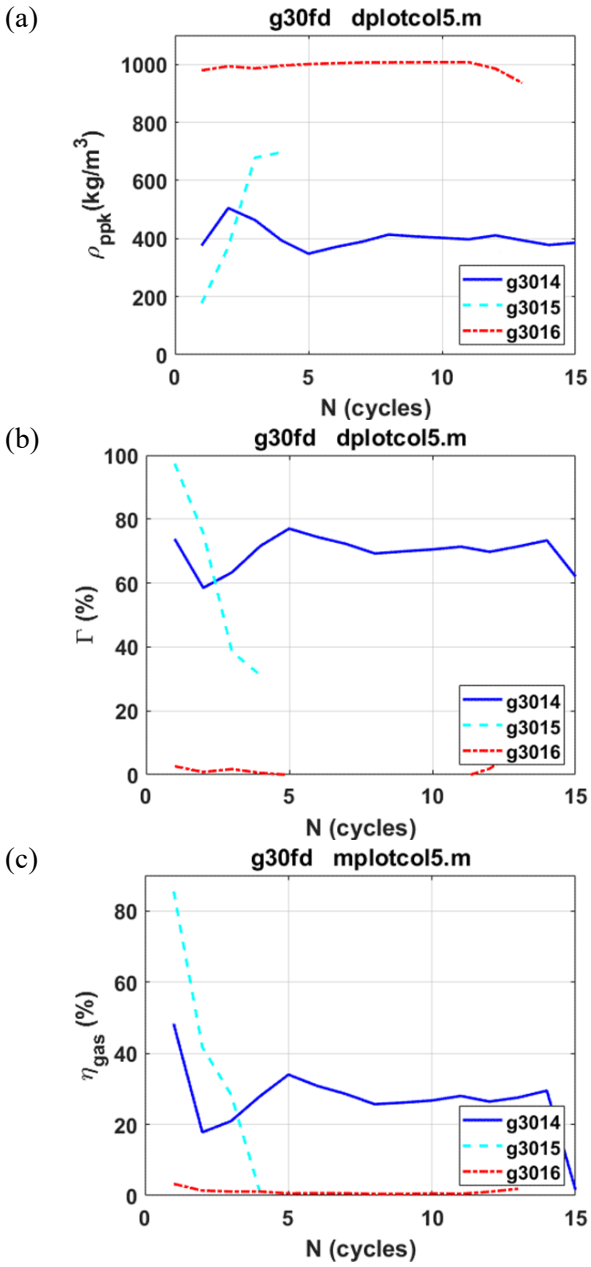

Figure 47: Cyclic injection responses as a function of number of cycles of G3 series for (a) pressure peak-based density, (b) quality; (c) gas mass rate ratio; foam as a fracturing fluid.

6.2.3.2 Summary of cyclic foam fracturing experimental results

Foam cycling and fracturing mechanism

The mechanism of foam cyclic fracturing is similar to that of water cyclic fracturing, as discussed in Section 6.1.2. But there are some unique aspects in foam fracturing using cyclic injection, especially

considering the compressibility of foam and rate-dependent viscosity. More data analysis is required to obtain better understanding of fatigue mechanisms involved.

Statistics of results

The cyclic test results are summarized in Table 15 and Table 16 in terms of maximum pressure, and monitoring-based density, foam quality, and gas mass rate ratio.

- With the maximum pressure ratios between 0.58 and 0.94, cyclic injection produced failure in less than 225 cycles.
- Except for g3016, the density of foam in all the specimens is maintained at a relatively low level, corresponding to a foam quality range between 42 and 87%.
- It was observed that the nominal mass flow rate ratio of gas ranged from 27 to 64%. This is lower than that of the monotonic injection case because of the lower foam quality obtained in cyclic injection.

Table 15 Pressure and Nf obtained for cyclic injection tests using foam as a fracturing fluid

grps	sps	p_{max}	N_f	p_b	p_{max}/p_b
		MPa	Cycles	MPa	
g21fd	g2014	11.00	7	17.80	0.62
	g2015	12.80	34	17.80	0.72
	g2016	11.20	78	17.80	0.63
	g2017	10.40	225	17.80	0.58
	g2018	13.30	180	17.80	0.75
g31fd	g3014	13.50	13	19.60	0.69
	g3015	14.30	1	19.60	0.73
	g3016	18.40	12	19.60	0.94

Note: sps – specimens, p_{max} – maximum/ peak pressure; N_f – number of cycles to failure; p_b – breakdown pressure based on monotonic injection

Table 16 Density, quality, and gas MRR obtained for cyclic injection tests using foam as a fracturing fluid

grps	sps	mdn	sdn	mql	sql	mgmrr	sgmrr
		Kg/m^3		%		%	
g21fd	g2014	340.30	152.90	75.40	17.60	37.50	16.50
	g2015	588.40	266.60	48.20	31.20	27.70	18.90
	g2016	564.20	211.80	49.90	24.20	27.60	14.10
	g2017	476.20	228.50	59.40	25.90	32.20	16.60
	g2018	640.70	218.00	42.30	25.60	27.40	17.00
g31fd	g3014	405.40	40.30	70.20	4.80	28.40	7.20
	g3015	274.40	137.60	86.50	15.40	63.70	31.00
	g3016	999.20	9.70	0.10	1.20	1.00	0.80

Note: 1) sps – specimens; *dn – density; *ql – foam quality; *gmmr – gas mass rate ratio. The symbol * is a place holder for mean or standard deviation. 2) m* - mean; s* - standard deviation.

6.3 SUMMARY OF CYCLIC RESULTS

6.3.1 Experimental Technique

A range of foam quality were observed during cycling. In general, because of high flow rate in cycling, the foam quality was a little lower (42 to 87%) than those in monotonic injection. The large deviation of foam quality is partly attributed to the conditions of the rock sample such as fracture pattern as created by the fracture initiation.

6.3.2 Responses of Granite

In general, experiments found that specimens can be fractured with a relatively small number of fatigue cycles (on the order of 100 cycles) as shown in Figure 48. The fatigue pressure was approximately 70% of breakdown pressure obtained under monotonic injection for water fracturing and 58 - 94% of the breakdown pressure for foam fracturing. This is important because it implies that the use of cyclic injection has the potential to reduce the breakdown pressure in an EGS system no matter if it is with water or foam as the fracturing fluid. This reduced fracture pressure has added benefits of mitigating the risk of micro-seismicity related to reservoir stimulation and reduced stresses on pumping equipment.

The lifetime can be expressed by the ratio of maximum pressure to monotonic fracture initiation pressure as well. The results illustrated that the variation of pattern is similar with the ratios ranging between 0.65 and 1.02.

When pooling all the data points, a tendency is appreciable that the lifetime decreased with increasing pressure amplitude in cycling. The data points can be fit by using the following equation,

$$y = a + b\ log_{10}x,$$

Equation 11

where x – N_f, and y – p_{max}/p_b. The fitting parameters are a = 0.7409, b = -0.0258. It has been seen that the y-axis intercept, a, doesn't approach one as expected in this case. The same equation was applied to the S-N data of rocks induced by mechanical fatigue testing, resulting in a = 0.9455, and b = -0.0278 (Cerfontaine and Collin, 2018). It was realized that the data sets used by the mechanical fatigue covered a variety of materials and testing conditions, and a wide range of number of cycles to failure from 1 to 10^6. The controlling mechanism for the hydraulic cyclic fatigue of granite remains to be investigated. However, the lower value of a in this study shows that there was a unique mechanism activated in hydraulic cyclic fatigue that may not exist in mechanical cyclic fatigue. The curve fitting results are summarized in Table 17, including the data points for granite obtained with open hole specimens (Zhuang et al., 2019b).

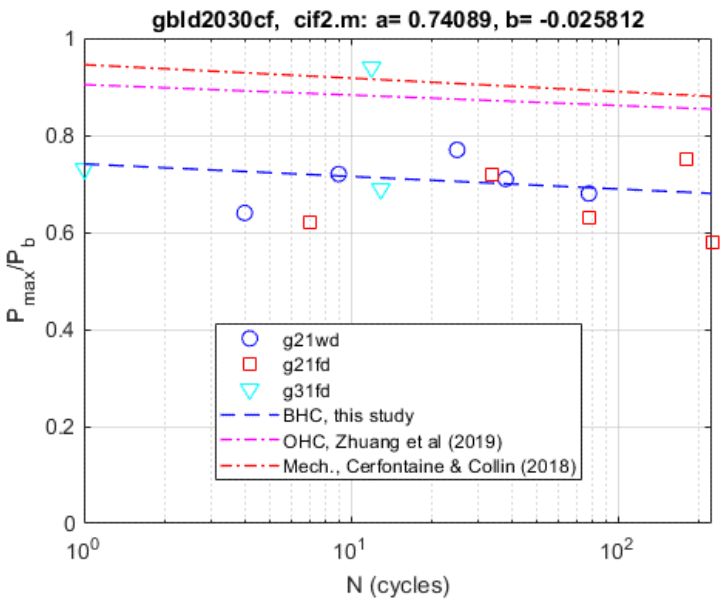

Figure 48 Ratios of maximum pressure in cycling to breakdown pressure in monotonic injection as a function of number of cycles to failure: (a) P_{max}/P_b and (b) fitting for pooled data using $y = a + b*\log_{10}(x)$. g21wd – G2 series with water; g21fd – G2 series with foam; g31fd – G3 series with foam; BHC – blind hole cylinder; OHC – open hole cylinder, Mech. – mechanical fatigue.

Table 17 Curve fitting coefficients of fatigue test data

	a	b	N	Testing	Specimen	Notes
Granite	0.7409	-0.0258	13	Hydraulic	Blind hole cylinder	This study
Granite	0.9044	-0.0215	33	Hydraulic	Open hole cylinder	Based on Zhuang et al. (2019b)
Rocks	0.9455	-0.0278	N/A	Mechanic	Various geometrics	Cerfontaine and Collin (2018)

Note: N is the number of data points used in curve fitting

7. DISCUSSIONS OF FRACTURING RESULTS

7.1 FAILURE MODE AND LOCAL STRESS

The failure mode of fracturing was investigated using the analyses of post-test specimens and online videos. There were three modes of failure involved with the fracturing process of a blind hole granite specimen as delineated in Figure 49. Most of the failures have been shown to be associated with axial split. According to the statistics of 29 tested specimens, about 24% had a pure axial split, 66% a primary axial split with secondary transverse fracture, and the rest with slant facture.

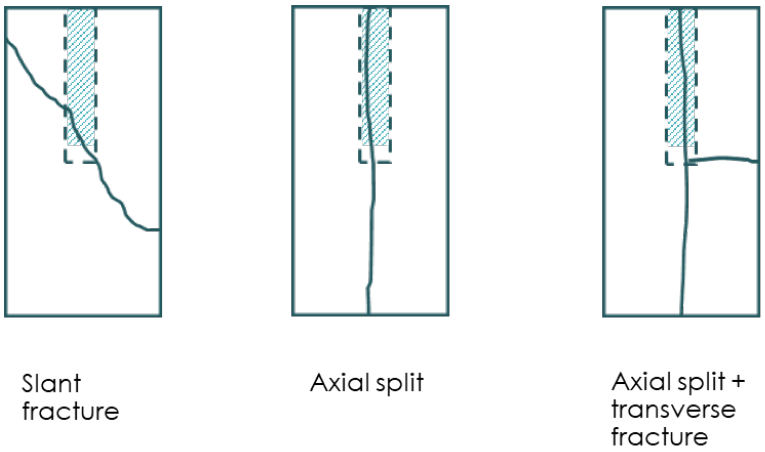

(a)

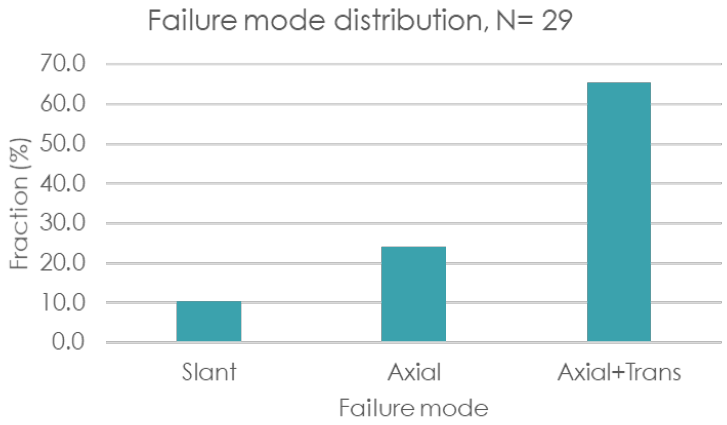

(b)

Figure 49 (a) Failure mode and (b) fraction of failure modes. The blind hole is delineated by a dash rectangular box where the shadow area is bonding zone of tube, and the un-shadow area in the bottom is injection zone.

The failure of the cylinder is, therefore, dominated by the tangential stress. We can idealize the stress state by using a thick-walled cylinder equation. In such case, the fracture initiation occurs when the local

tangential stress at the inner surface of the hole exceeds the tensile strength of the rock. The tangential stress of a thick-walled tube can be expressed as follows (Finnie and Heller, 1959),

$$\sigma_t = \frac{R_i^2}{R_o^2 - R_i^2}\left(1 + \frac{R_o^2}{r^2}\right)p$$

Equation 12

where p is the inner pressure, Ri and Ro are the inner and outer radii of tube, r is the radius from tube axis. The inner tangential stress can be evaluated at r = Ri. The resolved tensile strength for G2 and G3 series and water and foam fracturing are between 16.3 and 20.7 MPa (Table 18). This agrees well with the rupture modulus reported for this material (Coldspring, 2022). The G3 series produced a tensile strength higher than G2 series, perhaps because of size effects.

Table 18 Inner tangential stress for thick-walled cylinder

	p_{fi}	R_i	R_o	σ_t	Fluid	Note
	MPa	mm	mm	MPa		
G2	15.205	4.763	25.400	16.313	water	g25wsm
G3	20.378	2.381	25.400	20.739	water	g35wsm
G2	15.960	4.763	25.400	17.123	foam	g26fsn
G3	17.945	2.381	25.400	18.263	foam	g35fsn

Note: p_{fi} – inner pressure at fracture initiation; R_i - inner radius of hole; R_o – outer radius of cylinder, σ_t – tangential stress at the inner radius.

It is worthwhile noting that the initiation of fracture did not generally trigger complete specimen failure as is often seen with brittle materials, even without confining pressure. It is, therefore, possible to study the crack growth process in the specimen. Subcritical crack growth (SCG) prior to breakdown and water use are discussed in Section 7.3.

7.2 INJECTION MODULUS

The scatter plots of fracture initiation pressures are presented as a function of injection modulus as shown in Figure 50. Injection moduli are lower for foam experiments due to the compressibility of gas contained within the foam and its lower density at the pressure values of the experiment (Wanniarachchi et al., 2018). In experiments involving specimens with smaller hole diameters, a higher pressure was reached resulting in a much higher injection modulus.

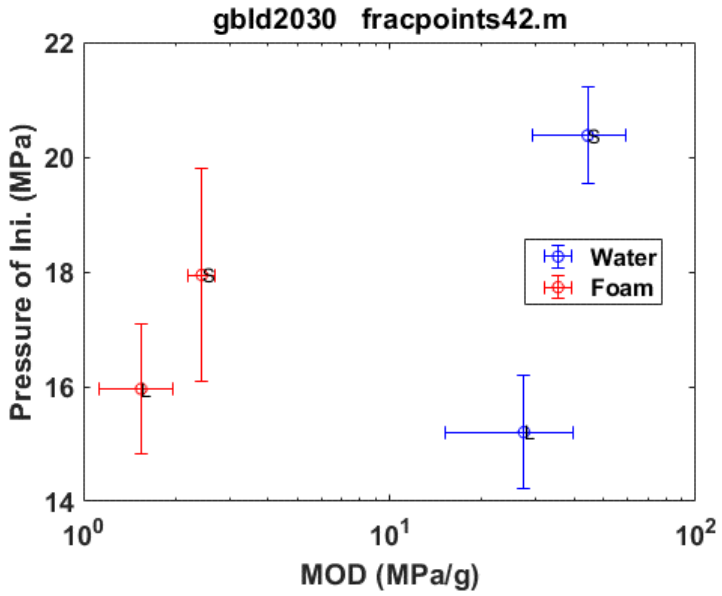

Figure 50 Fracture initiation pressures related to injection moduli based on monotonic tests. Labels L and S correspond to G2 and G3 series. Error bars have a half of standard deviation. Same comments apply in the following.

It is believed that the solid- fluid interaction plays a role in this procedure (Cheng, 2016). There are at least two aspects involved with the mass or volume injected. The first is the volume variation of the space of the injection zone induced by the mechanical loading. For the given dimensions of the specimen (for example G2 series, that has a diameter of 3/8" and height of ¼") and injection pressure, the deformation of the hole wall is related to the elastic properties. Determination of an exact volumetric change may require one to resort to numerical analysis, but for the dense brittle rocks like granite, the rupture strain is generally low. The second is related to the flooding of rocks. The mass consumed in the linear pressurization is mainly by the saturation process (Zhuang et al., 2019a). The total volume consumed ΔV_t by an injection process can be expressed as follows,

$$\Delta V_t = \Delta V_{mech} + \Delta V_p, \quad \text{(a)}$$

$$\Delta V_p = \varphi \Delta V, \quad \text{(b)}$$

$$V_p = \varphi V, \quad \text{(c)}$$

Equation 13

where ΔV_{mech} is the volume variation of injection zone caused by mechanical loading, ΔV_p is the flooded pore volume, ϕ is the porosity of the material, ΔV is the flooded specimen volume, and V is the specimen volume. Substituting the specimen dimensions (Section 4.3) and porosity of 0.02 for charcoal granite (Cheng, 2016) into Equation 13, a total pore volume can be estimated as 4.119 cm^3 for a G2 specimen.

Focusing on water as discussed in Section 5.1.3, one has a total mass of 0.818 g, or volume of 0.818 cm^3 at the fracture initiation. Disregarding the volume amount consumed by the mechanical expansion of the injection zone, the saturated area was thus estimated to be about 19.86% of the total pore volume, $\Delta V_p/V_p$, for the granite specimen at the fracture initiation in the monotonic injection using water. This ratio should also represent the flooded volume fraction of the specimen, $\Delta V/V$. A numerical analysis of the diffusion process would provide a more detailed picture.

7.3 CRACK GROWTH AND INJECTIVITY VARIATION

7.3.1 Crack Growth

Surface crack growth or fracture propagation as measured by length of the fracture in the axial direction, generally corresponded to the increase in II (Figure 51). For water fracturing, the subcritical growth can take on a wider range of mass. The steep bottom of the injectivity index curve is generally associated with the point of fracture initiation. However, the fracture initiation may not be visible on the specimen surface because it is initiated internally. So, there was a delay between the external fracture appearance and the fracture initiation.

In the case of foam fracturing, the change in II was not significant while the breakdown occurred almost right after the fracture initiation with a short period of sub-critical growth. Note that the empty square marker in Figure 51 signifies the breakdown of each specimen. The abrupt rise in II after that, in fact, corresponded to the post-failure stage.

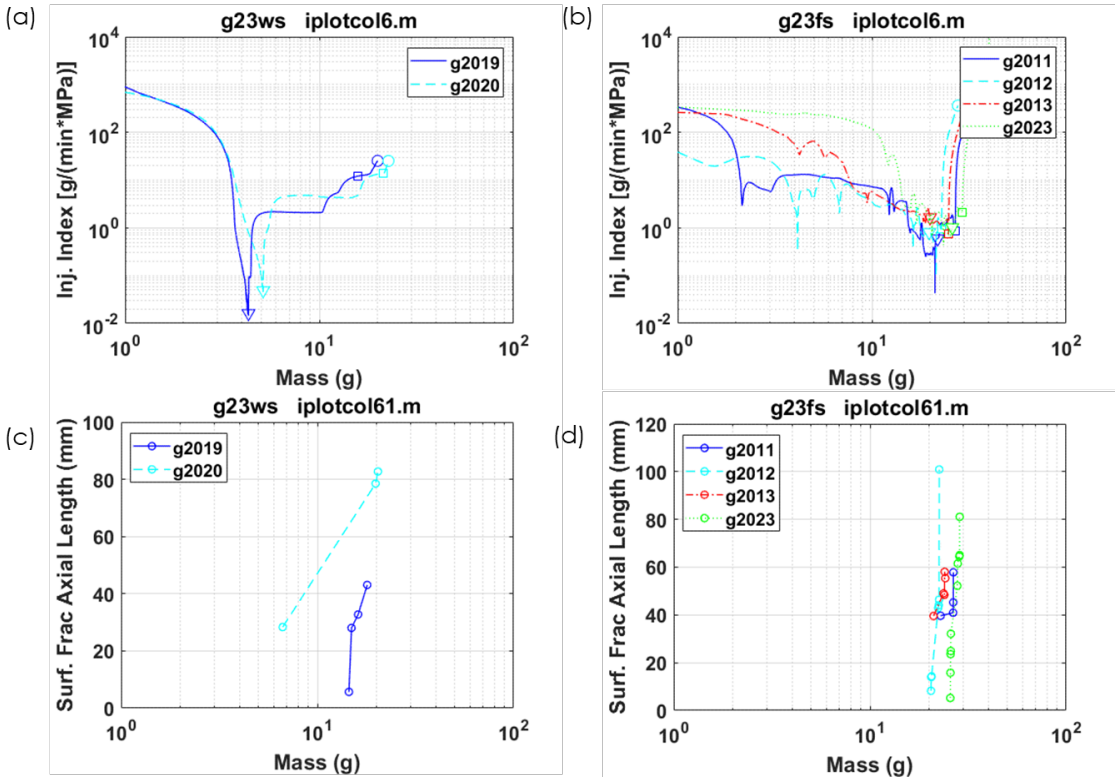

Figure 51 Responses of G2 series tests as a function of injection mass: injectivity index for (a) water fracture and (b) foam fracturing; surface fracture size for (c) water fracturing and (d) foam fracturing.

Similar image analysis was carried out on the footages for G3 series, and the results are presented in Figure 52. In a couple of water fracturing specimens, the subcritical growth, in fact, occurred within a very narrow band of the mass axis near fracture initiation. The dense subcritical events corresponded to the jump in injectivity index. The same was true for foam fracturing of g3011. Specimen g3007 had a

very high foam density and was excluded from the discussion above. It is shown here as a reference to illustrate the correlation between the evolution of injectivity index and crack growth.

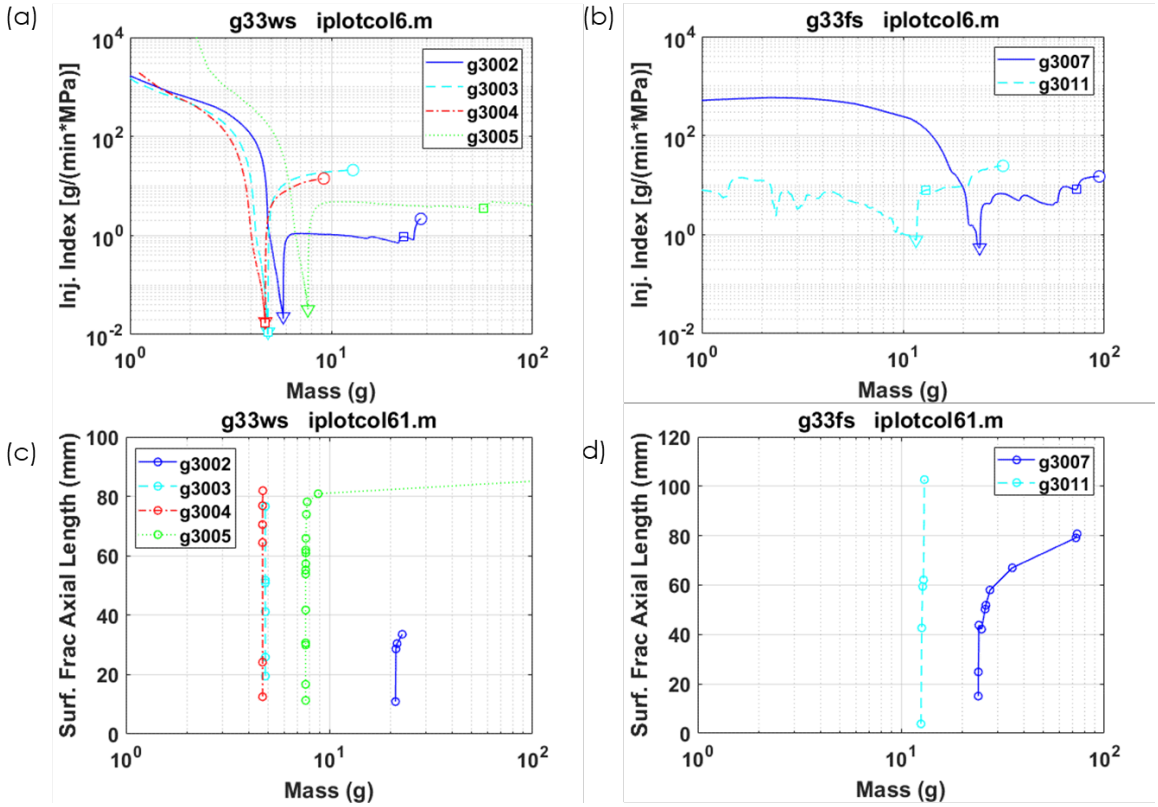

Figure 52 Responses of G3 series as a function of injection mass: injectivity index for (a) water fracture and (b) foam fracturing; surface fracture size for (c) water fracturing and (d) foam fracturing.

7.3.2 Injectivity Enhancement

We will examine the characteristic points to quantify the responses, namely fracture initiation and breakdown as shown Figure 53. The term WinF represents the water contained in a foamed fluid, while INI and BKD correspond to data averages at fracture initiation and breakdown, respectively.

In terms of the mass rate shown in the upper view, we have observed that the II was distributed in a very wide range for water fracturing. In foam fracturing, both fracture and breakdown II points are located in the upper right, indicating the high injectivity of this fluid overall. By focusing on the water in foam (in purple color indicated by arrows), we found the II was shifted down substantially and approached that of water. It is believed that, while the high II of foam delivers the pressurized fluid effectively in fracturing, it is the low II of water that reduces water use. It is seen that there is a clear trend between the IIs and mass rates at the characteristic points of fracturing. Further data analysis can be used to reveal the relation involved.

The enhancement of injectivity as a scatter plot of mass is illustrated in the lower view. The closeness of fracture and breakdown points of the water part in foam (in purple color indicated by arrows) to the fracture points of water demonstrated that the completion of fracturing can be realized by the water

amount close to that of water in fracture (initiation). As a result, the final use of water is lower in foam fracturing.

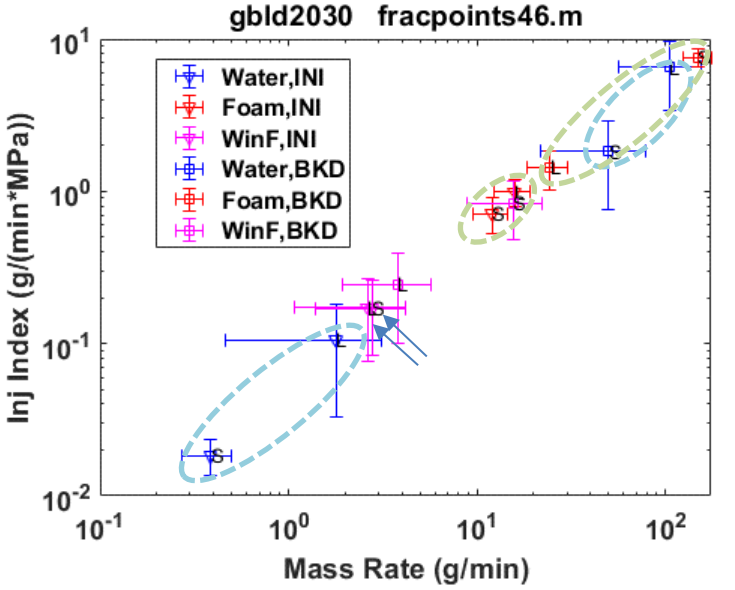

(a)

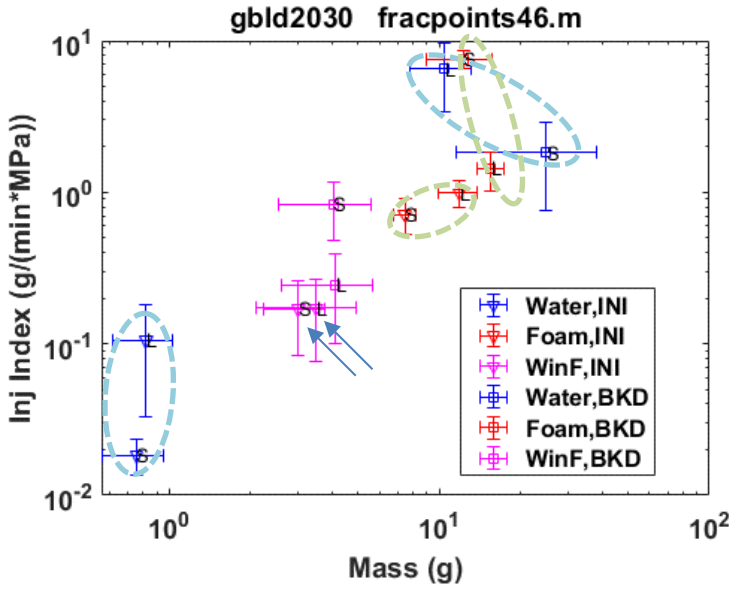

(b)

Figure 53 Characteristic injectivity indices based on monotonic injection as related to: (a) mass rate and (b) mass. Mass amount of filling internal tubes was removed. WinF – water in foamed fluid; INI- fracture initiation; BKD- breakdown are presented.

7.3.3 Cyclic Injection

For cyclic injection, we observed that faster II increase was related to a shorter fatigue life as discussed in Sections 6.1.2 and 6.2.3. Additionally, a higher initial II level corresponded to a faster II rise. Both

observations imply a greater amount of initial structural damage within the test specimen. The degree of damage and damage evolution depended on the pressure amplitude of cycling as would be expected for a typical fatigue process. This also suggests that the lifetime of specimens should be related to the pressure amplitude, which is also what was observed in this project (Sect. 6.3). Apparently, to obtain additional data points would definitely improve the confidence level of use of the established relation to predict the lifetime performance of the rock under cycling hydraulic loading.

In cyclic injection, footages generally showed surface leaking as a result of fracture initiation and fracture propagation. The subcritical growth is normally not seen from video until the final failure cycle. There may be micro subcritical events happening internally, but that cannot be resolved using the current analysis tool and measurement approach.

7.4 WATER REDUCTION AND REPLACEMENT

7.4.1 Monotonic Injection

Focusing on characteristic pressures as a function of mass rate and mass in the scatter plots, one can see at the breakdown, the water mass rate for foam fracturing was at least one order of magnitude lower than that of water fracturing, Figure 54 (a). For example, in G2 series, the breakdown water rate was reduced from 105.13 in water fracturing to 4.76 g/min in foam fracturing. The difference in water use has two components for this experimental configuration. First, a large amount of water has been replaced by the gas as defined by the mass rate ratio of the fluid. Second, we observed that the crack growth occurred over a very short period for foam fracturing. This is largely due to the compressible nature of foamed fluids and their ability to continue to supply energy to extend fractures as the fluid expands. Water, by comparison, must continue to be injected to extend fractures because it is incompressible. It shall be noted that the scatter plot of data in terms of mass rate actually presents potential to maximize the water replacement in a foam fracturing task as shown in Sect. 5.2. For example, decoupling of foam mass flow rate of g2013 into water and gas parts suggested that the gas mass rate ratio could reach as high as 80% near breakdown (Figure 17).

The scatter plot in Figure 54 (b) illustrates pressure points related to three mass quantities: water mass in water fracturing, foam mass in foam fracturing, and water mass in foam fracturing. The last item was based on the measurements in foam fracturing with the gas mass removed. In all the masses presented, the amount in filling the inner spaces of the tube and specimen hole was removed. The water mass in foam fracturing was usually higher than in water fracturing at fracturing initiation. With similar breakdown pressures, the water mass in foam fracturing was down from 10.44 g for water fracturing to 5.17 g in G2 series, representing more than 50% water reduction. This would be the amount of water reduction that can be achieved with the current configuration and foam compositions. In G3 series, while the breakdown pressure in foam fracturing is lowered in comparison to water fracturing, a water use reduction of 84% has been reached, from 24.92 down to 4.05 g.

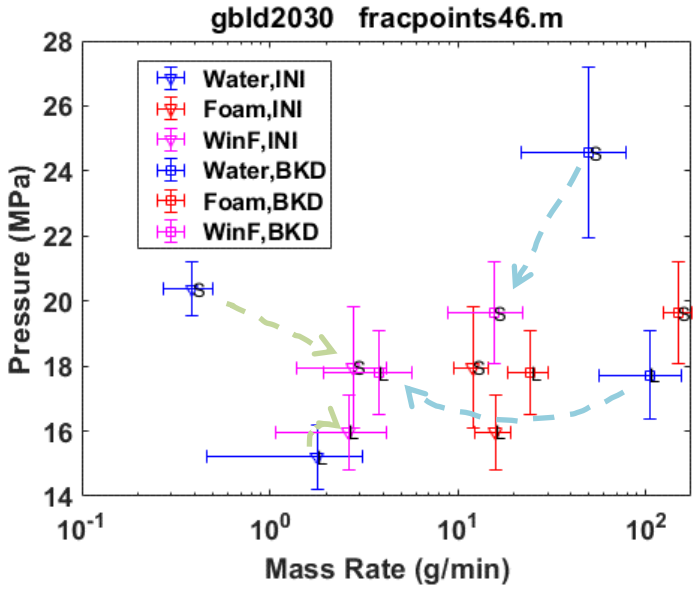

(a)

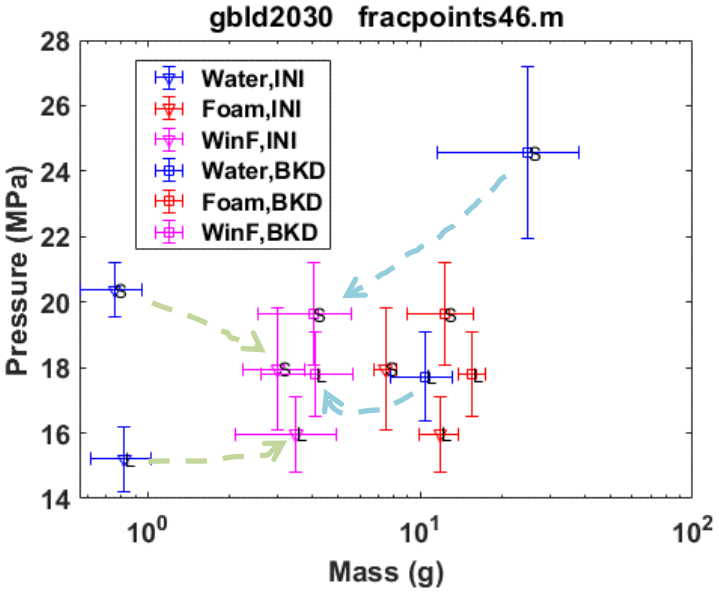

(b)

Figure 54 Characteristic pressures based on monotonic injection as related to: (a) mass rate and (b) mass. Dashed line delineates the water use reduction direction. Mass amount of filling internal tubes was removed. WinF – water in foamed fluid; INI- fracture initiation; BKD- breakdown are presented.

The after-fracture initiation behavior of the system can be understood better if one focuses on the segment of the pressure vs. mass curve from fracture initiation to breakdown (Figure 6). The quantities taken from the segment define the difference in pressure in the y-axis and in mass in the x-axis and are illustrated in Figure 55. The term WinF has the same meaning as defined above. After fracture initiation, further pressure increase was enabled by the pressurization process to overcome the pressure loss with tube and fracture flow and thus fueled the SCG. The pressure and mass increases for the extended pressurization were limited but relatively high in the case of water. An injection modulus can be calculated for the

segment of pressure vs. mass curve after fracture initiation: $\Delta P/\Delta m = (P_b - P_i)/ (m_b - m_i)$. The results showed that the injection moduli have been reduced for both water and foam, but it appeared to be more substantial for water fracturing from 18.58 – 26.97 MPa/g at fracture initiation down to 0.17 – 0.26 MPa/g, depending on hole size. On the other hand, that for foam fracturing reduced less from 1.35 – 2.40 MPa/g to 0.35 – 0.49 MPa/g. The higher remaining injection modulus indicates a stronger pressure delivery of foam after fracture initiation.

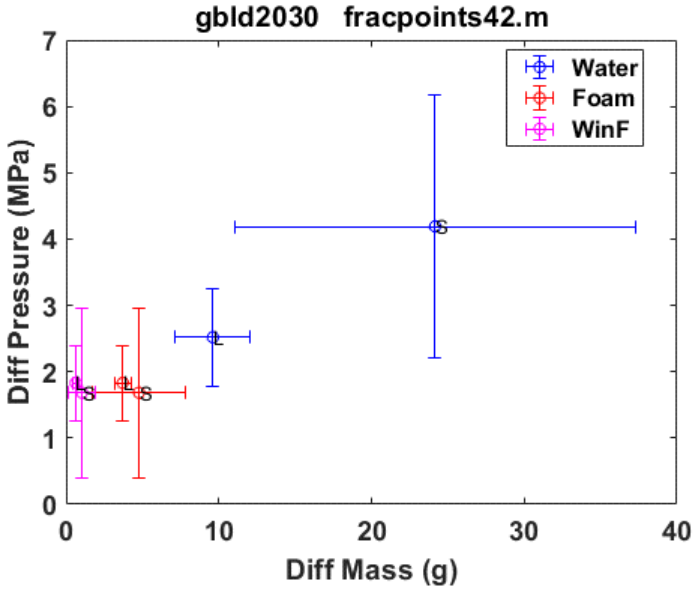

Figure 55 Differential pressure versus differential mass based on monotonic tests, where the differences are evaluated between fracture initiation and breakdown. WinF – water in foamed fluid.

7.4.2 Cyclic Injection

As discussed in Sections 5.2.3 and 6.2.3, foam density in cyclic injection was generally higher than in monotonic foam injection, and thus foam quality and gas MRR were lower. This was mainly due to the lower injection pressure levels and higher mass flow rates used in cyclic injection. Further discussion is presented in the next section.

Water use in a cyclic injection remains to be investigated. In this study, foam was discharged in the depressurization half cycle. The effect of foam discharge and recycling on the final water use is beyond the scope of this study and remains to be investigated in the future.

An additional strategy for increasing water replacement would be to explore other candidate foams like CO_2 or supercritical CO_2 as a gaseous phase. These gases have a density much higher than N_2, and thus are more capable of displacing water, especially at high pressures.

7.5 CYCLIC FATIGUE

7.5.1 Mechanical Fatigue

Natural rocks contain defects such as cracks and pores. Under engineering loading, the rock deformation is initially linear and transitions to nonlinear behavior when pores begin to compact and internal fractures close. The stages of deformation are dominated by the cracks and matrix corresponding to 1) the closing of cracks, 2) collective response of crack- matrix system, and 3) reactivation and propagation of cracks at the failure. If the test unloads the specimen prior to failure, and the closed cracks open, the result is hysteresis with a strain- stress loop (Scholz and Kranz 1974; Cerfontaine and Collin, 2018). Whether cracks are activated depends on the orientation and size of the cracks for a given load.

For a cyclic test under constant amplitude, a repetitive process of closing and opening of cracks occurs. Depending on the orientation of the crack, the effect could include the wear of surface asperity, the mobilization of a wing crack if the friction is overcome, and so on. A mobilized tip means that another crack can be triggered nearby. In many cases, the material degrades because of cyclic fatigue attributed to these phenomena. The observation is that the sample may be failed by an applied load lower than its monotonic strength, well known as SCG (Atkinson, 1984) as discussed above. This is significant because it offers the theoretical basis for exploring the fatigue of materials in hydraulic fracturing.

The fatigue tests conducted in rock mechanics is usually with a mean stress applied, and it can be regarded as an equivalent process of SCG. Stress corrosion is one of the mechanisms involved with this process (Atkinson, 1984). It is assumed that strained bonds close to the crack tips react more easily with environmental agents and these bonds are broken at a lower stress level (Michalske and Freiman, 1983). Furthermore, the environmental weakening can be promoted by the presence of water and material anisotropy (Nara et al., 2012).

The fatigue life of rocks depends on cyclic amplitudes as expected for engineering materials. The data points on a S-N plot are extremely scattered, being related to many factors including materials and testing conditions (Cerfontaine and Collin, 2018). While examining the strain response of rock under a constant stress amplitude, one can see the fatigue curve resembles that of creep behavior; namely, the rock sample would display a process with the stages of stabilizing, stationary and accelerating (Attewell and Farmer, 1973). This is interesting because it implies that both creep and fatigue share a similar damage mechanism. While primary mechanical parameters like strain, secant modulus, and energy dissipated are used as responsive quantities for monitoring (Momeni et al., 2015), some secondary quantities (Cerfontaine and Collin, 2018) were employed as well including wave velocity (Xiao et al., 2010), AE counts (Xu et al., 2009; Trippetta et al., 2013), and permeability (Wang et al, 2017a). In this study, we demonstrated in Sections 6.1.2 and 6.2.3, a relevant quantity like injectivity index can be monitored in a cyclic process to measure and characterize the fatigue response of granite in foam fracturing.

7.5.2 Hydraulic Fatigue

No explicit interpretation is available regarding the fatigue mechanism of hydraulic fracturing. Here we mainly focus on the role of water, including 1) mechanical impact, 2) erosion, 3) pore pressure on the strength of rock, and 4) stress corrosion.

Firstly, there are microprocesses, including crack closing and opening, and surface frictional wear, that occur to the cracks with a proper orientation and position.

Secondly, the pressurization imposes a surface load on the solid; the stress field would be favorable for radial cracks should the stress exceed the strength. The depressurization creates a tensile stress field, on

the other hand, and has potential to generate a crack in the conferential direction. The repetitive pressurizing and depressurizing actions would promote the interaction of different fracture systems, resulting in isolation and dislodgement of the grains and particles. Such an erosion process has been investigated intensely previously in a variety of materials using various experimental methods, including the laser induced cavitation approach (Wang et al., 2009; Ren et al., 2010a, 2010b, 2012; Wang et al. 2016, 2017b, 2020b).

Thirdly, cyclic injection could produce a repeatable injection curve (pressure as a function of mass) as long as the pressure is within the level of fracture initiation. This means that the solid skeleton behaves elastically within the pressure range, in which water is soaked in pressurization and dispelled in depressurization. In certain conditions like the saturated and undrained, pore pressure exists and alters the stress state of the rock. The effect of pore pressure on the strength of rock has been a subject in rock mechanics textbooks (Jaeger et al., 2007) and previous studies (Tao and Wang, 1987; Baud et al., 2000). Once the surface is fractured, water seeps into the crack and loads directly on the fresh fracture surface. The fracture flow changes the stress field, which in turn alters the opening of cracks and the permeability of rocks. In hydraulic cycling, the fracturing and saturation has been evolved alternately during the cycling resulting in the unique waviness of the mass rate profile.

Finally, dissolution of chemical bonds near a crack tip was reported in calcarenite (Ciantia et al., 2015). The level of the dissolution in granite may also depend on environmental factors like temperature, remaining a subject of research in future.

7.5.3 Field Cyclic Fatigue

Cyclic fatigue has been explored in cyclic stimulation in a couple of geothermal sites (Hofmann et al., 2019; Zang et al., 2019). The period of cycle varied from hours to seconds that were set up in the long, middle, and short terms of injection protocol with cyclic pressure lower than the breakdown pressure anticipated in conventional stimulation. The essence of cyclic stimulation lies in the use of depressurization to mitigate the effect of one-time energy release on micro seismicity involved with conventional stimulation. The repeated dynamic injection, such as that used in this study, serves the same purpose.

It is noted that this approach is different from that of delayed initiation of fracture (Lu et al., 2015) or creep rupture in which the pre-determined creep load, lower than the breakdown strength obtained under monotonic loading, is applied to the materials to initiate breakdown by making use of time- dependent effects. In the delayed initiation of fracture approach, the release of stored energy is momentary and dynamic, while for cyclic injection, the release of stored energy is intermittent and controlled.

The results of cyclic injection are shown to be preferable to reservoir stimulation. It has been seen that a more connected fracture network can be created by using cyclic injection than that for monotonic injection (Zang et al., 2019; Zhuang et al., 2019b). A well-developed fracture network in a reservoir can provide a high efficiency of heat exchange as required by EGS. In this project, the re-constructed fracture surfaces by using the surface trace coordinates of the fractures showed a little increase in fracture surface area in foam cycling than in foam monotonic injection. Additional morphological data can be collected to further evaluate the effect of cycling injection mode.

While it makes use of cyclic fatigue to reduce the breakdown pressure with many benefits, cyclic injection may also bear some downsides. One of the concerns is the operation expense because the cyclic fatigue process can be longer than a monotonic injection process. The operational cost can be related to the pump energy or injection energy consumed in a fracturing job, E, which can be expressed as

$$E = \int P \cdot \dot{m} / \rho \cdot dt \ ,$$

Equation 14

where P, $\dot{m}$, ρ have the meanings as specified in Sect. 4.4. A preliminary analysis of injection energy was conducted for water fracturing using data of G2 series, and the E was estimated to be 153 ± 61 J and 340 ± 269 J for monotonic and cyclic injections, respectively. The analysis has removed the amount of water mass used to fill the cavities but not pressurize the specimen.

Apparently, the energy consumption in the cyclic injection was higher than the monotonic injection, which is mainly because of a relatively high mass flow rate used in cycling. However, the pump energy data for hydraulic fracturing jobs are usually not available in the field. A numerical study, conducted by Zang et al. (2013), revealed that the accumulative seismicity energy can be reduced by 78% using cyclic injection with the pump energy increased by only about 39%.

As mentioned above, the major motivation to introduce the cyclic injection into hydraulic stimulation is to suppress the seismic energy. Therefore, the final adaption of cyclic injection in an EGS site is subjected to cost and risk analysis.

The injection scheme obviously needs to be optimized if the cyclic injection is recommended to control the seismicity in an EGS site. The waveform of cyclic injection and the injection parameters for a maximized reduction of breakdown pressure and a maximized use of fracturing fluids can be studied by using a laboratory setup in the future. The experimental work described in this report focused on specimen pressurization without confining pressure. The effect of confining pressure on the fracture initiation and development for the materials under foam fracturing remains to be studied. Further discussion is given in Section 9.3.

8. FOAM CHARACTERIZATION

8.1 TEST SETUP AT TEMPLE UNIVERSITY

A foam testing apparatus, as shown in Figure 56 and Figure 57, has been developed to test and characterize performance of foams in a combinational condition of temperature and pressure (Thakore, et al., 2021). The current system is capable of testing foam pressures up to 2000 psi and temperatures up to 200°C.

The foam base solution was prepared using the procedure developed in this project (Thakore, et al., 2020; Thakore et al., 2021). The pressure of the foam was controlled by simultaneously adjusting i) the pressure of the injected gaseous phase through a pressure regulator, and ii) the pressure of the liquid phase by the pump setting. The settings in other devices, such as the accumulator and the back pressure valve, were adjusted accordingly. The foam quality was controlled by adjusting the flow meters. This study focused on high quality foams (~ 90% gas volumetric fraction).

After the foam homogeneity was obtained, the foam was injected into a preheated view cell. Once the foam filled the view cell, the valves was closed, and the height of the foam recorded using a digital camera. A mirror was placed in the oil bath next to the view window to assist observation.

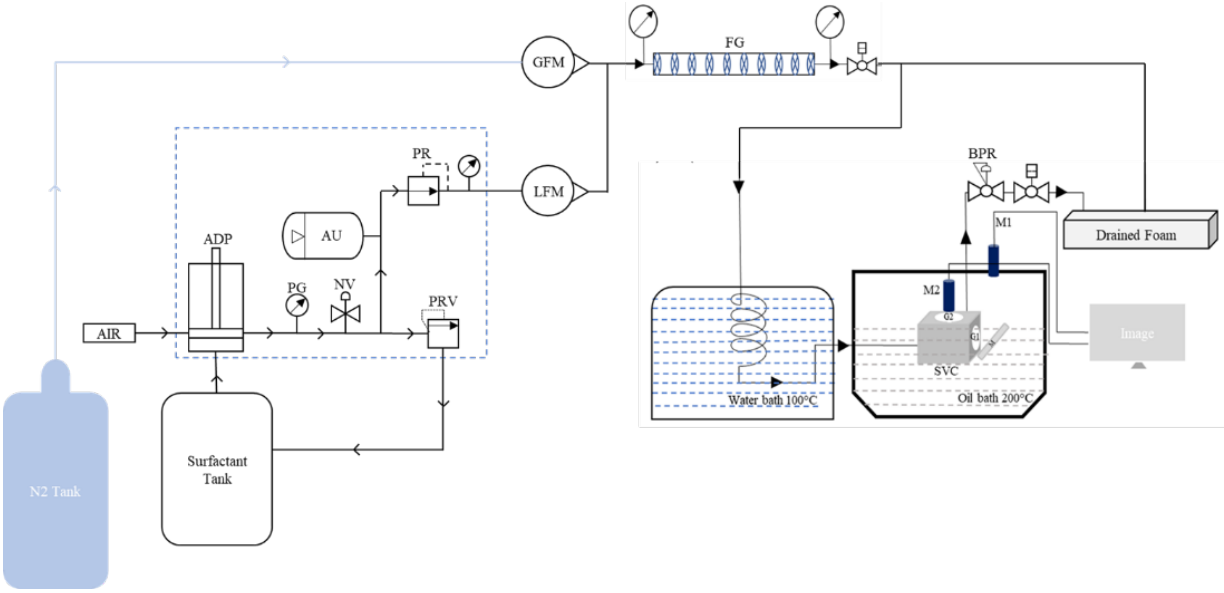

Figure 56 Diagram of test apparatus for foam testing and characterization. ADP – air driven pump, PG – pressure gauge, NV – needle valve, PRV – pressure relieve valve, AU – accumulator, PR – pressure regulator, LFM – liquid flow meter, GFM – gas flow meter, FG – foam generator, BPR – back pressure regulator, M1 – microscope for foam height, M2 – microscope for foam bubble size, SVC – sapphire view cell, G1 – glass window for foam height, G2 – glass window for foam bubble size, M – reflecting mirror.

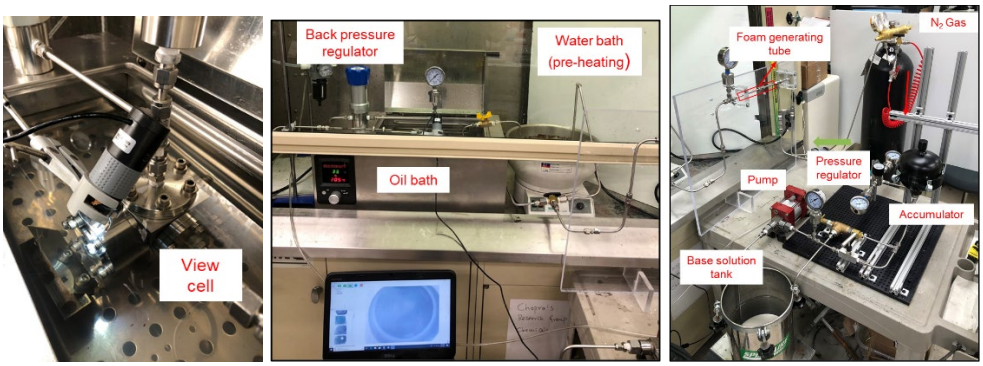

Figure 57 Main components of foam testing and characterization system (from right to left): foam generation section, foam monitoring section, and view cell setup.

8.2 CANDIDATE FOAMS

Candidate foams studied in this project included N_2 and CO_2 gaseous phases. Four surfactants have been identified after an extensive literature survey: alfa olefin sulfonate (AOS), sodium dodecyl sulfonate (SDS), Tergitol^{TM} (NP – 40), and cetyltrimethylammonium chloride (CTAC). Five stabilizing agents have been selected and studied: guar gum, bentonite clay, borate salt, SiO_2, graphene oxide (GO). Some of the agents like SiO_2 and GO just emerged recently.

The foam base solution and stabilizing agents with their concentrations are listed in Table 19 and Table 20, based on references (Simjoo et al., 2013; Thakore et al., 2020; Thakore et al., 2021).

Table 19 Surfactants used in this study

Chemical Name	Charge type	Concentration in the base solution (wt.%)
AOS	Anionic	1
SDS	Anionic	1
NP-40	Nonionic	1
CTAC	Cationic	1

Table 20 Stabilizing agents used in this study

Chemical Name	Type	Concentration in the base solution (wt.%)
Guar gum	Gelling agent	0.36
Bentonite clay	Gelling agent	0.36
Borate salt	Cross-linker	0.1
SiO_2	Nanoparticle, 50-70 nm	0.1
Graphene oxide	Nanoparticle, 4-30 µm (lateral size)	0.05

These foam compositions were studied for various purposes for gas and oil industry applications. Although the concentrations were developed, the data for thermal stability at the temperature and pressure conditions of interest are not available. The purpose of this project is to test and characterize the candidate foams and to identify a foam with the best thermal stability for EGS use. Figure 58 shows some example images obtained during a foam testing.

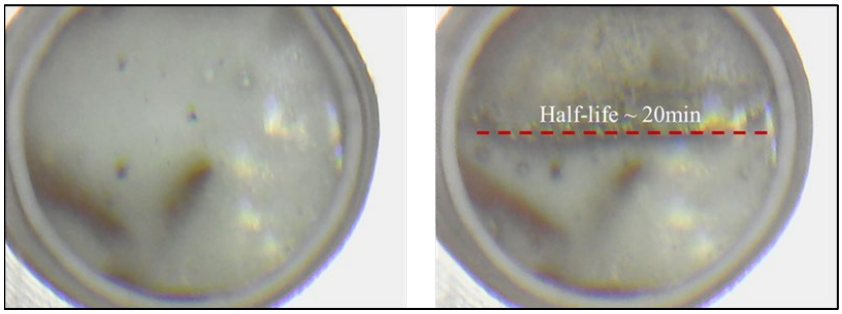

Figure 58 AOS + Crosslinker foams at 200°C and 1000 psi condition. The two images represent foam (a) after injection, (b) at 50% height.

8.3 EXPERIMENTAL RESULTS

8.3.1 Thermal Stability of AOS Foams

From the work in FY19 (Thakore et al., 2020), it was concluded that N_2 (non-polar) foams have better performance than CO_2 (polar) foams. The work in FY20 showed that, among all the surfactants tested to 400 psi (2.8 MPa), AOS foam demonstrated the best stabilizing effect as shown in Figure 59 (Thakore et al., 2021). Guar gum, crosslinker, and GO nanoparticles seemed to further enhance the foam stability.

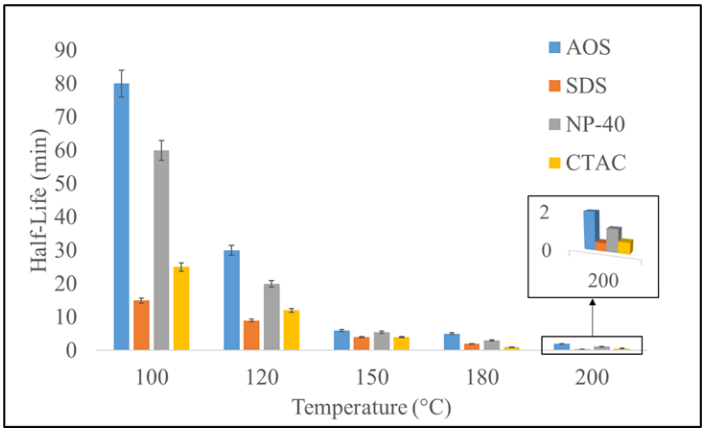

Figure 59 Thermal stability of foams with different surfactants at 400 psi.

In FY21, thermal stability testing on the down- selected AOS foams with different stabilizing agents was conducted at temperatures up to 200°C and pressures up to 1,000 psi (6.9 MPa) (Thakore et al., 2022).

As shown in Figure 60, at 100°C, the half-life of AOS foams (without stabilizing agents) reached 78 min at 1,000 psi. At 200°C, the half-life of AOS foams at 1,000 psi was decreased to 10 min, which was still 20 times higher than the half-life recorded at 100 psi.

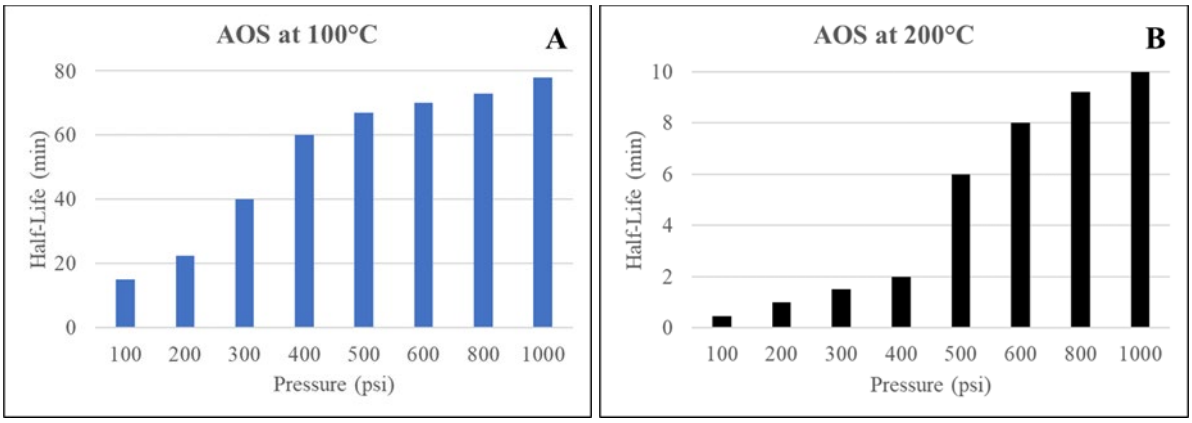

Figure 60 Thermal stability of AOS foams at (A)100°C and (B) 200°C.

Gelling agent guar gum enhanced the thermal stability of AOS foams. It is observed that, with addition of guar gum, the viscosity of foam base fluid was increased compared to base fluid with only surfactant.

Figure 61 compares thermal stability of AOS + Guar foams at 100°C and 200°C for the pressure range up to 1,000 psi. The half-life of guar foams at 100°C and 100 psi was recorded at 30 min; with increase in pressure to 1,000 psi, the half-life increased to 170 min. At 200°C, with increase in pressure from 100 psi to 1,000 psi, guar foams half-life was also observed to increase from 0.7 min to 14 min.

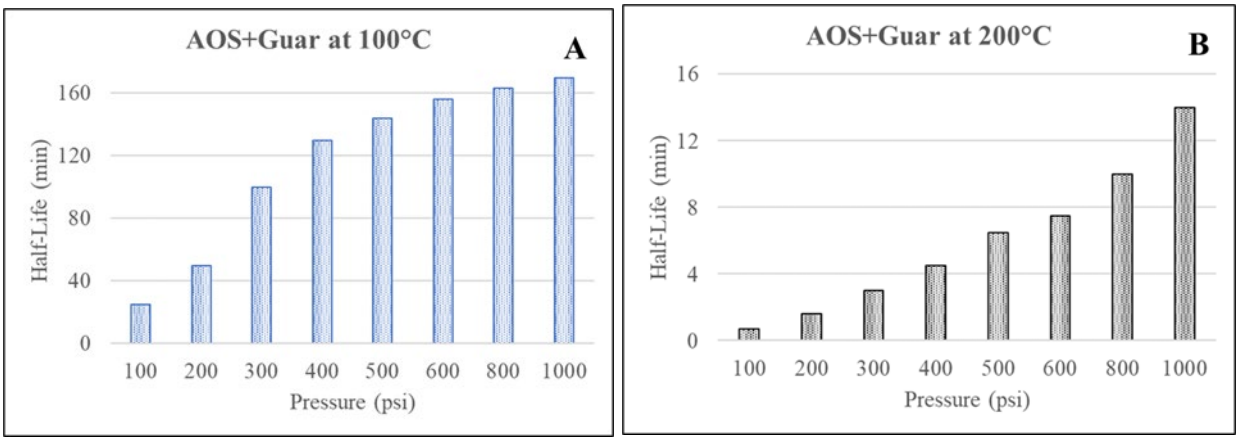

Figure 61 Thermal stability of AOS + Guar foams at (A)100°C and (B) 200°C.

Another gelling agent was bentonite clay which has a higher thermal capacity compared to guar as a gelling agent. Clay as a stabilizing agent also showed an increase in AOS foam half-life.

From Figure 62, the half-life of clay foams at both temperatures increased with increasing pressure within the tested pressure range. For 100ºC, half-life was recorded at 110 min at 1,000 psi, which is a drastic increase with respect to 20 min under 100 psi. At 200°C, when the pressure increased from 100 psi to 1,000 psi, the half-life of clay foams was recorded to increase form 0.5 min to 16 min.

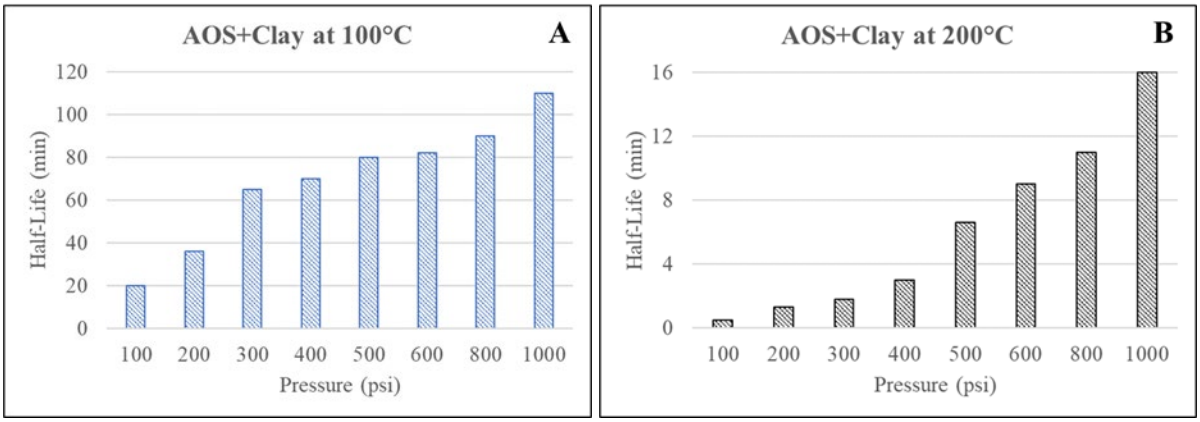

Figure 62 Thermal stability of AOS + Clay foams at (A)100°C and (B) 200°C.

Crosslinker base fluid was made by mixing gelling agent guar gum and borate salts in the ratio mentioned in Table 20. Addition of borate salt was observed to increase the base fluid's viscosity compared to other gelling agents.

AOS + Crosslinker foams have exhibited quite stable performance at the temperatures tested, as shown in Figure 63. A steady increase in crosslinker foam half-life was observed with increase in pressure at 100°C. The half-life at 100°C and 100 psi was recorded at 60 min which increased to 190 min with increase in pressure to 1000 psi. At 200°C and with pressure increasing from 100 psi to 1000 psi, the half-life of crosslinker foams was recorded to increase from 0.8 min to 20 min.

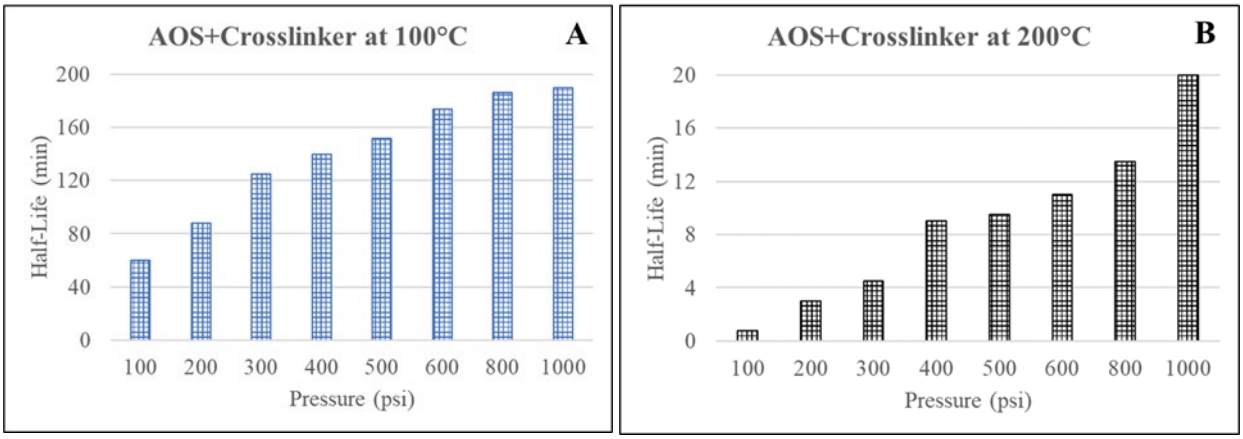

Figure 63 Thermal stability of AOS + Crosslinker foams at (A)100°C and (B) 200°C.

Another stabilizing agent studied was SiO_2 nanoparticles. Literature (Binks et al., 2005; Hunter et al., 2008) studies have shown that the addition of SiO_2 nanoparticles tends to block the lamella border of foam structure, which could result in decreased drainage rate and increased foam stability.

From Figure 64, at 100°C, continuous increase in foam half-life is observed from 50 min to 130 min with increase in pressure from 100 psi to 1000 psi. At 200°C, SiO_2 foams showed drastic increase in half-life from 5 min to 17 min with increase in pressure from 100 psi to 1000 psi at 200°C.

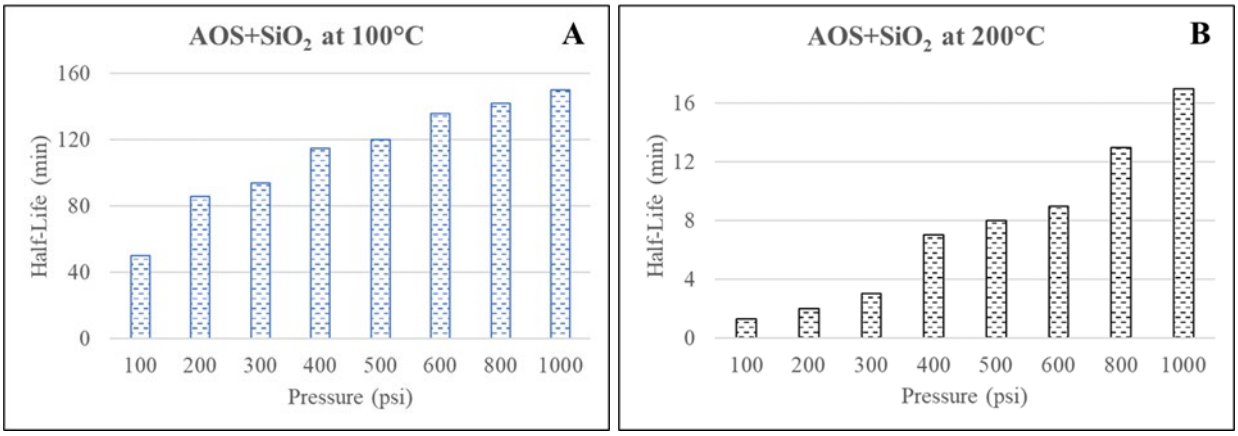

Figure 64 Thermal stability of AOS + SiO_2 foams at (A)100°C and (B) 200°C.

GO as a stabilizing agent is recently studied for foam stability (Kim, et al., 2010). GO dispersion itself acts as surfactant with addition of AOS in base fluid. GO as a stabilizing agent has shown significant enhancement in thermal stability of AOS foams.

From Figure 65, radical increase in foam half-life is observed with increase in pressure at 100°C and 200°C. The half-life of GO foams at 100°C and 100 psi was recorded at 65 min and drastic increase in half-life to 190 min was recorded with increase in pressure to 1000 psi. At 200°C, the half-life for GO foam increased from 1 min to 17 min with increase in pressure from 100 psi to 1000 psi.

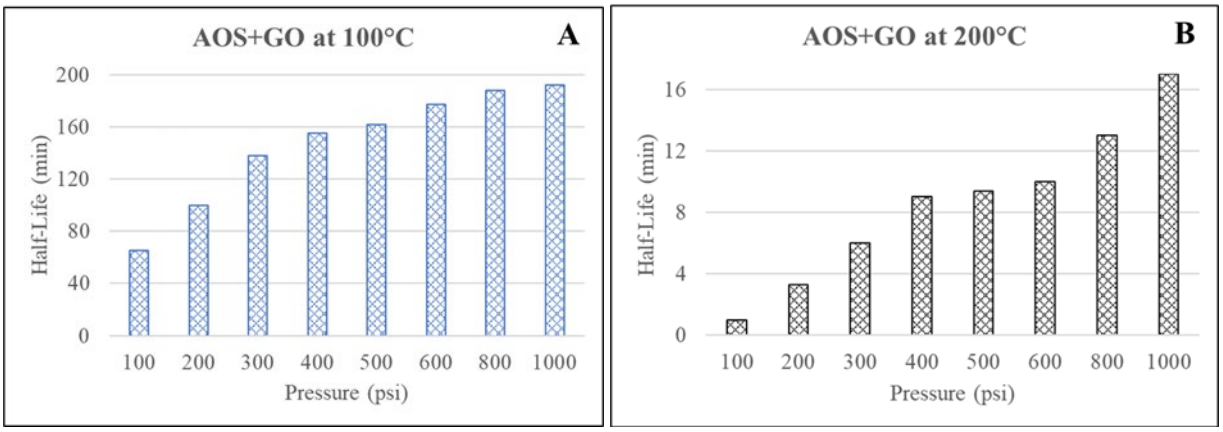

Figure 65 Thermal stability of AOS + GO foams at (A)100°C and (B) 200°C.

8.3.2 Foam Data Assembly

A 3D scatter plot of foam half-life as a function of pressure and temperature is shown in Figure 66. The figure includes the data collected at temperatures up to 200°C, and pressures up to 1,000 psi for AOS foams. For SDS, NP-40, and CTAC foams, the data are presented in the pressure range up to 400 psi. The half-life demonstrated consistent trends regarding tested parameters; it increases with increasing pressure and decreasing temperature.

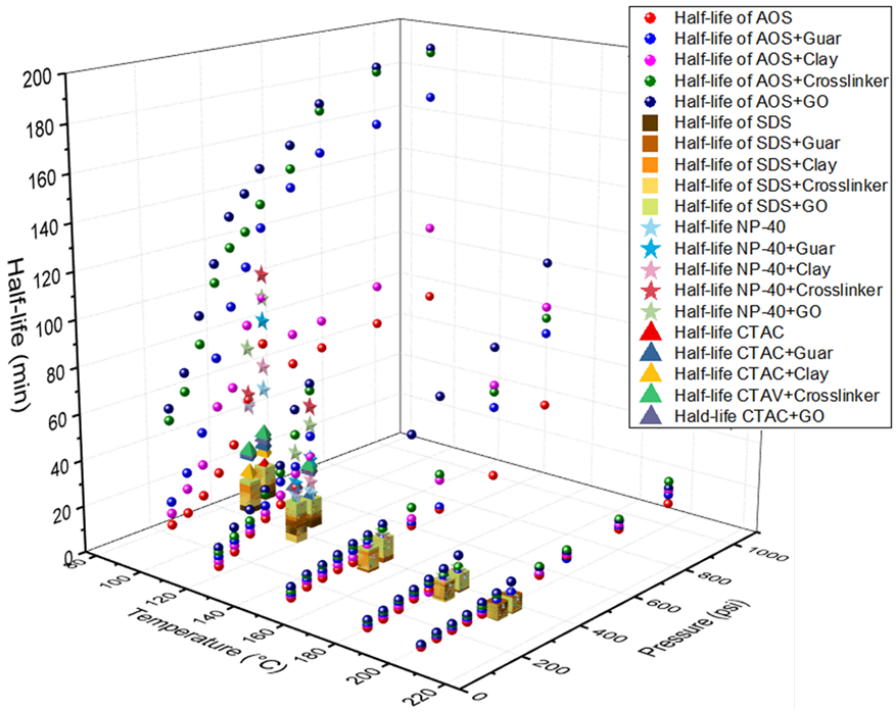

Figure 66 Half-life as a function of temperature and pressure for various aqueous N_2 foams with candidate surfactants and stablizing agents tested in this study.

8.3.3 Analysis and Discussion

8.3.3.1 Effect of temperature

The poor thermal stability at elevated temperatures may be attributed to the accelerated liquid phase drainage and gaseous phase diffusion. First of all, the reduced foam stability may be due to lower viscosity of the liquid phase at higher temperature, which resulted in more rapid liquid drainage and hence lower foam stability. A literature review on foam fracturing fluid by Gu and Mohanty (2015) suggested that temperature lowered the viscosity of foams by decreasing the liquid phase viscosity and stability of bubbles. In addition, the foam included in this study had a high quality of ~ 90-95%. Harris and Heath (1996) reported that high quality foams were highly unstable with either N_2 or CO_2 gaseous phases, as these foams were usually a mixture of very small and very large gas bubbles, which could lead to faster bubble coalescence.

Our analysis showed that for a given foam composition at a given pressure, the half-life, t, may be described by the following relationship

$$t = t_0 \, exp(-aT)$$

Equation 15

where T is temperature in Kelvin, and t_0 and a are fitting parameters. Figure 67 shows some fitting examples to this exponential decay function. The corresponding quantitative fitting results are given in Table 21 for 600 psi, 800 psi and 1,000 psi. These analyses show that t_0 depends on the pressure such that an increase in the pressure will lead to an increase in t_0. In addition, t_0 may also be a function of the type of foam composition. On the other hand, parameter a may be considered as a decay rate, which is dependent on the

foam composition and pressure as well. A higher value of *a* indicates a higher dependency of the foam stability on temperature.

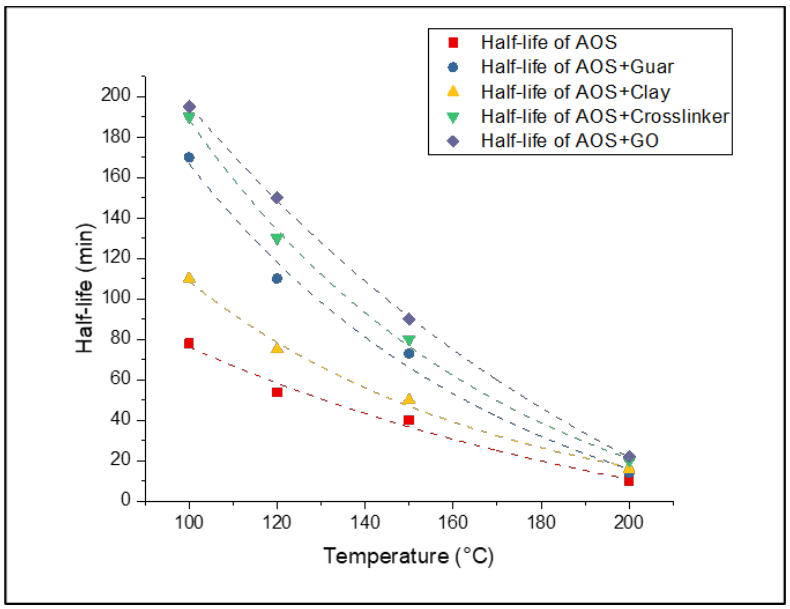

Figure 67 Exponential fitting curves showing the effect of temperature on foam half-life at 1000 psi.

Table 21 Fitting results to Equation 15 at 600 psi, 800 psi and 1000 psi.

	600 psi			800 psi			1000 psi		
Data set	t_0 (min)	-a (1/K)	R^2	t_0 (min)	-a (1/K)	R^2	t_0 (min)	-a (1/K)	R^2
AOS	488.4	0.022	0.96	503.3	0.021	0.97	680.0	0.021	0.96
AOS + Guar	2350.4	0.030	0.98	2814.6	0.028	0.99	2361.1	0.025	0.97
AOS + Clay	726.7	0.022	0.99	902.9	0.021	0.86	956.9	0.019	0.75
AOS + Crosslinker	2357.7	0.028	0.99	2643.5	0.026	0.99	1968.8	0.023	0.98
AOS + GO	3565.2	0.029	0.98	3124	0.027	0.97	2656.2	0.024	0.90
AOS + SiO_2	2184.2	0.027	0.99	1733.7	0.024	0.97	1662	0.022	0.83

8.3.3.2 Effect of pressure

In contrast to the effect of temperature, pressure shows a positive effect on the foam stability. The density of the dispersed phase (N_2) and the viscosity of the foam base fluid play an important role. With increase in pressure, both the N_2 density and fluid viscosity was increased, which led to more stable foams at high pressures. On the other hand, the mobility of surfactant molecules in the foam base fluid increases with increase in pressure (Akhtar, et al., 2018), which causes the liquid to flow from areas with lower surface tension to areas of higher surface tension and stabilizes the foam lamella border reducing the drainage rate. This phenomenon is termed as Marangoni effect (Szabries et al., 2019), which is accelerated under high pressure. Moreover, foam bubbles become smaller with increasing pressure, which reduces coalescence and enhances foam stability.

To model the effect of pressure on the foam half-life, both exponential and power law curve fitting were performed. Figure 68 shows some examples of curve fitting for exponential and power law models for foam

half-life at 200°C. Curve fitting results to the power law model (Equation 16) and the exponential law model (Equation 17) are listed in Table 22 to Table 24 for temperatures of 100ºC, 150ºC, and 200ºC, respectively.

$$t = p_0 P^{b_0}$$

Equation 16

$$t = p_0' e^{b_0' P}$$

Equation 17

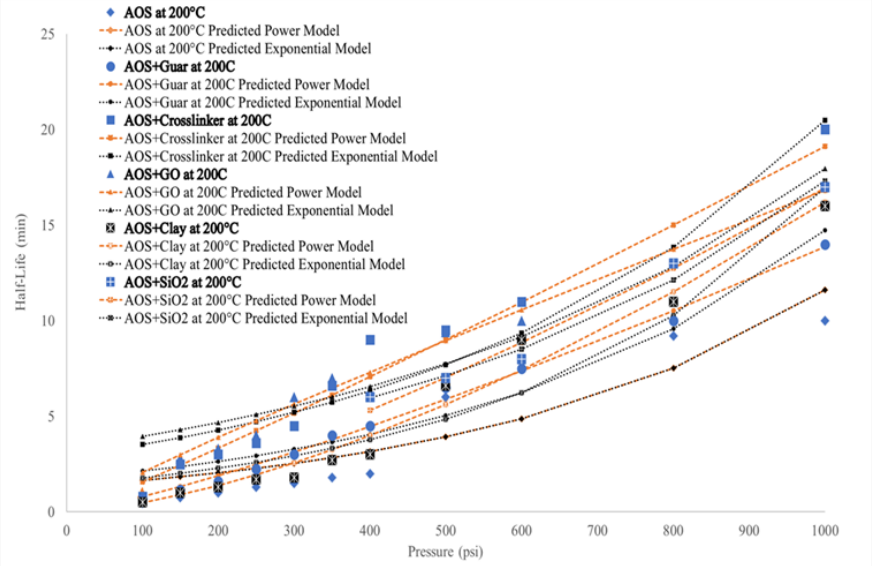

Figure 68 Exponential and power law curve fitting showing the effect of pressure on foam half-life at 200°C.

Table 22 Fitting results to the power law model (Equation 16) and the exponential model (Equation 17) at 100°C.

	Power model			Exponential model		
Data set	p_0 (min)	b_0 (1/K)	R^2	p'_0 (min)	b_0' (1/K)	R^2
AOS	1.418	0.594	0.88	30.28	0.00107	0.69
AOS + Guar	3.134	0.594	0.88	66.917	0.00107	0.67
AOS + Clay	2.005	0.580	0.94	38.67	0.0011	0.80
AOS + Crosslinker	8.517	0.458	0.95	88.53	0.00087	0.78
AOS + GO	12.787	0.402	0.93	98.973	0.00076	0.73
AOS + SiO_2	9.331	0.409	0.95	73.982	0.00079	0.78

Table 23 Fitting results to the power law model (Equation 16) and the exponential model (Equation 17) at 150°C.

	Power model			Exponential model		
Data set	p_0 (min)	b_0 (1/K)	R^2	p'_0 (min)	b_0' (1/K)	R^2
AOS	0.6805	0.333	0.97	1.981	0.00294	0.85
AOS + Guar	9.71×10^{-6}	2.291	0.95	2.977	0.00322	0.96
AOS + Clay	0.0395	0.919	0.92	2.827	0.0029	0.83
AOS + Crosslinker	0.000347	1.786	0.98	5.232	0.003	0.98

AOS + GO	0.0034	1.498	0.95	9.701	0.0024	0.90
AOS + SiO_2	0.0021	1.552	0.96	11.267	0.00216	0.99

Table 24 Fitting results to the power law model (Equation 16) and the exponential model (Equation 17) at 200°C.

	Power model			Exponential model		
Data set	p_0 (min)	b_0 (1/K)	R^2	p'_0 (min)	b'_0 (1/K)	R^2
AOS	0.0045	1.019	0.99	0.438	0.00393	0.95
AOS + Guar	0.00267	1.238	0.99	1.718	0.0021	0.94
AOS + Clay	0.0004	1.528	0.97	1.381	0.0025	0.93
AOS + Crosslinker	0.01054	1.086	0.96	2.892	0.002	0.91
AOS + GO	0.0312	0.910	0.97	3.338	0.0017	0.89
AOS + SiO_2	0.0027	1.267	0.98	2.935	0.00177	0.98

In summary, testing was conducted at pressures as high as 1,000 psi at temperatures up to 200°C. Four candidate surfactants were tested, out of which AOS showed the most promising results in terms of thermal stability at high temperature. Further enhancement in thermal stability of aqueous foams was achieved by addition of other stabilizing agents, including guar gum, bentonite clay, crosslinking agent, GO dispersion, and SiO_2 nanoparticles. All the stabilizing agents showed increase in thermal stability of AOS foams compared to only AOS foam. AOS foams with crosslinking agent and SiO_2/ GO dispersion showed the most stable foams with a half-life of 20 min and 17 min at 200° and 1,000 psi, respectively. The effect of temperature on foam stability was studied as an exponential decay model (Equation 15), which showed foam half-life decreased exponentially with increase in temperature. Whereas pressure showed positive effect on foam thermal stability, which could be expressed in terms of a power law (Equation 16) or exponential model (Equation 17). Further data analysis on the foam performance is discussed in Section 9.3.3.

8.3.3.3 Comparison with published data

The data generated in this study is compared with the work based on Maini and Ma (1986) in Figure 69. For the surfactants with same range of molecular weight, the half-life data obtained generally exhibited the similar temperature dependence as shown in the published data, but with noticeable difference of performance. Particularly, in short chain category (AOS C14-16, C16 AOS, Stepanflo 30), C16 AOS had a longer half-life at 100ºC than AOS C14-16. But that surfactant degraded faster with temperature. The rapid half-life degradation also occurred to one of the surfactants with long chain molecules in their data. Another long chain surfactant C2428 (whose figure legend is marked with the symbol *) displayed abnormal temperature dependance. It was reported that this surfactant was hard to dissolve at room temperature and heating to 150º improved the solubility and further half-life.

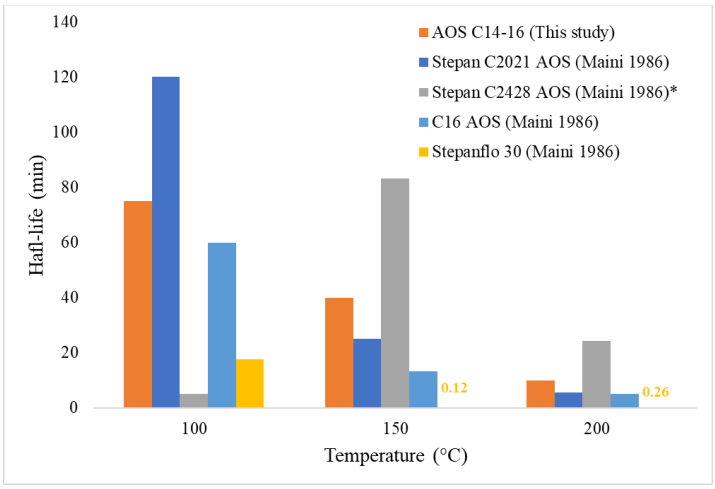

Figure 69 Comparison of foam half-life data obtained in this study with the published data.

9. CONCLUSION AND FUTURE WORK

9.1 INJECTION SYSTEM AND INJECTION TESTING

Foam fracturing is considered as a strategy to reduce use of water in the development of enhanced geothermal systems. This is significant for the areas where the geothermal source is abundant, but the water stress is very high already. The source rock mass generally needs to be engineered just as in a conventional enhanced geothermal system to obtain the required permeability.

The project focuses on the demonstration of foam fracturing technology in the laboratory under a simulated condition so that the critical factors in the field can be addressed in a more controllable way.

9.1.1 Foam Testing System

A foam fracturing testing system has been developed for EGS foam fracturing study. The system has a pressure rating of 6,000 psi (41.4 MPa) and automated controls for injecting single phase or variable quality foams. Computer controlled flow control valves and pressure regulators are used to cycle the system at user- specified amplitudes and frequencies (up to 50 Hz) to enable the investigation of cyclic fatigue effects. Pressure, mass rate, and density of foam are monitored online. A video camera is used to record the failure process of the specimen.

9.1.2 Experimental Results

Experimental results were reported for water and foam fracturing tests performed on Charcoal Black granite without confining pressure. Cylindrical specimen geometries with a blind hole were studied using water and nitrogen-gas-in-water foam as fracturing fluids. The effects of fracturing fluids and injection modes on the breakdown pressure and failure responses of the material were examined in detail.

9.1.2.1 Monotonic results

There was a hole effect on characteristic pressures; namely, pressures at fracture and breakdown were generally higher for small hole as expected. However, the size effect depended on the fluids used. At fracture initiation, the pressure ratio of small-hole to large-hole tests was reduced from 1.34 in water to 1.12 in foam, which may be associated with the high penetrability of gas phase of the foam used.

The breakdown pressures exhibited various increases with respect to fracture initiation pressures. The increases depended in the fluids used. For the large hole-size tests, the pressure ratio of breakdown to fracture initiation was reduced from 1.17 in water to 1.11 in foam, which shall be attributed to the different SCG responses of specimens with these fracturing fluids.

At the nominal same level of breakdown pressure, the water mass used for foam fracturing experiments was less than 50% of the water mass used for water fracturing experiments.

9.1.2.2 Cyclic results

A significant reduction in breakdown pressure was observed to be achievable by cyclic injection in this study. With a 4-sec period, the specimen can be cycled to failure with about 70% of the monotonic breakdown pressure in water fracturing and 58-94% (averaged 71%) of the monotonic breakdown pressure in foam fracturing. The number of cycles to failure ranged from 1 to 225.

The reduced operating pressure for initiating fracture has multiple potential field application benefits including reducing the risk associated with stimulation-induced micro-seismicity and reducing the burden on and reliability of surface equipment associated with higher pressure operation.

9.2 FOAM CHARACTERIZATION

9.2.1 Foam Testing System and Candidate Foams

A foam testing apparatus has been developed to test and characterize thermal stability of foams in a combinational condition of temperature and pressure. The current system is capable of testing foam at pressures up to 2,000 psi and temperatures up to 200°C. Half-life is obtained through monitoring the height of liquid separated from foam in a view cell filled with fresh foam and was used to characterize the performance of foams in this project.

Candidate foams studied in this project include those with N_2 and CO_2 gaseous phases. Four surfactants have been identified after an extensive literature survey: alfa olefin sulfonate (AOS), sodium dodecyl sulfonate (SDS), Tergitol^{TM} (NP – 40), and cetyltrimethylammonium chloride (CTAC). Five stabilizing agents were selected: guar gum, bentonite clay, borate salt, SiO_2, and graphene oxide (GO). Although the concentrations of these foams were developed previously, the data for thermal stability at the temperature and pressure conditions of interest are not available. The purpose of this project is to test and characterize the candidate foams and to identify a foam with the best thermal stability for EGS use.

9.2.2 Experimental Results

It was concluded that N_2 (non-polar) foams have better performance than CO_2 (polar) foams. Among all the surfactants tested, AOS foam demonstrated the best overall stabilizing effect.

All the AOS foams with stabilizing agents showed increase in thermal stability compared to AOS- only foam. AOS foams with crosslinking agent and SiO_2/ GO dispersion showed to be the most stable foams with a half-life of 20 min and 17 min at 200°C and 1,000 psi, respectively. The effect of temperature on foam stability was studied using an exponential decay model, which showed foam half-life decreased exponentially with increase in temperature. The effect of pressure on foam thermal stability could be expressed in terms of a power law or exponential model.

9.3 FUTURE WORK

9.3.1 Foam Fracturing Testing

9.3.1.1 Fracturing using gas only

The current study investigated foam that is very dry with foam quality more than 90% in monotonic injection to maximize the replacement of water. Such foam still carries the main features of foam in terms of high density and high viscosity, which offer various advantages for a fracture job in the field. There is a necessity to conduct the fracture test using gas only. This not only eliminates water use, but also clarifies how a crack growth can be shortened so that the breakdown pressure can be decreased. We realized that there were some experimental efforts made previously using CO_2 and N_2, for example, by Li et al. (2015) and Jia et al. (2018). But the relevant data needed to be collected systematically in both monotonic and cyclic injections.

9.3.1.2 Cyclic fracturing

There are critical variables that affect the lifetime of rock under cyclic injection for a given fluid and which remain to be investigated in a wider range.

Maximum pressure

The first would be amplitude or maximum pressure in cycling. The data points obtained in this study are still limited in terms of the maximum pressure range. It has become increasingly clear that the pressure must be ramped to fracture initiation pressure for the cyclic injection to be feasible in terms of used water and pump economics. The subcritical crack growth can be explored to accomplish hydraulic fracturing at a pressure lower than at breakdown in monotonic injection. The monitoring of flow rate in this study and of acoustic emission in a related study (Zhuang, et al, 2019b) demonstrated the existence of such a subcritical process in cycling.

Minimum pressure

The second variable would be the mean pressure or the minimum pressure. In a hydraulic stimulation in the field, the minimum pressure is identified as the closing pressure of fracture to avoid the crash of asperities of the fracture surface (Hofmann et al., 2018). It was demonstrated that the mean pressure would accelerate the failure using cement as a model material (Wang, et al, 2020). The effect of the mean pressure on the lifetime of rock in cyclic injection can be better studied in the laboratory.

Cycling period

A further variable would be the cycling frequency or period. A 4-sec pulse period was used in this study to demonstrate the effectiveness of cyclic injection in reducing the breakdown pressure for hydraulic stimulation. The results are promising in the cases of both water and foam. The cyclic injection in hydraulic stimulation in the field is generally implemented by an injection scheme consisting of sub-sections whose period varies from days to hours to seconds (Hofmann et al., 2018). The effect of cycling frequency on the fatigue life was shown to be mixed (Attewell and Farmer, 1973; Cerfontaine and Collin, 2018). To facilitate the hydraulic stimulation, fracturing tests need to integrate the time factor in cyclic testing to develop the database for target source rock so the field job can be better served.

9.3.1.3 Confining pressure effect

There is a need to investigate the effect of confining pressure on fracturing of rock in the view of application. Traditionally, confining pressure is applied in a pressure cell to cylindrical specimen, where inner flow for fracturing and outer pressure for confining are controlled using separate control valves. Additional approaches to apply confining can be achieved through a shrink-fit sleeve or externally loading. These approaches may be explored for this task, but the current test system or specimen needs to be modified.

9.3.1.4 Temperature effect

The experimental data related to the effect of temperature on the fatigue life of rocks are limited (Cerfontaine and Collin, 2018). The observation is this effect can be tested in a laboratory setting as demonstrated in this project on foam characterization. The confined or unconfined specimens can be heated to simulate the temperature of rocks in EGS. An environmental chamber or tape heater was used in a related project previously and can be explored. The current test system needs to be modified to accommodate this test requirement and a pre-heated fracturing fluid can be used.

9.3.1.5 Uncertainty of test results

There is a substantial variation in fracturing data, especially breakdown mass rate and mass. One of the contributors would be the heterogeneity of materials as illustrated by the various fracture patterns. To address this issue with the uncertainty of results, the number of tests needs to be raised to at least 10 (ASTM, 2016).

9.3.2 Numerical Study

A primary finite element analysis (FEA) using commercial software COMSOL was conducted in this project (Wang et al., 2021b). A model has been developed with the fluid-structure interaction included. Further work would be to incorporate Darcy's law to image the permeating flow and pressure field within the medium.

9.3.3 Foam Stability Study

9.3.3.1 Data analysis

There has been a large volume of foam performance data generated in this project. The foam compositions include various gaseous phases, surfactants, and stabilizing agents. The testing conditions include various temperatures and pressures. The current data, together with existing database (more than 1000 data points), provide a sound base for advanced analysis and prediction. One future objective is to investigate the trend of performance data and to establish the link between laboratory data and field performance. Multivariable regression and machine learning can be explored for this purpose.

9.3.3.2 Testing and characterization

To support the foam application in waterless stimulation of EGS, the identified candidate foams are expected to be tested with an extended range of temperature and pressure. Part of the strategy was discussed in Section 7.4, including gas phases and performance data collection in the extended testing conditions.

9.3.4 Downhole Device Development

The purpose of this task is to implement the concept of foam injection realized in the laboratory setting in a design that can be accommodated in a downhole environment (Wang et al, 2019). This needs to integrate the input from EGS industries to better reflect the foam injection requirements in the field. The goal is to complete the downhole foam injector design and provide the recommendation for future implementation.

10. ACKNOWLEDGMENTS

This research was sponsored by the US Department of Energy, Assistant Secretary for Energy Efficiency and Renewable Energy, Geothermal Technologies Office, as part of the Enhanced Geothermal Systems Program under Contract No. DE-AC05-00OR22725 with the US Department of Energy.

Authors are grateful to David Wilson, Darren Loposser, Danny Parrott, Anthony McBee, Nathan Grundy, Cody West, Matt Rumbolt, James Oran, April Case, Eric Loyd of the ORNL for their help in flow control, line assembling, and pressure system evaluation; Harmon Phillips of Control Management Technology, Jason Reynolds of Intek, Carmen Bracco of TEK CV&F, Timothy Cavicchio of High Pressure Equipment, Eric Balcerzak & Will Hewitt of Swagelok, Larry Miller of Airgas, Marco Escobar of SC Hydraulic Engineering, Rao Choday of SFP for their help and discussion on fluid measurement and control.

Authors want to thank Haoqi Li and several students at Temple University for their support in experimental work and database development. Authors also thank Drs. Lianshan Lin, James Hemrick, Edgar Lara-Curzio of ORNL for the review of this manuscript and the comments.

11. REFERENCES

Abdul, A. S., Gibson, T. L., Rai, D. N., Selection of Surfactants for the Removal of Petroleum Products from Shallow Sandy Aquifers, *Ground Water*, **28** (6), (1990), 920-926.

Ahmed, S., Elraies, K. A., Hashmet, M. R., Alnarabiji, M. S., Empirical Modeling of the Viscosity of Supercritical Carbon Dioxide Foam Fracturing Fluid under Different Downhole Conditions, *Energies*, **11**, (2018), 782.

Akhtar, T. F., Ahmed, R., Elgaddafi, R., Shah, S., Amani, M., Rheological Behavior of Aqueous Foams at High Pressure, *J. Petroleum Sci. Eng.*, Vol. **162**, (2018), 214-224.

Akhtar, T. F., Rheology of Aqueous and Polymer-Based Nitrogen Foams at High Pressure and High Temperature (HPHT) Conditions, M.S. Thesis, (2017), U. of Oklahoma.

ASTM D3967-16 Standard Test Method for Splitting Tensile Strength of Intact Rock Core Specimens, ASTM International, (2016), West Conshohocken, PA 19428.

Atkinson, B., Subcritical Crack Growth in Geological Materials. *J. Geophys. Res.,* **89** (B6), (1984), 4077-4114.

Attewell, P., Farmer, W., Fatigue Behaviour of Rock. *Int. J. Rock Mech. Min. Sci.,* **10**, (1973), 1–9.

Baud, P., Zhu, W., Wong, T.-F., Failure Mode and Weakening Effect of Water on Sandstone, *J. Geophys. Res*., **105** (B7), (2000), 16,371– 16,389.

Beckers, K. F., Lukawski, M. Z., Anderson, B. J., Moore, M. C., and Tester, J. W., Levelized Costs of Electricity and Direct-Use Heat from Enhanced Geothermal Systems, *J. Renewable Sustainable Energy* **6**, (2014), 013141.

Binks, B. P., Horozov, T. S., Aqueous Foams Stabilized Solely by Silica Nanoparticles, *Angew. Chem. Int. Ed.*, **44** (24), (2005),3722-5.

Blackwell, D., Richards, M., Frone, Z., Batir, J., Ruzo, A., Dingwall, R., and Williams, M., Temperature-At-Depth Maps for the Conterminous U. S. and Geothermal Resource Estimates, *GRC Trans.*, **35**, (2011), 1545 – 1550.

Cawiezel, K. E., & Niles, T. D., Rheological Properties of Foam Fracturing Fluids under Downhole Conditions, SPE Hydrocarbon Economics and Evaluation Symposium, Dallas, Texas, (1987), SPE 16191.

Cerfontaine, B., Collin, F., Cyclic and Fatigue Behaviour of Rock Materials: Review, Interpretation and Research Perspectives, *Rock Mech Rock Eng.,* **51**, (2018), 391–414.

Chabora, E., Zemach, E., Desert Peak EGS Project, Geothermal Technologies Program 2013 Peer Review, U.S. DOE EERE, (2013).

Chambers, D. J., Foam for Well Stimulation, Foams: Fundamentals and Applications in the Petroleum Industry, Advances in Chemistry Series 242, American Chemical Society, Washington DC, Ed. Schramm, L.L., (1994), 355- 404.

Chen, M., Guo, T., Qu, Z., Sheng, M., Mu, L., 2022, Numerical Investigation into Hydraulic Fracture Initiation and Breakdown Pressures Considering Wellbore Compliance Based on the Boundary Element Method, *J. Petrol. Sci. Eng*., **211**, 110162.

Cheng, A. H.-D., Poroelasticity, (2016), Springer.

Christopher, U. E., Time-Dependent Initiation of Multiple Hydraulic Fractures in Rocks, M.S. Thesis, (2015), Swanson School of Engineering, U. of Pittsburgh.

Ciantia, M., Castellanza, R., di Prisco, C., Experimental Study on the Water-Induced Weakening of Calcarenites. *Rock Mech. Rock Eng.,* **48** (2), (2015), 441–461.

Clark, C. E., Harto, C. B., Sullivan, J. L., Wang, M. Q., Water Use in the Development and Operation of Geothermal Power Plants, ANL/EVS/R-10/5, (2011).

Coldspring, https://www.coldspringusa.com/building-materials/colors-and-finishes/charcoal-black/, accessed Jan. 2022

Cote, L. J., Kim, J., Tung, V. C., Luo, J., Kim, F., and Huang, J., Graphene Oxide as Surfactant Sheets, *Pure Appl. Chem.*, **83** (1), (2011), 95–110.

Detournay, E. and Carbonell, R., 1997, Fracture-Mechanics Analysis of the Breakdown Process in Minifracture or Leakoff Test, *SPE Prod. & Facil*., 195- 199.

Detournay, E., Cheng, A. H.-D., Poroelastic Response of a Borehole in a Non-Hydrostatic Stress Field, *Int. J. Rock Mech. Min. Sci. & Geomech. Abstr.,* **25**, (3), (1988), 171-182.

Enzendorfer, C., Harris, R. A., Valko, P., Economides, M. J., Fokker, P. A., & Davies, D. D., Pipe Viscometry of Foams, *J. Rheol.*, **39** (2), (1995), 345-358.

Faroughi, S.A., Pruvot, A. J.-C. J., and McAndrew, J., The Rheological Behavior of Energized Fluids and Foams with Application to Hydraulic Fracturing: Review, *J. Petroleum Sci. Eng.*, **163**, (2018), 243-263.

Finnie, I. and Heller, W. R., Creep of Engineering Materials, McGraw-Hill, (1959), 182-184.

Freyman, M., Hydraulic Fracture & Water Stress: Water Demand by the Numbers, Ceres, (2014).

Fry, J. F, and French R. J., A Mechanical Foam-Generator for Use in Laboratory, *J. Appl. Chem.*, (1), (1951), 425-429.

Gauglitz, P. A., St. Laurent, C. M., and Radke, C. J., Experimental Determination of Gas-Bubble Breakup in a Constricted Cylindrical Capillary, *Ind. Eng. Chem. Res.*, **27**, (1988), 1282-1291.

Gu, M., Mohanty, K. K., Rheology of Polymer-Free Foam Fracturing Fluids, *J. Petroleum Sci. Eng.*, **134**, (2015), 87-96.

Haimson, B., Fairhurst, C., Hydraulic Fracturing in Porous-Permeable Materials. *J. Petroleum Tech.*, (1969), 811-817.

Harris, P. C., & Heath, S. J., High-Quality Foam Fracturing Fluids. Society of Petroleum Engineers. (1996), SPE-35600-MS

Harris, P. C., Reidenbach, V. G., High-Temperature Rheological Study of Foam Fracturing Fluids, *J. Petroleum Technol.*, (1987), 613-619.

Harris, P., A Comparison of Mixed Gas Foams with N_2 and CO_2 Foam Fracturing Fluids on a Flow Loop Viscometer, *SPE Prod. Facil*., **10**, (1995), 197–203.

Harris, P. C., Haynes, R. J., and Egger, J. P., The Use of CO-Based Fracturing Fluids in the Red Fork Formation in the Anadarko Basin, Oklahoma, *J. Petroleum Technol.*, **36**, (1984), 1003–1008.

Herzhaft, B., Kakadjian, S., Moan, M., Measurement and Modeling of the Flow Behavior of Aqueous Foams Using a Recirculating Pipe Rheometer, *Colloid. Surface. Physicochem. Eng. Aspect.,* **263**, (2005), 153–164.

Hofmann, H., Zimmermann, G., Farkas, M., Huenges, E., Zang, A., Leonhardt, M., Kwiatek, G., Martinez-Garzon, P., Bohnhoff, M., Min, K.-B., Fokker, P., Westaway, R., Bethmann, F., Meier, P., Yoon, K.

S., Choi, J. W., Lee, T. J., Kim K. Y., First Field Application of Cyclic Soft Stimulation at the Pohang Enhanced Geothermal System Site in Korea, *Geophys. J. Int.*, **217**, (2019) 926–949.

Hofmann, H., Zimmermann, G., Zang, A., and Min, K.-B., Cyclic Soft Stimulation (CSS): a New Fluid Injection Protocol and Traffic Light System to Mitigate Seismic Risks of Hydraulic Stimulation Treatments, *Geotherm Energy,* **6**, 27, (2018).

Holt, T., Vassenden, F., Svorstol, I., Effects of Pressure on Foam Stability; Implications for Foam Screening, SPE/DOE Improved Oil Recovery Symposium, (1996), Society of Petroleum Engineers.

Hubbert, M. K., Willis, D. G., Mechanics of Hydraulic Fracturing, *AIME Petroleum Trans.,* **210**, (1957), 153 -169.

Hunter, T. N., Pugh, R. J., Franks, G. V., Jameson, G. J., The Role of Particles in Stabilising Foams and Emulsions, *Advances in Colloid and Interface Science*, **137** (2), (2008), 57-81.

Hutchins, R. D., Miller, M. J., A Circulating-Foam Loop for Evaluating Foam at Conditions of Use, *SPE Prod. Facil*., **20**, (2005), 286–294.

Jacobs, T., Shale Revolution Revisits the Energized Fracture, *JPT*, (2014), 48-56.

Jaeger, J. C., Cook, N. G. W., and Zimmerman, R. W., Fundamentals of Rock Mechanics, 4th Edition, (2007), Blackwell Pub.

Jia, Y., Lu, Y., Elsworth, D., Fang, Y., Tang, J., Surface Characteristics and Permeability Enhancement of Shale Fractures due to Water and Supercritical Carbon Dioxide Fracturing, *J. Petroleum Sci. Eng.*, **165**, (2018), 284–297.

Khan, S. A., Schnepper, C. A., & Armstrong, R. C., Foam Rheology: III. Measurement of Shear Flow Properties. *J. Rheol.*, **32** (1), (1988), 69-92.

Kim, J., Cote, L. J., Kim, F., Yuan, W., Shull, K. R. and Huang, J., Graphene Oxide Sheets at Interfaces, *J. Am. Chem. Soc.*, **132** (23), (2010), 8180–8186.

Kohshour, I. O., Barati, R., Yorro, M.C., Leshchyshyn, T., Adejumo, A.T., Ahmed, U., Kugler, I., Reynolds, M., McAndrew, J., Economic Assessment and Review of Waterless Fracturing Technologies in Shale Resource Development: A Case Study, *J. Earth Sci.*, **28**, (2017), 933-948.

Kroezen, A.B., Wassink, J.G., & Bertlein, E., Foam Generation in a Rotor—Stator Mixer, *Chem. Eng. Process.*, **24**, (1988), 145-156.

Lee, K.-K., Ellsworth, W. L., Giardini, D., Townend, J., Ge, S., Shimamoto, T., Yeo, I.-W., Kang, T.-S., Rhie, J., Sheen, D.-H., Chang, C., Woo, J.-U., and Langenbruch, C., Managing Injection-Induced Seismic Risks, *Science*, **364** (6442), (2019), 730- 732.

Li, X., Feng, Z, Han, G., Elsworth, D., Marone, C., Saffer, D., Hydraulic Fracturing in Shale with H_2O, CO_2 and N_2, The 49th US Rock Mechanics / Geomechanics Symposium, San Francisco, CA, USA, (2015), ARMA 15-786.

Liu, Y., Grigg, R. B., Svec, R. K., CO_2 Foam Behavior: Influence of Temperature, Pressure, and Concentration of Surfactant, The SPE Production Operations Symposium, Oklahoma City, Oklahoma (2005), SPE-94307-MS.

Lu, G., Uwaifo, E. C., Ames, B. C., Ufondu, A., Bunger, A. P., Prioul, R., Aidagulov, G., Experimental Demonstration of Delayed Initiation of Hydraulic Fractures below Breakdown Pressure in Granite, The 49th US Rock Mechanics / Geomechanics Symp., San Francisco, CA, USA, (2015), ARMA 15-190.

Lv, Q., Li, Z., Li, B., Li, S., and Sun, Q., Study of Nanoparticle−Surfactant-Stabilized Foam as a Fracturing Fluid, *Ind. Eng. Chem. Res.,* **54**, (2015), 9468−9477.

Maini, B. B., Ma, V., Laboratory Evaluation of Foaming Agents for High-Temperature Applications - I. Measurements of Foam Stability at Elevated Temperatures and Pressures, *J. Can. Petrol. Technol.*, **25**, (1986), 65-69.

Majer, E. L., Baria, R., Stark, M., Oates, S., Bommer, J., Smith, B., Asanuma, H., Induced Seismicity Associated with Enhanced Geothermal Systems, *Geothermics,* **36**, (2007), 185–222

Mattson, E. D., Neupane, G., Plummer, M., Jones, C. and Moore, J. Long-Term Sustainability of Fracture Conductivity in Geothermal Systems using Proppants, *Proceedings*, 41st Workshop on Geothermal Reservoir Engineering, Stanford University, Stanford, California, SGP-TR-209, (2016).

McClure, M. W., Horne, R. N., An Investigation of Stimulation Mechanisms in Enhanced Geothermal Systems, *Int. J. Rock Mech. & Mining Sci.*, **72** (2014), 242–260.

McGarr, A., Maximum Magnitude Earthquakes Induced by Fluid Injection, *J. Geophys. Res.: Solid Earth*, **119**, (2014), 1008-1019.

Michalske, T., Freiman, S., A Molecular Mechanism for Stress Corrosion in Vitreous Silica. *J. Am. Ceram. Soc.,* **66** (4), (1983), 284–288.

MIT, The Future of Geothermal Energy, (2006), INL/EXT0611746.

Momeni, A., Karakus, M., Khanlari, G. R., Heidari, M., Effects of Cyclic Loading on the Mechanical Properties of a Granite. *Int. J. Rock Mech. Min. Sci.*, **77**, (2015), 89–96.

Munson, B. R., Young, D. F., Okiishi, T. H., Huebsch, W. W. Fundamentals of Fluid Mechanics, Sixth Edition, (2009), John Wiley & Sons, Inc.

Nara, Y., Morimoto, K., Hiroyoshi, N., Yoneda, T., Kaneko, K., Benson P., Influence of Relative Humidity on Fracture Toughness of Rock: Implications for Subcritical Crack Growth, *Int. J. Solids Struct.,* **49** (18), (2012), 2471–2481.

Olasolo, P., Juárez, M. C., Morales, M. P., D´Amico, S., Liarte, I. A., Enhanced Geothermal Systems (EGS): A Review, *Renewable and Sustainable Energy Reviews*, **56**, (2016), 133-144.

Patel, S. M., Sondergeld, C. H., Rai, C. S., Laboratory Studies of Hydraulic Fracturing by Cyclic Injection, *Int. J. Rock Mech. & Min. Sci.,* **95**, (2017), 8–15.

Reidenbach, V. G., Harris, P. C., Lee, Y. N., Lord, D. L., Rheological Study of Foam Fracturing Fluids Using Nitrogen and Carbon Dioxide, *SPE Production engineering*, (1986), 31-41.

Ren, F., Wang, J. J.-A., and Wang, H., Alternative Approach for Cavitation Damage Study Utilizing Repetitive Laser Pulses, *Wear*, **270** (1-2), (2010b), 115-119.

Ren, F., Wang, J.-A., and Wang, H., Cavitation Damage Study via a Novel Repetitive Pressure Pulse Approach, *Proc. PVP2010*, ASME Pressure Vessels and Piping Conference, Bellevue, WA, USA, (2010a), No. PVP2010-26102.

Ren, F., Wang, J.-A., Liu, Y., and Wang, H., Development of a Pulsed Pressure- Based Technique for Cavitation Damage Study, *Proc*. the 8th Int. Symposia on Cavitation, Singapore, Ed. C.-D. Ohl, E. Klaseboer, S. W. Ohl, S. W. Gong, and B. C. Khoo, (2012), 382-387.

Saint-Jalmes, A., Vera, M.U. and Durian, D.J., Uniform Foam Production by Turbulent Mixing: New Results on Free Drainage vs. Liquid Content, *Eur. Phys. J. B*, **12**, (1999), 67-73.

Scholz, C., Kranz, R., Notes on Dilatancy Recovery. *J. Geophys. Res.*, **79** (14), (1974), 2132–2135.

Simjoo, M., Rezaei, T., Andrianov, A., Zitha, P. L. J., Foam Stability in the Presence of Oil: Effect of Surfactant Concentration and Oil Type, *Colloids and Surfaces A: Physicochemical and Eng. Aspects*, **438**, (2013), 148-158.

Sun, X., Liang, X., Wang, S., Lu, Y., Experimental Study on the Rheology of CO_2 Viscoelastic Surfactant Foam Fracturing Fluid, *J. Petroleum Sci. Eng.*, **119**, (2014), 104 - 111.

Szabries, M., Jaeger, P., Amro, M. M., Foam Analysis at Elevated Pressures for Enhanced Oil Recovery Applications, *Energy Fuels*, **33** (5), 2019, 3743-3752.

Tao, Z. and Wang, H., The Effects of Joint Cohesion and Water Saturation on Rock Slope Stability, *Proc.* the 5th Int. Conf. on Appl. of Statis. and Prob. in Soil and Struc. Eng., Vancouver, Canada, Lind, N. C. (Ed.), Vol. 2, (1987), 791-796.

Thakore, V., Ren, F., Voytek, J., Wang, H., Wang, J.-A. J., Polsky, Y., High Temperature Stability of Aqueous Foams for Potential Application in Enhanced Geothermal System (EGS), *Proceedings*, 46th Workshop on Geothermal Reservoir Eng., Stanford U., Stanford, CA, SGP-TR-218, (2021), 336-347.

Thakore, V., Ren, F., Voytek, J., Xi, J., Wang, H., Wang, J.-A. J., Polsky, Y., High-Temperature Stability of Aqueous Foams as Potential Waterless Hydrofracking Media for Enhanced Geothermal Systems (EGS), *Proceedings*, 45th Workshop on Geothermal Reservoir Eng., Stanford U., Stanford, CA, SGP-TR-216, (2020), 535-544.

Thakore, V., Ren, F., Wang, H., Wang, J.-A. J., Polsky, Y., High Temperature, High Pressure Stability of Aqueous Foams for Potential Application in Enhanced Geothermal System (EGS), *Proceedings*, 47th Workshop on Geothermal Reservoir Eng., Stanford U., Stanford, CA, SGP-TR-223 (2022), 604-614.

Trippetta, F., Collettini, C., Meredith, P., Vinciguerra, S., (2013) Evolution of the Elastic Moduli of Seismogenic Triassic Evaporites Subjected to Cyclic Stressing. *Tectonophysics*, **592**, (2013), 67–79.

U.S. DOE, GeoVision, Harnessing the Heat Beneath Our Feet, 2019, https://www.energy.gov/eere/geothermal/downloads/geovision-harnessing-heat-beneath-our-feet, accessed Jan. 2020.

Valko, P. and Economides, M. J., Hydraulic Fracture Mechanics, (1997), New York: John Wiley & Sons.

Valvias, Gas Density, www.valvias.com/miscellanea-material-properties-gases-density.php, accessed on 7/25/2020.

Wang, H. and Tao, Z., Simulating Technique of Joint Network and Its Application in the Stability Analysis of Rock Slope, *Proc*. the 2nd Int. Conf. on Mech. of Jointed and Faulted Rock, Vienna, Austria, Rossmanith, H.-P. (Ed.), Balkema, Rotterdam, (1995), 627-632.

Wang, H., Wang, J.-A. J., Polsky, Y., Ren, F., Thakore, V., Study on Foam Fracturing of Granite for the Development of Enhanced Geothermal Systems, *Proceedings*, 46th Workshop on Geothermal Reservoir Engineering, Stanford University, Stanford, California, SGP-TR-218, (2021a), 348-360.

Wang, H., Wang, J.-A. J., Polsky, Y., Ren, F., Thakore, V., FY21 Annual Report for Foam Fracturing Study for Stimulation Development of Enhanced Geothermal System (EGS), Prepared for DOE GTO EGS Program, (2021b).

Wang, H., Wang, J.-A. J., Polsky, Y., Ren, F., Li, H., Thakore, V., Xi, J.: Study of Foam Fracturing for Enhanced Geothermal Systems Using Model Material, *Proceedings*, 45th Workshop on Geothermal Reservoir Engineering, Stanford University, Stanford, CA, SGP-TR-216, (2020a), 545-555.

Wang, H., Wang, J.-A. J., Polsky, Y., Ren, F.: Research Considerations for Foam Fracturing in Stimulation Development for Enhanced Geothermal Systems, *Proceedings*, 44th Workshop Geotherm. Reservoir Eng., Stanford University, Stanford, CA, SGP-TR-214, (2019), 617-627.

Wang, H., Xu, W., Cai, M., Xiang, Z., Kong, Q., Gas Permeability and Porosity Evolution of a Porous Sandstone under Repeated Loading and Unloading Conditions, *Rock Mech, Rock, Eng.*, **50** (8), (2017a), 2071–2083.

Wang, J.-A. J., Wang, H., Ren, F., Cox, T. S., A Cavitation-Based Hydro-Fracturing Technique for Geothermal Reservoir Stimulation, *U.S. Patent*, (2017b), US 9,574,431 B2.

Wang, J.-A. J., Wang, H., Ren, F., Cox, T. S., Cavitation- Based Hydro- Fracturing Stimulator, *U.S. Patent*, (2016), US 9,500,068 B2.

Wang, J.-A. J., Wang, H., Ren, F., Cox, T. S., Specimen for Evaluating Pressure Pulse Cavitation in Rock Formation, *U.S. Patent*, (2020b), US 10,578,533 B2.

Wang, J.-A., Ren, F., and Wang, H., An Innovative Low/ High Temperature Repetitive Pressure- Pulse Apparatus for Cavitation Damage Research, ORNL/TM-2009/260, (2009), Oak Ridge National Laboratory, Oak Ridge, TN.

Wanniarachchi, W. A. M., Ranjith, P. G., Perera, M. S. A., Rathnaweera, T. D., Zhang, D. C., Zhang, C., Investigation of Effects of Fracturing Fluid on Hydraulic Fracturing and Fracture Permeability of Reservoir Rocks: An Experimental Study Using Water and Foam Fracturing, *Eng. Fract. Mech.*, **194**, (2018), 117-135.

Warnock, W. E., Harris, P. C., and King, D. S., Successful Field Applications of CO_2-Foam Fracturing Fluids in the Arkansas-Louisiana-Texas Region, *J. Petroleum Technol.*, **37**, (1985), 80-88.

Wendorff, C.L., & Earl, R.B., Foam Fracturing Laboratory, 58th Annual Technical Conference and Exhibition, San Francisco, CA, (1983), SPE 12025.

Xiao, J., Ding, D., Jiang, F., Xu, G., Fatigue Damage Variable and Evolution of Rock Subjected to Cyclic Loading. *Int. J. Rock Mech. Min. Sci.*, **47** (3), (2010), 461–468.

Xie, L., Min, K.-B. & Song, Y., Observations of Hydraulic Stimulations in Seven Enhanced Geothermal System Projects, *Renewable Energy*, **79**, (2015), 56-65.

Xu, J., Li, S.-C., Tao, Y.-Q., Tang, X.-J., Wu, X., Acoustic Emission Characteristic during Rock Fatigue Damage and Failure. *Proc. Earth Planet. Sci.*, **1**(1), (2009), 556–559.

Xue, Z., Worthen, A., Qajar, A., Robert, I., Bryant, S. L., Huh, C., Prodanovic´, M., Johnston, K. P., Viscosity and Stability of Ultra- High Internal Phase CO_2-in-Water Foams Stabilized with Surfactants and Nanoparticles with or without Polyelectrolytes, *J. Colloid Interf. Sci.*, **461**, (2016), 383–395.

Young, C., Graham, C, Controlled Foam Injection Progress towards Automated Hard Rock Excavation, The 5th Int. Symp. on Mine Mechanization and Automation, Sudbury, Ontario, (1999).

Young, C., Controlled Foam Injection Methods and Means for Fragmentation of Hard Compact Rock and Concrete, *U.S. Patent*, (2002), US 6375271 B1.

Yu, J., Khalil, M., Liu, N., Lee, R., Effect of Particle Hydrophobicity on CO_2 Foam Generation and Foam Flow Behavior in Porous Media, *Fuel*, **126**, (2014), 104–108.

Zang, A., Stephansson, O., Stenberg, L., Plenkers, K., Specht, S., Milkereit, C., Schill, E., Kwiatek, G., Dresen, G., Zimmermann, G., Dahm, T., and Weber, M., Hydraulic Fracture Monitoring in Hard Rock at 410 m Depth with an Advanced Fluid-Injection Protocol and Extensive Sensor Array, *Geophys. J. Int.,* **208**, (2017), 790–813.

Zang, A., Yoon, J. S., Stephansson, O., Heidbach, O., Fatigue Hydraulic Fracturing by Cyclic Reservoir Treatment Enhances Permeability and Reduces Induced Seismicity, *Geophys. J. Int.*, **195**, (2013), 1282-1287.

Zang, A., Zimmermann, G., Hofmann, H., Stephansson, O., Min, K.-B. Kim, K. Y., How to Reduce Fluid-Injection- Induced Seismicity, *Rock Mech. Rock Eng.*, **52**, (2019), 475–493.

Zhang, Y., ZEISS-CT Inspection with Versa, (2021), Oak Ridge National Laboratory.

Zhuang, L., Kim, K. Y., Jung, S. G., Diaz, M., and Min, K.-B., Effect of Water Infiltration, Injection Rate and Anisotropy on Hydraulic Fracturing Behavior of Granite, *Rock Mech Rock Eng.*, **52**, (2019a), 575–589.

Zhuang, L., Kim, K. Y., Jung, S. G., Diaz, M., Min, K.-B., Zang, A., Stephansson, O., Zimmermann, G., Yoon, J.-S., & Hofmann, H.: Cyclic Hydraulic Fracturing of Pocheon Granite Cores and Its Impact on Breakdown Pressure, Acoustic Emission Amplitudes and Injectivity, *Int. J. Rock Mech. Min. Sci.*, **122**, (2019b), 104065.

Zimmermann, G., Moeck, I., Blöcher, G., Cyclic Waterfrac Stimulation to Develop an Enhanced Geothermal System (EGS)—Conceptual Design and Experimental Results, *Geothermics,* **39**, (2010), 59–69.

Zimmermann, G., Zang, A., Stephansson, O., Klee, G., Semiková, H., Permeability Enhancement and Fracture Development of Hydraulic In Situ Experiments in the Äspö Hard Rock Laboratory, Sweden, *Rock Mech. Rock Eng.,* **52**, (2019), 495–515.

Zoback, M. D., Rummel, F., Jung, R., and Raleigh, C. B., 1977, Laboratory Hydraulic Fracturing Experiments in Intact and Pre-Fractured Rock, *Int. J. Rock Mech. Min. Sci. & Geomech. Abstr*., **14**, 49-58.

APPENDIX A.

APPENDIX A. CRITICAL COMPONENTS FOR FOAM FRACTURING SYSTEM

Table 25 Components for liquid section

Components		Model or P/N	Specifications	Pressure rating	Manufacturer/ Supplier
PM1	Pump	S10014-M058-65	L3 air-driven, w/ distance piece & silencer, stall pressure 7 200 psi at 100 psi air pressure	8 875 psi	SC hydraulic Eng. Corp.
RD1	Rupture disc	RD6500	NPT safety head 15-61 NMB w/ pressure rating 15 000 psi	6 500 psi	HiP
AC1	Accumulator	BA04-60-SK-N-W-2-A	1 Gal bladder accumulator, 6000 psi, 1-5/8" SAE, Nitrile, SS trim, nickel plated, ASME	6 000 psi, 1 Gal	SFP
	Pre-charge kit	CKT-0050	Charging and gauging kit for bottom repairable accumulator, 5000 psi; instructions manual	5 000 psi	SFP
PR1	Pressure regulator	KHP1WXB4C6S200G0	316SS, pressure control range 50 to 6 000 psi, maximum inlet pressure 10 000 psi, port B, ¼" female NPT, outlet gauge only	6 000 psi	Swagelok
NV1	Needle valve	15F-11NFB	two-way straight valve, 1/4" NPT, 15,000 psi	15 000 psi	HiP
	SS tubing	89785K23	Smooth-bore seamless 316 SS tubing ¼" OD, 0.049" wall thickness, 6 ft. long	6 100 psi at 72 deg F	McMaster
FM1	Flow meter	210-IDT-TUL1/4(HP)-4/20-24V-(ER)	RheoTherm flow meter, loop tube, SS316, ¼" tube stubs, 4-20 mA analog out, 24 VDC input power; 23 – 2 000 cc/min, 6 000 psi	6 000 psi	Intek
CV1	Control valve	SW4081-FRC1	¼" OD connection, 0.188" orifice size, 0.65 Cv, 2-way straight, 15 000 psi, regulating stem; electric actuator, 24 VDC, 4-20 mA analog out	15 000 psi	Parker
CK1	Check valve	10-41AF4	Ball check valve, ¼" OD tube, taper seal, 10 000 psi	10 000 psi	HiP

Table 26 Components for gas section

Components		Model or P/N	Specifications	Pressure rating	Manufacturer/ Supplier
GC	Gas cylinder	NI UHP6K	Nitrogen UHP GR 5.0 size 6K CGA 677	6 000 psi	Airgas
	Pressure regulator w/ needle valve	Y1112900CB 677-AL	Regulator high pressure piston model 2900 CGA 677 400-6 000 psi 1/4" NPT male outlet needle valve Brass	6 000 psi	Airgas
	SS tubing	89785K903	Smooth-bore seamless 316 SS tubing 1/16” OD, 0.02” wall thickness, 6 ft. long	6 400 psi at 72 deg F	McMaster
FM2	Flow meter	210-IDT-TUL1/16(HP)-4/20-24V-(ER)	RheoTherm flow meter, loop tube, SS316, 1/16” tube stubs, 4-20 mA analog out, 24 VDC input power; 50 – 5 000 cc/min, 6 000 psi	6 000 psi	Intek
CV2	Control valve	SW4081-FRC1	¼” OD connection, 0.188” orifice size, 0.65 Cv, 2-way straight, 15 000 psi, regulating stem; electric actuator, 24 VDC, 4-20 mA analog out	15 000 psi	Parker
CK2	Check valve	10-41AF4	Ball check valve, ¼” OD tube, taper seal, 10 000 psi	10 000 psi	HiP

Table 27 Components for foam section

Components		Model or P/N	Specifications	Pressure rating	Manufacturer/ Supplier
TEE	Tee connect	10-23AF4	¼” OD tube, taper seal, 10 000 psi	10 000 psi	HiP
IF	Line filter	10-51AF4	¼” OD tube, taper seal, 100 micron filter, 4 pc./ set, 10 000 psi	10 000 psi	HiP
RD3	Rupture disc	RD6500	NPT safety head 15-61 NMB w/ pressure rating 15 000 psi	6 500 psi	HiP
AC3	Accumulator	BA04-60-SK-N-W-2-A	1 Gal bladder accumulator, 6000 psi, 1-5/8” SAE, Nitrile, SS trim, nickel plated, ASME	6 000 psi, 1 Gal	SFP
	Pre-charge kit	CKT-0050	Charging and gauging kit for bottom repairable accumulator, 5000 psi; instructions manual	5 000 psi	SFP

PR3	Pressure regulator	KHP1WXB4 C6S200G0	316SS, pressure control range 50 to 6 000 psi, maximum inlet pressure 10 000 psi, port B, ¼” female NPT, outlet gauge only	6 000 psi	Swagelok
FM3	Flow meter	M14-AAD-22-0-H	mini Cori flow meter, pressure rating 6 000 psi, measurement range 0.5 to 500 ml/min	6 000 psi	Bronkhorst
CV3	Control valve	SW4081-FRC1	¼” OD connection, 0.188” orifice size, 0.65 Cv, 2-way straight, 15 000 psi, regulating stem; electric actuator, 24 VDC, 4-20 mA analog out	15 000 psi	Parker
PV1	Pulse valve	10-11AF4-MPO-NO	¼” taper seal straight needle valve, normally open, air actuator, 35 air psi	10 000 psi	HiP
PV2	Pulse valve	10-11AF4-MPO-NC	¼” taper seal straight needle valve, normally closed, air actuator, 45 air psi	10 000 psi	HiP
	Nylon tube	5548K74	Flexible high-pressure nylon tubing semi-clear, 0.17" ID, 1/4" OD, 25 ft	330 psi at 72 deg F	McMaster
	Tee	SS-400-3	Union tee, ¼” OD x ¼” OD	6 600 psi	Swagelok
BPR	Back pressure regulator	KHB1W0G4 C6P200A0	316SS, pressure control range 50 to 6000 psi, port G, ¼” female NPT, inlet gauge only	6 000 psi	Swagelok
NV3	Needle valve	15F-11NFB	two-way straight valve, 1/4" NPT, 15,000 psi	15 000 psi	HiP
PS	Pressure sensor	060-1108-02TJG	TJE model, capacity 15 000 psi w/ Daytronic 3270 strain gage conditioner/ indicator	15 000 psi	Honeywell